DESIGN OF A MULTI-FREQUENCY UNDERWATER TRANSDUCER USING CYLINDRICAL PIEZOELECTRIC ELEMENTS

A THESIS SUBMITTED TO
THE GRADUATE SCHOOL OF NATURAL AND APPLIED SCIENCES
OF
MIDDLE EAST TECHNICAL UNIVERSITY

BY

ŞİAR DENİZ YAVUZ

IN PARTIAL FULFILLMENT OF THE REQUIREMENTS
FOR
THE DEGREE OF MASTER OF SCIENCE
IN
MECHANICAL ENGINEERING

JULY 2011

Approval of the thesis:

DESIGN OF A MULTI-FREQUENCY UNDERWATER TRANSDUCER USING CYLINDRICAL PIEZOELECTRIC ELEMENTS

submitted by **ŞİAR DENİZ YAVUZ** in partial fulfillment of the requirements for the degree of **Master of Science in Mechanical Engineering Department, Middle East Technical University** by,

Prof. Dr. Canan Özgen
Dean, Graduate School of **Natural and Applied Sciences** _____

Prof. Dr. Süha Oral
Head of Department, **Mechanical Engineering** _____

Prof. Dr. S. Kemal İder
Supervisor, **Mechanical Engineering Dept., METU** _____

Prof. Dr. Hayrettin Köymen
Co-Supervisor, **Electrical and Electronics Engineering Dept., Bilkent University** _____

Examining Committee Members:

Prof. Dr. Haluk Darendeliler
Mechanical Engineering Dept., METU _____

Prof. Dr. S. Kemal İder
Mechanical Engineering Dept., METU _____

Prof. Dr. Hayrettin Köymen
Electrical and Electronics Engineering Dept., Bilkent University _____

Prof. Dr. Levend Parnas
Mechanical Engineering Dept., METU _____

Asst. Prof. Dr. Ender Ciğeroğlu
Mechanical Engineering Dept., METU _____

Date: July 5th, 2011

I hereby declare that all information in this document has been obtained and presented in accordance with academic rules and ethical conduct. I also declare that, as required by these rules and conduct, I have fully cited and referenced all material and results that are not original to this work.

Name, Last name : ŞİAR DENİZ YAVUZ

Signature :

ABSTRACT

DESIGN OF A MULTI-FREQUENCY UNDERWATER TRANSDUCER USING CYLINDRICAL PIEZOELECTRIC ELEMENTS

Yavuz, Şiar Deniz

M.Sc., Department of Mechanical Engineering

Supervisor : Prof. Dr. S. Kemal İder

Co-Supervisor : Prof. Dr. Hayrettin Köymen

July 2011, 148 Pages

In this thesis, numerical and experimental design of a multi-frequency underwater acoustic transducer with cylindrical piezoelectric ceramic tubes is studied. In the numerical design, the acoustic, mechanical and thermal performances of the transducer are investigated by means of finite element method (FEM) in ANSYS. The design of the transducer that meets the acoustic requirements is checked in terms of the mechanical and thermal performances. After the completion of the numerical design, the transducer is manufactured and some performance tests such as impedance test, hydrostatic pressure test and full-power operation test are applied to it. Finally, the results of the numerical and experimental design are compared. As a result, the design of an underwater acoustic transducer that operates at two frequency bands centered at about 30 and 60 kHz under a hydrostatic pressure of 30 bars is accomplished. This transducer also resist to a shock loading of 500g for 1 millisecond.

Keywords: Acoustic Transducer, Piezoelectricity, Underwater Acoustics, Finite Element Analysis

ÖZ

SİLİNDİRİK PİEZOELEKTRİK ELEMANLAR KULLANARAK ÇOK FREKANSLI SUALTI ÇEVİRİCİ TASARIMI

Yavuz, Şiar Deniz
Yüksek Lisans, Makina Mühendisliği Bölümü
Tez Yöneticisi : Prof. Dr. S. Kemal İder
Ortak Tez Yöneticisi : Prof. Dr. Hayrettin Köymen

Temmuz 2011, 148 Sayfa

Bu tezde, silindirik piezoelektrik seramik tüplerle çok frekanslı bir sualtı akustik çeviricinin sayısal ve deneysel tasarımı çalışılmıştır. Sayısal tasarımda, ANSYS'de sonlu elemanlar yöntemi (FEM) kullanılarak çeviricinin akustik, mekanik ve ısıl performansları incelenmiştir. Akustik gereksinimleri sağlayan çevirici tasarımı mekanik ve ısıl performans açılarından kontrol edilmiştir. Sayısal tasarımın tamamlanmasından sonra çevirici üretilmiş ve çeviriciye, empedans testi, hidrostatik basınç testi ve tam-güç çalışma testi gibi bazı performans testleri uygulanmıştır. Son olarak, sayısal ve deneysel tasarım sonuçları karşılaştırılmıştır. Sonuç olarak, 30 ve 60 kHz'de merkezlenmiş iki frekans bandında 30 bar'lık hidrostatik basınç altında çalışan bir sualtı akustik çeviricinin tasarımı gerçekleştirilmiştir. Bu çevirici aynı zamanda 1 milisaniye boyunca 500g'lik bir şok yüklemesine de dayanmaktadır.

Anahtar Kelimeler: Akustik Çevirici, Piezoelektriklik, Sualtı Akustiği, Sonlu Elemanlar Analizi

To My Family

ACKNOWLEDGEMENTS

I would like to express my deepest gratitude to my supervisor Prof. Dr. S. Kemal İder and co-supervisor Prof. Dr. Hayrettin Köymen for their guidance, advice, criticism, encouragements and insight throughout the research.

I would also like to thank my family, especially my fiancée, Nazlı, for their support and encouragement.

TABLE OF CONTENTS

LIST OF TABLES

TABLES

LIST OF FIGURES

FIGURES

CHAPTER 1

INTRODUCTION

1.1 Transducer

A transducer is a device, usually electrical, electronic, electro-mechanical, electromagnetic, photonic, or photovoltaic, that converts one type of energy or physical attribute to another for various purposes. Generally, it is thought that transducers are devices that only perform information transfer by energy conversion; however, information transfer is not required for a device to be considered a transducer. Instead, anything that converts energy can be considered a transducer [1] [2].

1.2 The Applications and Types of Transducers

Transducers have so many application areas that they are everywhere in daily life. A light bulb, for example, is a transducer, which transforms electrical energy into the visible light. Electric motors and generators are other common forms of transducer, which performs transformation between electrical and mechanical energy [2].

On the other hand, many devices that are used for measurement and information transfer such as microphones, potentiometers, tachometers, accelerometers,

Geiger meters, thermometers, pressure sensors, antennae etc. are classified as transducers. A microphone, for example, converts sound waves into electrical signal in order to transfer information over wires. A pressure sensor or a thermometer transforms the physical force or temperature into an analog reading for measurement, respectively [2].

Actually, there are three types of transducers according to the task they perform. Firstly, a *"sensor"* is a transducer that is employed to measure a physical quantity in one form and to display it after converting into another form, usually an electrical or digital signal. Potentiometers, tachometers and accelerometers are some examples of sensors, which are used for measurement of displacement, rotational speed and acceleration, respectively. Secondly, an *"actuator"* produces movement from an input signal (generally an electrical signal). For instance, a loudspeaker generates acoustic waves from the input electrical signal after transforming it into magnetic field. Similarly, an electric motor produces kinetic energy from the electrical energy for mechanical tasks. Thirdly, some transducers have both functions. An ultrasonic transducer, for example, generates ultrasonic waves as an actuator and detects ultrasonic waves as a sensor [1].

More extensively, transducers can be classified according to their working principles or in other words, the energy types that they convert as follows [1]:

1. **Electromagnetic:** (Transformation between electrical energy and electromagnetic energy)
   - ***Antenna*** - converts electromagnetic waves into electric current and vice versa.
   - ***Cathode ray tube (CRT)*** - converts electrical signals into visual form.

- ❖ ***Fluorescent lamp, light bulb*** **-** converts electrical power into visible light.
- ❖ ***Magnetic cartridge*** **-** converts motion into electrical form.
- ❖ ***Photo detector or Photo resistor (LDR)*** **-** converts changes in light levels into resistance changes.
- ❖ ***Tape head*** **-** converts changing magnetic fields into electrical form.
- ❖ ***Hall Effect sensor*** **-** converts a magnetic field level into electrical form only.

2. **Electrochemical:** (Transformation of chemical properties into electrical signal)
   - ❖ ***pH probes*** **-** measure pH of a liquid.
   - ❖ ***Electro-galvanic fuel cell*** **-** measures the concentration of oxygen gas in scuba diving and medical equipment.
   - ❖ ***Hydrogen sensor*** **-** detects the presence of hydrogen.

3. **Electromechanical:** (Transformation between electrical and mechanical energy (motion))
   - ❖ ***Electroactive polymers (EAPs)*** **-** convert electrical voltage into shape deformation.
   - ❖ ***Galvanometer*** **-** converts electrical current into analog reading by rotary deflection of the pointer.
   - ❖ ***MEMS (Micro-electro-mechanical systems)*** **-** convert electrical energy into mechanical energy or vice versa. (20 micrometers to a millimeter in size)
   - ❖ ***Rotary motor, linear motor*** **-** converts electrical energy into mechanical energy.
   - ❖ ***Vibration powered generator*** **-** converts mechanical energy into electrical energy.

- ***Potentiometer when used for measuring position*** **-** converts displacement of a body into electrical resistance change.
- ***Load cell*** **-** converts force into electrical signal using strain gauge.
- ***Accelerometer*** **-** measures the proper acceleration, which is the acceleration experienced relative to freefall.
- ***Strain gauge*** **-** converts the mechanical strain of an object into electrical resistance change.
- ***String Potentiometer*** **–** measures the linear position of a moving object.
- ***Air flow sensor*** **-** measures the amount of a fluid flowing through a chamber.

4. **<u>Electroacoustic:</u>** (Transformation between acoustic energy (sound) and electrical energy)
   - ***Loudspeaker, earphone*** **-** converts electrical signals into sound.
   - ***Microphone*** **-** converts sound into an electrical signal.
   - ***Pick up (music technology)*** **-** converts motion of metal strings into an electrical signal.
   - ***Tactile transducer*** **-** converts solid-state vibrations into electrical signal.
   - ***Piezoelectric crystal*** **-** converts solid-state electrical modulations into an electrical signal.
   - ***Geophone*** **-** converts a ground movement (displacement) into voltage.
   - ***Gramophone pick-up*** **-** converts sound into an electrical signal.
   - ***Hydrophone*** **-** converts changes in water pressure (underwater sound) into an electrical form.
   - ***Sonar transponder*** **-** converts changes in water pressure (underwater sound) into an electrical signal or vice versa.

5. **Photoelectric:** (Transformation between light and electrical energy)
   - ***Laser diode, light-emitting diode*** **-** converts electrical power into forms of light.
   - ***Photodiode, photo resistor, phototransistor, photomultiplier tube*** **-** converts changing light levels into electrical form.

6. **Electrostatic:** (Utilization of electrostatic energy for measurement)
   - ***Electrometer*** **-** measures electric charge or electrical potential difference.

7. **Thermoelectric:** (Transformation between thermal energy (temperature) and electrical energy)
   - ***RTD (Resistance Temperature Detector)*** **-** measures temperature by utilizing electrical resistance change.
   - ***Thermocouple*** **-** measures temperature by producing voltage related to temperature difference.
   - ***Peltier cooler*** **-** provides cooling by creating heat flux from one side of the device to the other side with consumption of electrical energy.
   - ***Thermistor (includes PTC resistor and NTC resistor)*** **-** measures temperature from electrical resistance change.

8. **Radioacoustic:** (Transformation between acoustic energy (sound) and radio waves)
   - ***Geiger-Müller tube*** **-** used for measuring radioactivity.
   - ***Receiver (radio)*** **-** converts radio signal into another form such as sound, pictures, digital data, measurement values, navigational positions, etc.

As it can be seen from the above classification, transducers have a wide range of application areas and types. Among all these types, electroacoustic transducers

are one of the most common types. Particularly, they are the main parts for all underwater systems that convert electrical energy into the acoustic waves or vice versa. Therefore, for underwater acoustic, electroacoustic transducers are the most significant issue.

1.3 History of Underwater Acoustics & Electroacoustic Transducers

The science of underwater acoustics began at the end of the fifteenth century when Leonardo da Vinci wrote "If you cause your ship to stop, and place the head of a long tube in the water and place the outer extremity to your ear, you will hear ships at a great distance from you." This notable note indicates many crucial points in underwater acoustics. It states that the sound that a moving ship generates in the water propagates to large distances. Moreover, it describes a receiving device, in this case an air-filled tube, in order to detect this sound. It also emphasizes the necessity of reducing the self noise to get better results [3]. Although this technique provides no indication about the direction of the sound due to the acoustic mismatch between the air and water, it had widely used until World War I, when the direction could be estimated by adding a second tube and bringing the upper end of this to the other ear [4].

After these pioneering words of Leonardo da Vinci, many scientists started to work on this subject. In 1687, the first mathematical treatment of the theory of sound was introduced by Isaac Newton in his *Mathematical Principles of Natural Philosophy*. He was the first scientist who was able to relate the propagation of sound in fluids to measurable physical quantities such as density and elasticity. He found the speed of sound in air to be proportional to the square root of the ratio of atmospheric pressure to air density, which was corrected later by Laplace, who included the specific heat ratio in the expression

[3]. During the eighteenth and nineteenth centuries, the contributions of Bernoulli, Euler, LaGrange, d'Alembert, and Fourier to the theory of sound accelerated the improvement in underwater acoustics [5].

The speed of sound in water was first measured in 1826 by Daniel Colladon, a Swiss physicist, and Charles François Sturm, a French mathematician. On Lake Geneva, they used a mechanoacoustic transducer - striking of a bell under water - as a projector (source) and a tube as a hydrophone (receiver). The bell was struck simultaneously with a flash of light, and an observer in a boat 13 km away measured the time interval between the flash and arrival of the sound by his ear placed at one end of the tube with the other end in the water. Their measurement result, which was 1435 m/s for water at 8 °C, is very close to the accepted value today for fresh water, which is 1439 m/s [6].

As a result of the interest in telegraphy in the latter part of the eighteenth and the first part of the nineteenth centuries, in 1830, Joseph Henry introduced electroacoustic transducers into the telegraphy with a moving armature transducer (now often called variable reluctance transducer) in which transmitted signal was observed by the sound of the armature striking its stops. Pioneered by this development, Alexander Graham Bell invented the telephone in 1876 by using moving armature electroacoustic transducers on both ends of the line [6].

In 1877, Lord Rayleigh published his famous book *Theory of Sound* and established the modern acoustic theory. This book is one of the monumental works in acoustics since it gives the basis for acoustic theory such as generation, propagation, and reception of sound. Elastic behavior of solids, liquids, and gases are also covered in this significant acoustics source [3].

Among all these progresses, there are two certain milestones for underwater acoustics; discoveries of magnetostriction and piezoelectricity. In the 1840s, James Joule noticed that magnetization causes changes in the dimensions of some materials such as iron, nickel, cobalt, manganese and their alloys, in his experiments including the measurements of the change in length of an iron bar when magnetized. Conversely, mechanical stress induces a change in the magnetic properties of magnetostrictive materials [7]. Then, in 1880, Jacques and Pierre Curie discovered the piezoelectricity, which is a counterpart of magnetostriction as a transduction process – the conversion between electricity and sound [4]. Similarly, piezoelectric materials such as Quartz crystals, Rochelle salt, ammonium dihydrogen phosphate (ADP) develop an electric charge when subjected to a mechanical strain or undergo mechanical deformation in the presence of an electric field [7]. These properties are so significant for underwater acoustics that materials with such properties are still being used as the main component of most underwater acoustic transducers.

Early in the twentieth century, Submarine Signal Company (now part of Raytheon Mfg. Co.) developed the first commercial application of underwater sound to navigation. Ships were provided with a method of determining range to lightship by simultaneously sounding an underwater bell and an above-water foghorn, which were both located on the lightship. This was accomplished by measuring the time interval between the arrival of the airborne and waterborne sound [6].

In 1912, the first high-power underwater source, a new type of moving coil transducer, was developed by R. A. Fessenden. This device, which was driven electrically in the range 500 to 1000 Hz, was successfully used for signaling between submarines and for echo ranging. On 27 April, 1914, stimulated by the sinking of the Titanic in 1912, an iceberg at a distance of nearly two miles was

detected by underwater echo ranging using Fessenden's transducer, which was capable of acting as an underwater receiver as well as a transmitter. The installation of *"Fessenden Oscillators"*, shown in Figure 1.1, on United States submarines during World War I was accepted as the first practical application of underwater electroacoustic transducers [3] [6].

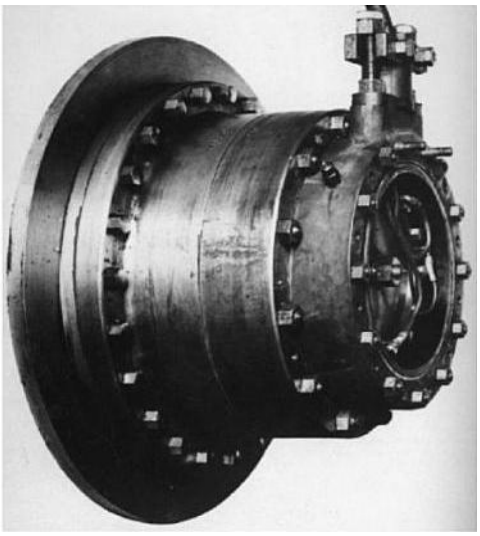

Figure 1.1: Fessenden's low frequency moving coil linear induction motor transducer [6]

Toward the start of World War I, it was understood that the only possible means for practical signaling through the water was sound waves since the electromagnetic waves were absorbed in a short distance in water. In the beginning of the war, when a significant submarine menace appeared, many underwater echo ranging experiments and researches were initiated. In France, Paul Langevin achieved some success in receiving echoes from targets at short distances by using an electrostatic transducer as a projector and a waterproofed carbon microphone as a hydrophone. In the meantime, British investigations were carried out by a group under R. W. Boyle. However, the numerous troubles

encountered in these researches exhibited the necessity of the improved transducers. Both Langevin and Boyle realized that quartz was a suitable material for improved transducers due to the piezoelectric effect in it. Then, in 1917, better results were obtained when Langevin used quartz hydrophone and transducers for the first time [6]. After these improvements, echoes were received from a submarine in early 1918 with an active system, where a quartz transducer was driven at 38 kHz [3].

In 1919, the first scientific paper on underwater acoustics was published by Germans, theoretically describing the refraction of sound rays produced by temperature and salinity gradients in the ocean, and recognizing their effect on the sound ranges. The range predictions in the paper were experimentally verified by transmission loss measurements conducted in all seasons of the year in shallow-water areas [4].

After the end of the World War I, the depth sounding by ships continued for commercial applications, and in 1925, Submarine Signal Company developed *"fathometer",* a name for their own depth sounder [4]. On the other hand, the researches for echo ranging on submarines were carried out in the United States primarily at the Naval Research Laboratory under H. C. Hayes. After the need for more powerful transducers was noticed, the researches focused on the magnetostrictive projectors, which were able to produce greater acoustic power. Nevertheless, lower efficiency of magnetostrictive materials resulted from the electrical and magnetic losses turned the researches to piezoelectricity again. As a result, Rochelle salt was found as a stronger piezoelectric material than quartz and became available in the form of synthetic crystals [6].

In the interwar period, the most remarkable accomplishment is the better understanding of sound propagation in the sea medium. Early echo ranging equipments were able to give accurate results only in the morning and poor echoes were obtained in the afternoon, which was called *"afternoon effect"* by E. B. Stephenson. The reason for this effect was that slight thermal gradients refract sound into the depths of the sea and cause the target to lie in the area what is now known as *"shadow zone"*. In 1937, equipment called *"bathythermograph"* to monitor the thermal gradient in the sea was built by A. F. Spilhaus. Moreover, the absorption of the sound in the sea was clearly understood in this period and the values of absorption coefficients were determined accurately at the ultrasonic frequencies 20 to 30 kHz [4].

In World War II, the serious threat of German submarines revealed the inevitability of SONARs (SOund NAvigation and Ranging) and high performance transducers. Therefore, the researches focused on new man-made transduction materials that had better performance of piezoelectricity. Then, in 1944, A. R. von Hippel discovered piezoelectricity in permanently polarized barium titanate ceramics and, in 1954 he found even stronger piezoelectricity in polarized lead zirconate titanate (PZT) ceramics. Discovery of these materials initiated the production of modern piezoelectric transducers [6].

Today, lead zirconate titanate (PZT) is still being used in most underwater sound transducers. Furthermore, new transduction materials are being developed, such as lead magnesium niobate (PMN) and single crystals of related compounds, and magnetostrictive materials Terfenol-D and Galfenol. The production of piezoelectric ceramics and ceramic-elastomer composites in a wide variety of shapes and sizes with many variations of compositions led to the development and manufacture of innovative transducer designs [6].

1.4 Underwater Transducer Applications

Underwater applications extend in the frequency spectrum from about 1 Hz to over 1 MHz. Frequencies below 100 Hz is used for acoustic communication over thousands of kilometers in the oceans since the absorption of sound increases rapidly as the frequency increases [6]. On the other hand, depth sounding requires frequencies from 10 kHz to several hundreds of kHz depending on the water depth to be explored. Upper part of this frequency range is utilized for shallow waters whereas deep waters necessitate lower frequencies [8]. Some short-range active sonars use frequencies up to 1.5 MHz to obtain high resolution [6].

In this wide spectrum, a large number and variety of transducers is used for various naval applications. For example, two submerged submarines communicate with each other by means of a projector to transmit sound and a hydrophone to receive sound. On the other hand, for echo ranging, a projector and a hydrophone on the same ship are required whereas passive listening requires only a hydrophone. Moreover, hydrophones and projectors used on naval ships consist of large groups of up to 1000 or more transducers closely packed in planar, cylindrical, or spherical arrays, as illustrated in Figure 1.2 [6].

Military applications are definitely the most common area of usage of underwater transducers. The most significant among these applications is sonars, which are acoustic equivalent of radars. There are two main types of sonars; active sonars and passive sonars. Active sonars transmit a signal and listen for the echoes from a target, which requires both projector and hydrophone arrays. The distance to the target can be determined by the time between transmission of the pulse and reception of the echo. They use frequencies around 1 kHz or

less. On the other hand, passive sonars, which include only hydrophone arrays, listen for the sound without transmitting. Operating at very low frequencies, between a few tens of Hz and a few kHz, allows longer detection ranges than active sonars [8].

Figure 1.2: Submarine sonar spherical array undergoing tests [6]

One of the other military applications is acoustic mines. These mines generally listen passively with a hydrophone sensitive to low-frequency sound, as illustrated in Figure 1.3, radiated by passing ships or submarines. They can also be sensitized to the sound of specific engines or other acoustic signatures, and can be equipped with detectors of magnetic field and hydrostatic pressure variations in order to be able to distinguish the target from other vessels. Moreover, modern acoustic mines are capable of working in active mode, as active sonars [8] [9].

Figure 1.3: Low frequency cylindrical hydrophone with isolation mounting system [6]

As a counter measure for acoustic mines, mine-hunting sonars are developed. These systems echo range at high frequencies (generally between 100 kHz and 500 kHz) with a short pulse length in order to provide acoustic images of the seabed with high resolutions for identification of mines on the seabed or floating in mid-water. After the mines are detected, minesweeping systems trigger the explosion of them by mimic the sound of the targets for these mines [8].

Similar to sonars, torpedoes have active or passive homing systems, or both to detect and steer toward their targets. Active homing systems echo range at high frequencies while lower frequencies are required for passive ones, which listen to the radiated noise of the target [4]. There are also torpedo countermeasure systems, which mask or simulate the target echo and the target radiated noise [10].

On the other hand, sonobuoys, which are dropped into the water from an aircraft in order to detect underwater objects, are expendable sonar/radio transmitter combinations. The radio floats on the surface while the hydrophone is submerged at a suitable depth, which can be seen in Figure 1.4. There are two types of sonobuoys; active ones that echo range and passive ones that only listen. However, both types send the signal received by their hydrophone to the aircraft [6].

Figure 1.4: A sonobuoy listening to the underwater and sending the information to the aircraft

There are also nonmilitary applications of underwater transducers. First of all, navigation is the starting points of many underwater acoustic systems. For navigation of naval vehicles, many devices such as single-beam depth sounders, beacons, transponders, Doppler logs etc. have been developed and used. The single-beam depth sounders are a form of active sonars to measure the depth

under a hull whereas upward-looking depth sounders are used for navigating under ice. On the other hand, the beacons, which are fixed at dangerous zones to navigate, transmit an acoustic signal and an optical or radio signal simultaneously and thus allow the vehicles to measure their distance from these zones by the time delay between the two signals. The transponders are more sophisticated that they allow dialogue using coded signals. Another device for navigation is Doppler logs, which are used to measure the velocity of the sonar and its supporting platform relative to a fixed medium, usually seabed, by using the frequency shift of echoes [5] [8].

Furthermore, by depth sounding, not only the water depth at a point can be detected, but also a detailed bottom map can be obtained. Today, bottom maps exist for a large portion of Earth's 140 million square miles of ocean [6]. For seafloor mapping, three types of acoustic system are extensively used: single-beam sounders, side-scan sonars and multibeam sounders. Single-beam sounders transmit a short signal between 12 kHz and 700 kHz downward, vertically, inside a narrow beam and measure the local water depth from the time delay of the echo, as mentioned before. On the other hand, side-scan sonars, which are placed on a platform towed close to the bottom, are used for acoustic imaging of the seabed with a resolution of a few tens of centimeters by transmitting a signal with frequencies of 100 to 500 kHz in a direction close to the horizontal. The backscattered signal by the seabed provides an image of irregularities, obstacles and changes in structure. Finally, multibeam sounders are the dominant acoustic system used in seafloor mapping. They transmit and receive a fan of beams (100 to 200 beams) with small individual widths (1-3°) and sweep a large corridor around the ship's path (a total width of 150°). Deepwater multibeam sounders operate at 12 kHz for deep ocean and at 30 kHz for continental shelves, whereas shallow-water ones use frequency range of 100 to 200 kHz. There are also high resolution systems operating between 300 and

500 kHz for local studies [8]. Moreover, seafloor mapping techniques are used in oceanography to determine the bottom characteristics. For example, the reasons for the decrease in the scallop population in the bottom of Peconic Bay, Long Island, New York have been investigated by sonars. Bottom mapping with sonar can also be extended to the exploration of sunken objects as ship and aircraft wreckage, ancient treasure etc [6].

Fisheries acoustics is another significant commercial application, where forward or side-looking active sonars are utilized for mainly detection of fish schools. Moreover, locating the isolated individual fish, and quantification of fish and other marine organisms are performed in the same way. Sounders used for these purposes are required to have high energy levels at transmission due to the low target strengths. The frequency range is commonly between 20 kHz and 200 kHz [8].

Underwater sound is also useful in ocean engineering in the determination of the specific locations when drilling for oil or gas deep in the ocean or laying underwater cables or pipelines. Similarly, finding the deposits of oil or gas under the oceans can be achieved by means of underwater acoustics [6].

Finally, there are several research projects where underwater sound is a significant issue. For example, the *Acoustic Thermometry of Ocean Climate project (ATOC)* is about the prediction of global warming from the changes in speed of sound. Since changes in speed of sound are primarily caused by changes in the temperature of the ocean, it may be one of the best measures of global warming. The technique depends on the determination of the speed of sound by measuring the time that takes for sound signals to travel between an acoustic source and a receiver separated by thousands of kilometers. Due to the

long path, i.e. 100-5000 km, very low frequency projectors and hydrophones are required in this project [11]. On the other hand, the *Sound Surveillance System (SOSUS)*, which was originally initiated by United States Navy for tracking Soviet submarines, is now being used for studying the vocalizations of whales and other ocean mammals, and for detection of earthquakes and volcanic eruptions under the sea [12] [6]. Furthermore, it is planned to mount acoustic sensors on Jupiter's moon Europa sometime around 2020. There are some cracks in the ice covering the surface of the Europa, which generate sounds in the ice and in the ocean under the ice. By means of these sounds received by acoustic sensors, the ice thickness and the depth and temperature of underlying ocean may be interpreted. Therefore, some clues about the possible existence of extraterrestrial life may be obtained [6]. One another research area in which underwater sound may play a role is particle physics if the sounds caused by high energy neutrinos passing through the ocean can be detected by hydrophone arrays [6].

All these applications of underwater sound require large numbers of transducers, with a great variety of special characteristics for use over a wide range of frequency, power, size, weight, and water depth. The problems raised and numerous possibilities for solutions make underwater transducer research and development a challenging subject.

1.5 Piezoelectricity & Piezoelectric Materials

Piezoelectricity can be defined as a coupling between the mechanical and electrical state in certain crystalline materials that lack a center of symmetry [13]. If a piezoelectric material is subjected to a mechanical force, it becomes electrically polarized. In other words, an electrical potential and electric field is

generated in the material in proportion to the magnitude of the applied force. Conversely, when a piezoelectric material is exposed to an electric field, it mechanically deforms in proportion to the strength of the field. These behaviors are called the *"direct piezoelectric effect"* and the *"converse (inverse) piezoelectric effect"*, respectively, from the Greek word piezein, which means to squeeze or press. These effects were observed first by Jacques and Pierre Curie in 1880 [14].

A piezoelectric crystal is a pile of perovskite crystals, which consist of both positive and negative ions. Although above a critical temperature, the Curie point, each perovskite crystal has a simple cubic symmetry with no electric dipole moment, below the Curie point, each crystal has tetragonal or rhombohedral symmetry and an electric dipole moment. Neighboring dipoles make regions of local alignment called domains. Even though each domain has a net polarization, the direction of polarization among adjacent domains is random. Therefore, the crystal has no overall polarization (Figure 1.5a) [14].

The domains are aligned by applying a strong, direct current electric field at a temperature slightly below the Curie point to the crystal, which is called *"polarizing (poling)".* During the polarizing treatment, the domains are aligned with the electric field and they are symmetrically distributed within the crystal so that the crystal as a whole is electrically neutral (Figure 1.5b). This alignment is nearly conserved even after the electric field is removed. Thus, the polarization is permanent (Figure 1.5c) [14] [15] [16].

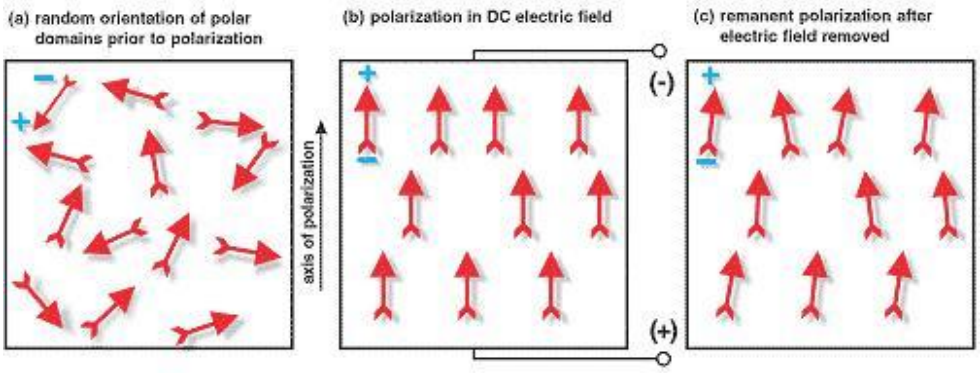

Figure 1.5: Orientation of polar domains before, during and after polarization treatment [14]

When a mechanical stress is applied on the crystal, however, the symmetry is slightly broken and the charge asymmetry generates a voltage. Compression along the direction of the polarization or tension perpendicular to the direction of the polarization causes voltage with the same polarity as the poling voltage (Figure 1.6b), whereas voltage with the opposite polarity as the poling voltage is generated by tension along the direction of the polarization or compression perpendicular to the direction of the polarization (Figure 1.6c). These energy conversions from mechanical energy to electrical energy are *generator actions* of piezoelectric material. On the other hand, a voltage with the same polarity as the poling voltage causes the piezoelectric element to become longer and narrower (Figure 1.6d) while a voltage with the opposite polarity as the poling voltage causes it to become shorter and broader (Figure 1.6e). Moreover, an alternating voltage leads the element to lengthen and shorten cyclically, at the frequency of the applied voltage. Electrical energy is transformed to the mechanical energy by these actions, which are *motor actions* of the piezoelectric material [14]. The mathematical description of piezoelectricity is given in Appendix A.

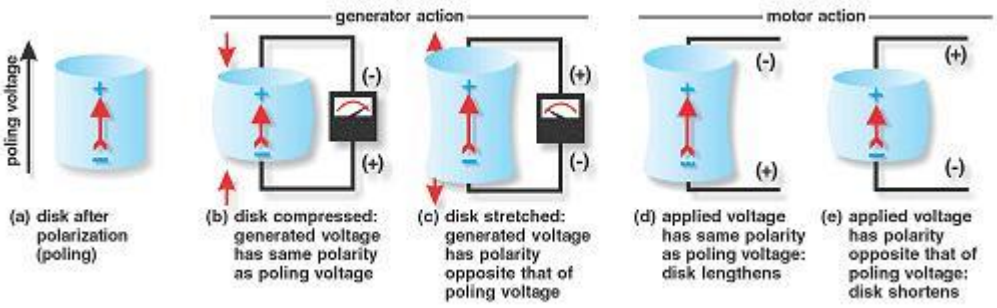

Figure 1.6: Generator and motor actions of a piezoelectric element [14]

Piezoelectricity occurs in many crystalline materials. Some of them are naturally occurring crystals and the others are man-made crystals and ceramics. *Quartz*, which is a naturally occurring crystal, was the first piezoelectric material discovered. Moreover, *Berlinite ($AlPO_4$), tourmaline, topaz, cane sugar and Rochelle salt* are some other naturally occurring crystals that exhibit piezoelectricity. On the other hand, *gallium orthophosphate ($GaPO_4$) and Langasite ($La_3Ga_5SiO_{14}$)* are some made-made piezoelectric crystals whereas *barium titanate ($BaTiO_3$), lead titanate ($PbTiO_3$), lead zirconate titanate (most commonly known as PZT), potassium niobate ($KNbO_3$), lithium niobate ($LiNbO_3$), lithium tantalate ($LiTaO_3$), sodium tungstate (Na_2WO_3), $Ba_2NaNb_5O_5$, $Pb_2KNb_5O_{15}$* are some man-made ceramic-based piezoelectric materials. Furthermore, *rubber, wool, hair, wood fiber, and silk* are some polymers which have piezoelectric properties to some extent. *Polyvinylidene fluoride (PVDF)* exhibits several times stronger piezoelectricity than quartz, by means of the attraction formed between long-chain molecules in response to the applied electric field [13] [16]. Among all these piezoelectric materials, lead zirconate titanate (PZT) is the most widely used one.

There are so many applications where piezoelectricity is used. These applications can be classified into four main categories: *generators, sensors,*

actuators and electroacoustic transducers. In generators, the piezoelectric ceramics are used as igniters in fuel lighters, gas stoves, welding equipment etc. by generating voltages sufficient to spark across an electrode gap [14]. Moreover, piezoelectricity is employed in transformers, which are a type of AC voltage multiplier. In this type of transformers, firstly, an alternating stress is created in a bar of a piezoelectric ceramic from an input voltage by inverse piezoelectric effect, which causes the bar to vibrate. Selecting the vibration frequency as the resonant frequency of the bar increases the amplitude of the vibration. Then, this increased vibration is converted into a higher output voltage by direct piezoelectric effect [13].

Piezoelectric sensors transform a physical parameter such as pressure or acceleration to an electric signal by means of the direct piezoelectric effect. In these sensors, the physical parameter generally creates vibrations in the piezoelectric element and these vibrations are, then, converted into an electric signal [14]. On the other hand, actuators perform transformation from an electrical signal to a mechanical movement. This movement is so small that better than micrometer precision can be obtained with a piezoelectric actuator. Loud speakers, piezoelectric motors, acousto-optic modulator, atomic force microscopes, scanning tunneling microscopes, inkjet printers, fuel injectors in high performance common rail diesel engines are some examples where inverse piezoelectric effect are employed by piezoelectric actuators [13].

Finally, piezoelectric electroacoustic transducers achieve transformation between electrical energy and vibrational mechanical energy, or sound. For example, ultrasonic transducers consist of piezoelectric crystals in order to generate sound from the input electrical energy by inverse piezoelectric effect and to convert incoming sound into an electrical signal by direct piezoelectric effect. Piezoelectric transducers are also employed for cleaning, atomizing

liquids, drilling or milling ceramics or other difficult materials, welding plastics, medical diagnostics etc. by means of ultrasonic vibrations [14].

1.6 Scope of the Current Study

In this study, a piezoelectric electroacoustic transducer is designed for underwater use. The results found with the help of a finite element modeling (FEM) software, ANSYS, are compared with the results of the tests conducted in Bilkent Acoustics and Underwater Technologies Research Center (BASTA). The transducer designed consists of two piezoelectric elements so it operates in two distinct frequency bands. It is used as a projector, which transmits acoustic signals by converting electrical energy into acoustic energy by means of the mechanical vibrations of the piezoelectric elements.

There are 4 main parts in the thesis. The first part is the introductory one, Chapter 1, which includes the basic information about transducers such as the definition of a transducer, the applications and types of transducers, history of underwater acoustics and electroacoustic transducers, underwater transducer applications and piezoelectricity. Then, the literature survey is presented in Chapter 2. After the design process is explained in detail in Chapter 3, the results are discussed in Chapter 4.

CHAPTER 2

LITERATURE SURVEY

In this chapter, noteworthy past researches in the area of underwater transducers are reviewed. There are many studies in this topic; some give general information about underwater acoustic and ultrasonic transducers and others discuss the specific types of underwater transducers.

Gallego-Juarez [17] reviewed the basic characteristics of piezoelectric ceramics. He also reported the application of these materials in practical ultrasonic transducers. According to Juarez, the choice of a piezoelectric material depends on the application for which the transducer will be used. He discussed that high permittivity and elastic compliance can be favorable in obtaining adequate values for the electrical impedance for low and medium ultrasonic frequencies, i.e., between 20 and a few hundred kHz. However, low permittivity and elastic compliance are convenient for higher frequencies. The paper also includes the properties of typical piezoelectric ceramics and compares them. Moreover, in the paper, they were classified according to the applications they are suitable for. Juarez explained that the simplest piezoelectric transducer is composed of a single element operated in one of its possible vibration modes according to the axis of polarization. He classified the transducers into two main groups: narrow-band (a few percent bandwidth) and broad-band (30-70% bandwidth) transducers. Narrow-band transducers are frequently used in high-intensity

applications usually at low frequencies, i.e. 20-100 kHz, whereas broad-band ones are generally utilized in detection, measurement and control applications with very short ultrasonic pulses in the frequency range of 0.5-50 MHz. Juarez also summarized the specific types of transducers in his paper.

In another paper, Juarez with Chacon, Corral, Garreton and Sarabia [18] presented a numerical and experimental procedure for the accurate selection of the piezoelectric rings in a piezoelectric sandwich transducer. Their procedure is based on the measurement of geometrical, mechanical and electrical parameters together with a numerical characterization of the vibration modes of the ceramic rings. In the paper, the resonance frequencies were founded by FEM and the vibration curves of these modes were analyzed in order to determine the thickness mode. They were also experimentally verified by electrical measurements with an impedance analyzer and the measurement of the vibration velocity distribution with laser vibrometry. Moreover, the thickness modes of the piezoelectric ceramic rings with different diameter-thickness ratio were compared.

Silva and Kikuchi [19] presented the main goals in the transducer design as high electromechanical energy conversion for a certain transducer vibration mode, specified resonance frequencies and narrowband or broadband response. According to them, the transducer is required to oscillate in the piston mode for more acoustic wave generation applications. Moreover, the transducer must be designed to have a broadband or narrowband frequency response which defines the kind of acoustic wave pulse generated (short pulse or continuous wave, respectively). The requirements also include an assurance of the specified mechanical resonance frequency, an absence of spurious resonances close to the working frequency and a high quality factor (Q_m) including minimum energy dissipation in the material and in the attachments. They also proposed a method

in order to design piezoelectric transducers that achieve these goals, based upon topology optimization techniques and finite element method.

Tressler [20] described the fundamental parameters and measurement techniques necessary to characterize transducers both in air and in water. Moreover, he reviewed the piezoelectric ceramic materials that are most commonly used in sonar transducers and their relevant material properties. Finally, he explained the most common piezoelectric ceramic-based projector designs.

Kunkel, Locke and Pikeroen [21] analyzed the natural vibrational modes of piezoelectric ceramic disks by FEM. They studied the dependence of the vibrational modes on the disk diameter-to-thickness ratio for several ratios. The resonance and anti-resonance frequencies, the electro-mechanical coupling coefficients and model displacement fields were found.

Yao and Bjorno [22] designed a broadband, high power tonpilz transducers using FEM. They analyzed the longitudinal piston mode and flapping mode for in-air and in-water situations.

Lin, Xu and Hu [23] studied a composite transducer that consists of a sandwich longitudinal piezoelectric transducer, an isotropic metal hollow cylinder with large radial dimension, and the front and back metal radiation mass. In their paper, they founded the resonance frequency analytically by electrical equivalent circuit model method. Then, they simulated the vibration of the transducer, the vibrational displacement distribution, the resonance frequency and the radiation sound field by numerical methods. Finally, they manufactured some transducers and measured the resonance frequency and the radiation

acoustic field in order to compare them with the analytical and numerical results.

In another paper, Lin and Xu [24] presented the analysis of a sandwich transducer with two sets of piezoelectric ceramic elements. They studied the relationship between the electromechanical coupling coefficient, the resonance/anti-resonance frequencies and the geometrical dimensions of the transducer both by analytically (electrical equivalent circuit model method) and experimentally.

Similarly, Lin and Tian [25] studied the thickness vibration of a sandwich piezoelectric ultrasonic transducer. They analyzed a piezoelectric ceramic stack consisting of a number of identical piezoelectric ceramic rings and obtained the electrical equivalent circuit of the transducer. Then, they found the resonance frequency equation from the equivalent circuit. Moreover, they manufactured two sandwich piezoelectric transducers and confirmed the theoretical results with the measurements.

Lin [26] also studied an improved cymbal transducer that consists of a combined piezoelectric ring and metal ring, and metal caps. The radial vibration was analyzed and electrical equivalent circuit of the transducer was obtained. The relationship between the resonance/anti-resonance frequency, the effective electro-mechanical coupling coefficient and geometrical dimensions were analyzed by numerical method. Moreover, the vibrational modes of the transducer were analyzed by the admittance curve and vibrational displacement distribution. Finally, the transducers designed were manufactured and resonance/anti-resonance frequencies and admittance curves measured were compared with the numerical results.

Tressler, Newnham and Hughes [27] developed a cymbal transducer for use as a shallow-water sound projector at frequencies below 50 kHz. The transmitting response of their transducer was comparable to the more widely used Tonpilz transducer and could withstand exposures of 2.5 MPa hydrostatic pressure before failure.

Sun, Wang, Hata and Shimokohbe [28] investigated the axial vibration characteristics of a cylindrical, radially polarized piezoelectric transducer by three different methods: analytical calculation, FEM simulation and experiment. In their study, the results from the three methods coincided well with each other whereas there were some deviations between the FEM simulation and measurement results in terms of the vibration amplitude. Moreover, they analyzed the influence of the electrode patterns on the excitation modes in detail.

Kim, Hwang, Jeong and Lee [29] [30] studied the radial vibration characteristics of cylindrical piezoelectric transducers polarized in the radial direction. They derived a formula in terms of radial displacement and electric potential for calculating the piezoelectric natural frequency of these transducers. They also confirmed the validation of the formula by experiments. Furthermore, they discussed the effect of the piezoelectricity on the natural frequency, and the dependence of the piezoelectric natural frequency on the radius and thickness of the piezoelectric cylinder. According to them, the frequency of the fundamental mode did not depend significantly on the thickness of the cylinder.

Again Lin and Liu [31] [32] studied the radial vibration characteristics of a composite piezoelectric transducer that consists of a piezoelectric ceramic ring polarized in axial direction and a metal circular ring. He obtained the electrical

equivalent circuit of the entire transducer from the equivalent circuits of the each component and boundary conditions between them. From the equivalent circuit, he could derive the resonance frequency equation and analyzed the relationship between the resonance frequency and the geometrical dimensions. Then, he manufactured some transducers and confirmed the theoretical results with the measurements.

Feng, Shen and Deng [33] proposed a 2D equivalent circuit of longitudinally polarized piezoelectric ceramic ring from the approximated analytical solution of 3D constitutive equations in the hypothesis of axial symmetry when the shearing stress and torsion is ignored. The model could give the relations between the input applied voltage and the output forces and velocities on every external surface analytically. Moreover, they determined the resonance frequency of the radial and thickness vibration modes of a thin ring and described the coupled vibration of a fairly thick ring. The model was also applicable to piezoelectric disk.

A similar study was performed by Lin [34]. He derived an electrical equivalent circuit model of a piezoelectric thin circular ring polarized in the thickness direction and analyzed the relationship between the resonance frequencies and the material parameters and the geometrical dimensions.

Ramesh, Prasad, Kumar, Gavane and Vishnubhatla [35] carried out numerical (FEM) and experimental studies on 1-3 piezocomposite transducers, which have two-phase materials consisting of piezoelectric and polymer components. They initially applied FEM to a piezocomposite infinite plate and then extended to transducers of finite size. Moreover, they analyzed the acoustic performance of multi-layer finite-size piezocomposite transducers. After manufacturing

transducer stacks with different number of layers, they evaluated the transducer characteristics such as the electrical impedance, the transmitting voltage response (TVR) and the receiving sensitivity (RS) of the 1-3 piezocomposite transducers as functions of frequency, ceramic volume fractions and the number of layers.

Similarly, Andrade, Alvarez, Buiochi, Negreira and Adamowski [36] compared the resonant characteristics and the surface vibration modes between a homogenous piezoelectric ring and a 1-3 piezocomposite ring. They validated the analytical models and FEM results with electrical impedance measurements and the surface acoustic spectroscopy method.

CHAPTER 3

DESIGN

In this study, the design process consists of two main phases: numerical design and experimental design. Firstly, the process starts with the numerical design. In this phase, a finite element method (FEM) software, ANSYS, is used. After the numerical design is completed, the transducer designed is manufactured. At this point, the experimental design phase begins and some tests are applied to the transducer. Finally, the results of both phases are compared and discussed.

3.1 Numerical Design

Numerical design is the starting point of the design process. In this phase, the design of the transducer is performed in terms of three main aspects: acoustic performance, mechanical performance and thermal performance. Among these aspects, the most significant and deterministic one is acoustic performance. After the design is accomplished according to the acoustic requirements, it is checked in terms of mechanical and thermal performances.

3.1.1 Acoustic Performance

Acoustic performance of an underwater electroacoustic transducer is related to the effectiveness and efficiency with which the transducer converts the input electrical energy into acoustic signals. The frequency, bandwidth and amplitude of the signal are the main parameters which determine the acoustic performance. These parameters depend on some design criteria, such as type, shape and dimensions of the piezoelectric materials used. In the next section, the design of the piezoelectric materials including the determination of type, shape and dimensions are explained.

3.1.1.1 Design of the Piezoelectric Material

In this study, cylindrical piezoelectric ceramic tubes are used because of their high strength and reliability, relatively low cost and ease of manufacturing. Due to the capability of being driven with high power, PZT4 is preferred as the type of the piezoelectric material. The tubes are selected to be polarized in the radial direction and will be operated in *"3-1 mode"* since procurement of radially polarized tubes is more easy and inexpensive. In 3-1 mode notation, the first digit, *"3"*, represents the polarization direction, whereas the second digit, *"1"*, represents the direction of primary stress and strain formed. In the radially polarized cylindrical tubes, direction 1 is along the circumference, 2 is along the length, and 3 is radial [6]. Therefore, the tubes in this study will be operated in a cylindrical vibration mode where the primary stress and strain are in the circumferential direction. This mode is designated as *"circumferential expansion mode"* in the rest of the text.

After the type and shape selection, the dimensions of the tubes are determined. For this task, two approaches are used: *electrical equivalent circuit model method (EECMM)* and *finite element method (FEM)*. At this point, the acoustic requirements, especially the operating frequencies of the transducers, must be specified since the dimensions of the tubes have to be assigned according to these requirements. In this study, one of the tubes will operate at about *30 kHz* and the other one at about *60 kHz*. Firstly, the dimensions that meet the requirements are found by trial and error with EECMM. The details about this method are given in Appendix B. The dimensions found by means of equivalent circuit and the other properties of the piezoelectric material used in the study are shown in Table 3.1.

Table 3.1: Properties of the piezoelectric material used in this study

Shape	Cylindrical Tube				
Type	PZT4				
	Inner Diameter	***Outer Diameter***	***Thickness***	***Length***	***Unit***
Tube1	14	20	3	10	mm
Tube2	26.7	30.5	1.9	25.4	mm

The electrical admittances of the tubes found by using electrical equivalent circuit model method are shown in Figure 3.1 and Figure 3.2.

The resonance frequencies, bandwidths and electrical admittances of the tubes in the circumferential expansion mode, found with equivalent circuit, are given in Table 3.2.

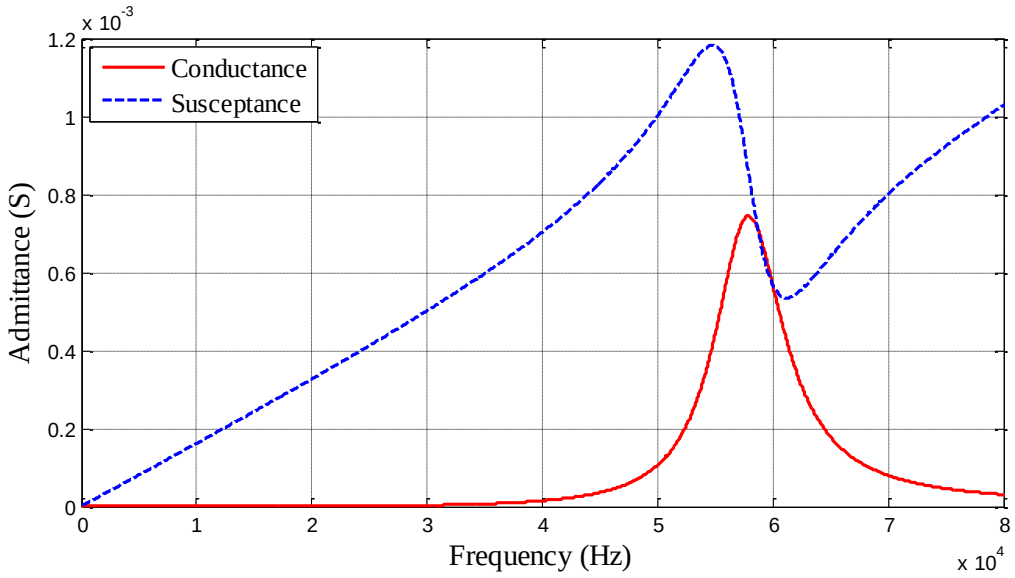

Figure 3.1: Electrical admittance of Tube1 found by using electrical equivalent circuit model method

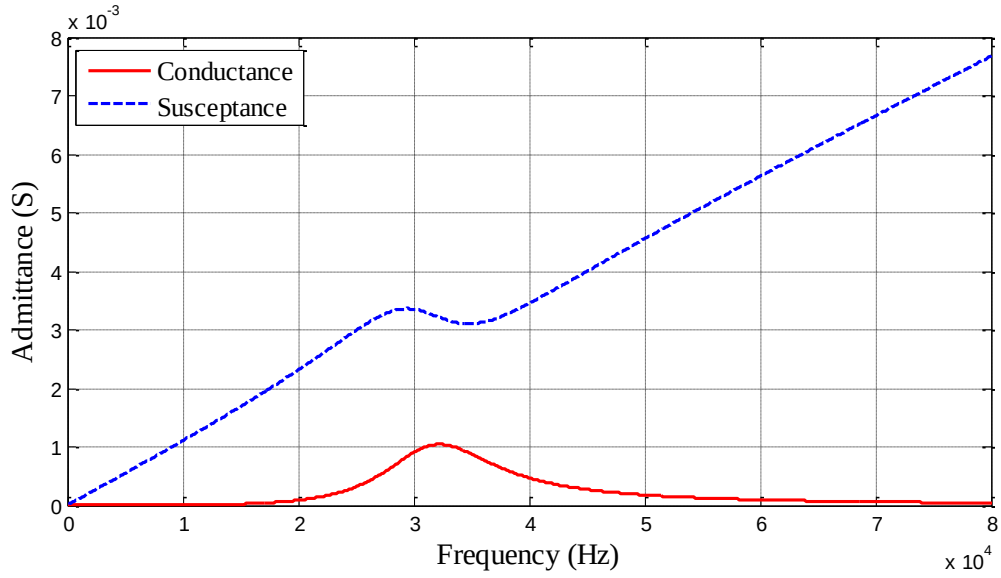

Figure 3.2: Electrical admittance of Tube2 found by using electrical equivalent circuit model method

Table 3.2: Results of electrical equivalent circuit model method

	Resonance Frequency (kHz)	***-3 dB Bandwidth (kHz)***	***Fractional Bandwidth (%)***	***Electrical Admittance (mS)***
Tube1	57.9	7.4	12.6	0.75 + j 0.85
Tube2	32.3	12.1	36.5	1.04 + j 3.23

From the results, the dimensions selected for the tubes seem to be appropriate for operating requirements. However, the electrical equivalent circuit model method is simplified since it has some assumptions. For example, the radiation impedance of a cylinder tube is approximated by an equivalent sphere of the same radiating area. Moreover, this method uses only S^{E}_{11} and d_{31} from the compliance matrix and piezoelectric matrix, respectively, by considering only circumferential expansion mode and ignoring the effects of the other vibration modes. For this reason, it assumes that the tubes have Poisson's ratio of zero and bending or contraction, which affects the radiation area and so radiation itself, does not occur in tubes. As a result, the admittances found by means of equivalent circuit include some deviations from the real values. In spite of these deviations, this method is an effective and rapid way of determining the dimensions.

After determining the dimensions of the cylindrical piezoelectric tubes, the real case should be understood more accurately and comprehensively. Thus, the other vibration modes as well as the circumferential expansion mode should be investigated with finite element method (FEM). For this task, the tubes are simulated in ANSYS so that all vibration modes can be analyzed. The details about the acoustic simulations of PZT tubes with FEM in ANSYS are given in

Appendix C. The electrical admittances of tubes found in ANSYS are shown in Figure 3.3 and Figure 3.4.

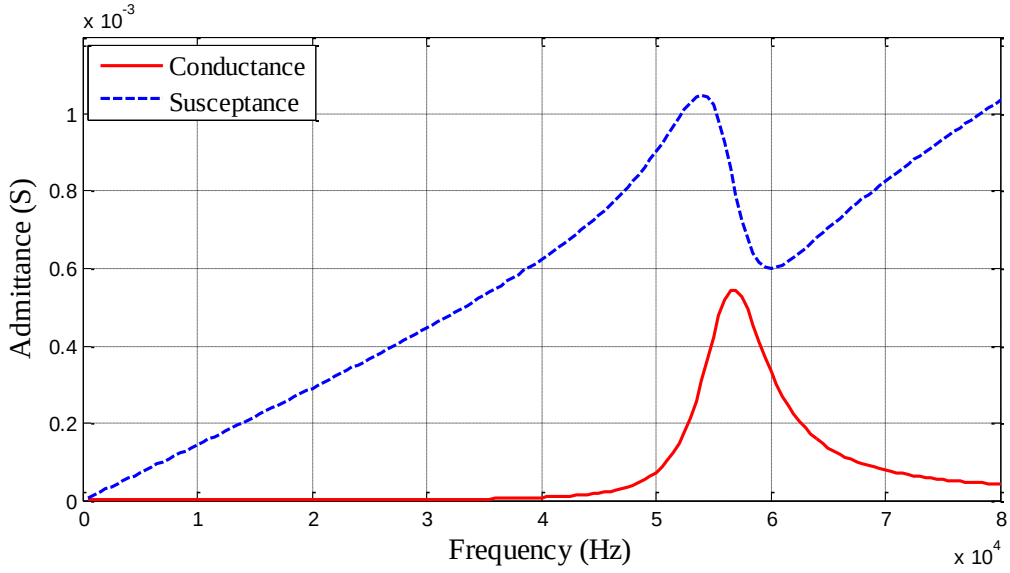

Figure 3.3: Electrical admittance of Tube1 found with FEM in ANSYS

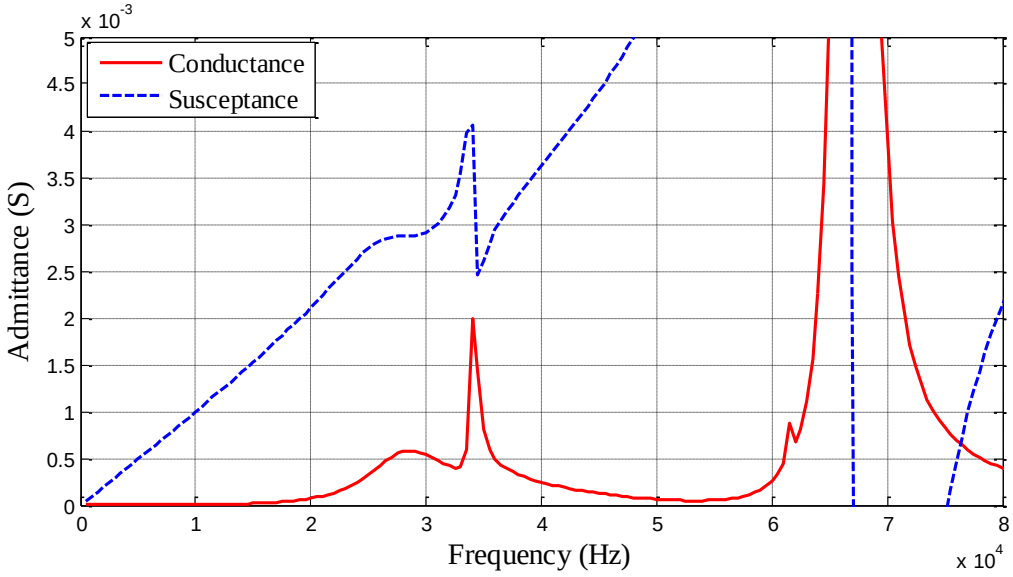

Figure 3.4: Electrical admittance of Tube2 found with FEM in ANSYS

As seen in the electrical admittance of Tube1, there is not any vibration mode of this tube other than circumferential expansion mode in the frequency range from 0 to 80 kHz. On the other hand, Tube2 has many vibration modes in the same range. The circumferential expansion mode, which is the operating mode, is centered at *28.5 kHz*, whereas there are three other modes centered at *34 kHz*, *61.5 kHz*, and *67 kHz*. The motions of Tube2 at these modes are shown in Figure 3.5. In the figure, the initial and deformed shapes of the axisymmetric model of the tube are shown.

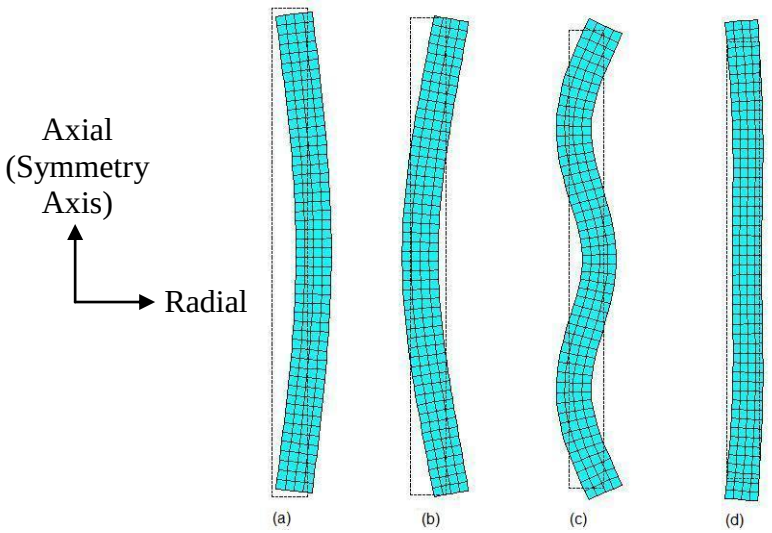

Figure 3.5: Initial and deformed shapes of the axisymmetric model of Tube2: (a) circumferential expansion mode at 28.5 kHz, (b) bending mode at 34 kHz, (c) shear mode at 61.5 kHz, (d) longitudinal mode at 67 kHz.

In the circumferential expansion mode, the tube switches back and forth as a whole, which results in a net displacement in the water (Figure 3.5a). Nevertheless, in the other modes, the tube bends or stretches and cannot create a net displacement in the water or can create relatively small net displacement. (Figure 3.5b, Figure 3.5c, Figure 3.5d). Instead, it mostly churns the water.

Therefore, the circumferential expansion mode is the only useful mode, which can transfer an acoustic power or acoustic signal to the water. As a result, the transducer will be operated in the circumferential expansion modes and the other modes must be kept away from the operating frequency bands.

The resonance frequencies, bandwidths and electrical admittances of the tubes in the circumferential expansion mode, found with FEM in ANSYS, are given in Table 3.3. The right-hand side of the band of Tube2 cannot be observed accurately because of the bending mode centered at 34 kHz so the bandwidth of Tube2 is approximated by linear interpolation.

Table 3.3: Results of FEM in ANSYS about tubes

	Resonance Frequency (kHz)	***-3 dB Bandwidth (kHz)***	***Fractional Bandwidth (%)***	***Electrical Admittance (mS)***
Tube1	57	7.31	12.8	0.55+j 0.79
Tube2	28.5	9.6	33.0	0.58+j 2.87

Designs of the piezoelectric materials finish here. However, the tubes cannot be used by themselves as a transducer since they will be submerged in water. For this reason, a frame and a coating are required. The designs of them are explained in the following section.

3.1.1.2 Design of the Frame and Coating

A frame and a coating are required for the following reasons:

- ❖ Holding the tubes coaxially and supporting them
- ❖ Protecting the tubes from impact, shock, hydrostatic pressure etc.

The design of the frame and coating is initiated by selecting the proper materials for them. The frame and coating should have the following properties:

- ❖ High stiffness and strength due to their task of protecting the tubes
- ❖ Light weight
- ❖ High corrosion resistance for operating in water
- ❖ High fatigue resistance due to the alternating stresses created by vibrations
- ❖ Not preventing the desired motions of the tubes by their own resonances

When considering the desired properties, *Carbon Fiber Reinforced Polymer (CRP)* is selected as the material of the frame and *Glass Fiber Reinforced Polymer (GRP)* as the coating material. The reason for these selections is the superiorities of composites over metals in terms of these aspects. Moreover, the anisotropic behavior of a fiber reinforced composite material gives a unique opportunity of tailoring its properties according to the design requirements. Therefore, this design flexibility can be utilized to selectively reinforce a structure in the directions of major stresses and to increase its stiffness in a preferred direction [37].

After deciding on the materials of the frame and coating, the design of the transducer is performed. In Figure 3.6, the cross-sectional drawing of the transducer with the names of the parts is shown.

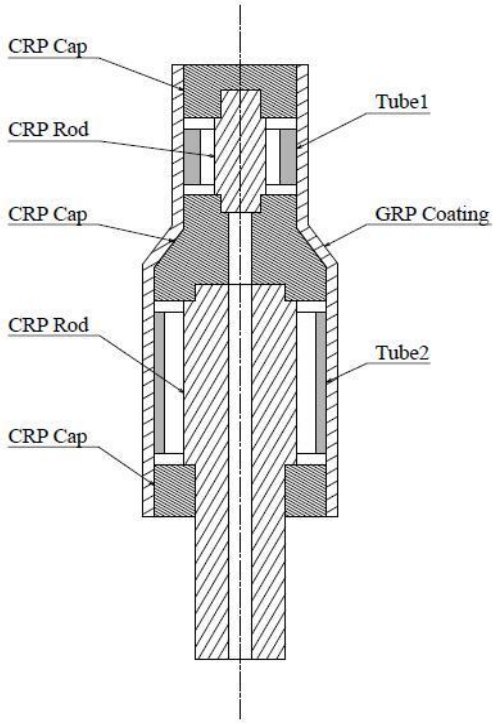

Figure 3.6: Cross-sectional drawing of the transducer designed

As seen in the figure, the transducer consists of *CRP Caps*, *CRP Rods*, *GRP Coating* and *PZT Tubes*. Although both CRP Caps and CRP Rods are made of T300 carbon fibers-epoxy matrix, they have different structures. CRP Caps are in laminated form including $[0/45/90/-45]_s$ fibers in order to prevent their bending (Figure 3.7a). However, CRP Rods are composed of unidirectional continuous carbon fibers in order to reinforce the structure in axial direction (Figure 3.7b). On the other hand, GRP Coating includes E-Glass fiber hoses with braid angle of 45°, i.e. woven fabric, impregnated with epoxy matrix so that the bending modes of the tubes can be sent away from the operating

frequency bands to higher frequencies (Figure 3.7c). Therefore, the formation of undesired motions in the operating bands can be prevented. The coating thickness is taken as ***2 mm*** in the design. The materials of the parts are tabulated in Table 3.4.

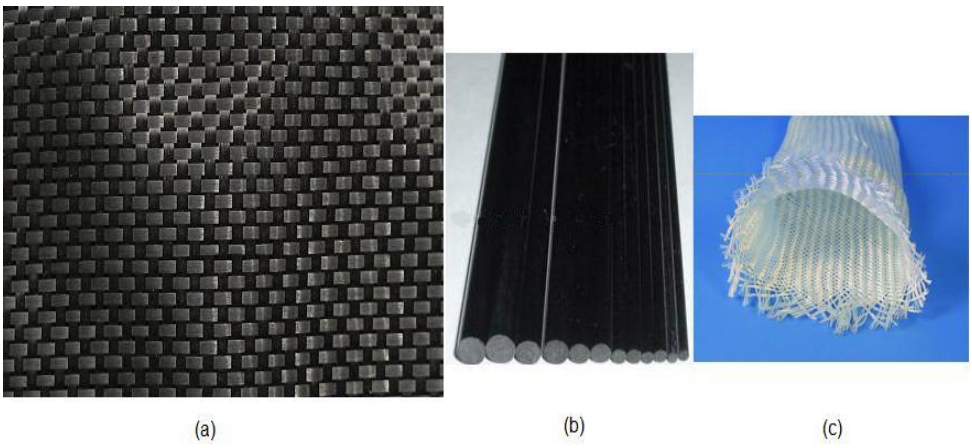

Figure 3.7: Composite structures used in the study: (a) carbon fiber sheet in laminated form, (b) unidirectional continuous carbon fiber rod, (c) glass fiber hose with braid angle of 45° [38] [39]

Table 3.4: Materials of the parts in the transducer designed

Component Name	***Material***
CRP Caps	Carbon fiber sheet in laminated form (T300 Carbon + Epoxy)
CRP Rods	Unidirectional continuous carbon fiber rod (T300 Carbon + Epoxy)
GRP Coating	Glass fiber hose in braided form (woven fabric) (E-Glass + Epoxy)
PZT Tubes	PZT4 piezoelectric ceramic tubes

The transducer shown in Figure 3.6 is simulated in ANSYS. The details about this acoustic simulation are given in Appendix D and the electrical admittances of tubes with frame found in ANSYS are shown in Figure 3.8 and Figure 3.9.

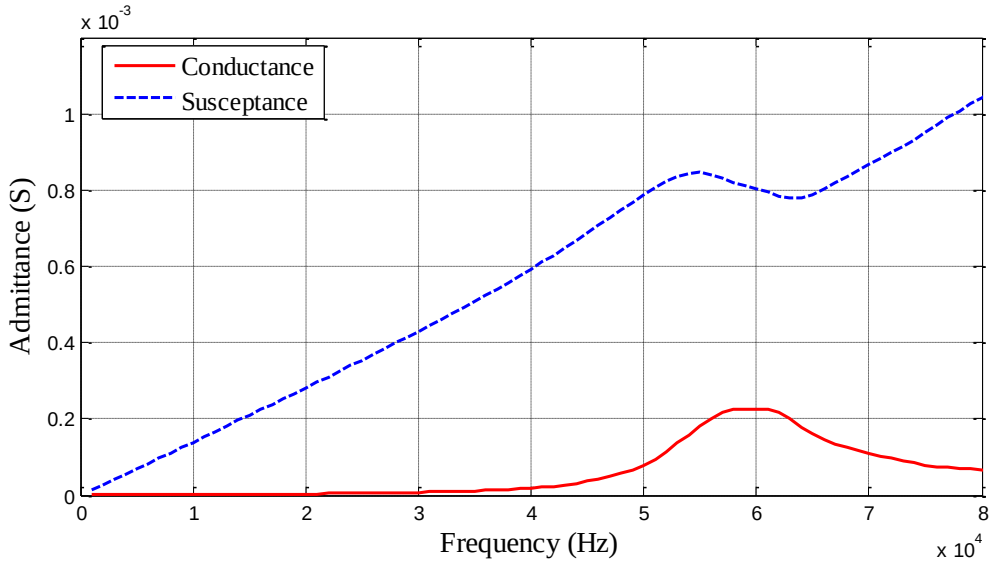

Figure 3.8: Electrical admittance of Tube1 with frame found with FEM in ANSYS

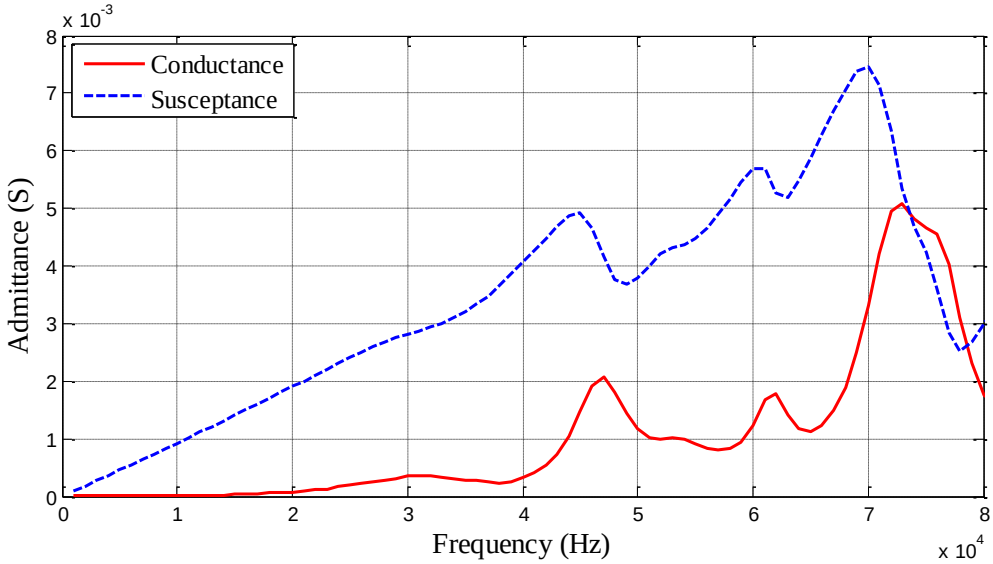

Figure 3.9: Electrical admittance of Tube2 with frame found with FEM in ANSYS

As seen in the electrical admittances of tubes with frame, Tube1 has only circumferential expansion mode in the frequency range from 0 to 80 kHz, whereas Tube2 has many vibration modes in the same range. The motions of the transducer at these modes are shown in the figures from Figure 3.10 to Figure 3.14. In the figures, the initial and deformed shapes of the axisymmetric model of the transducer with the values of radial displacement are shown.

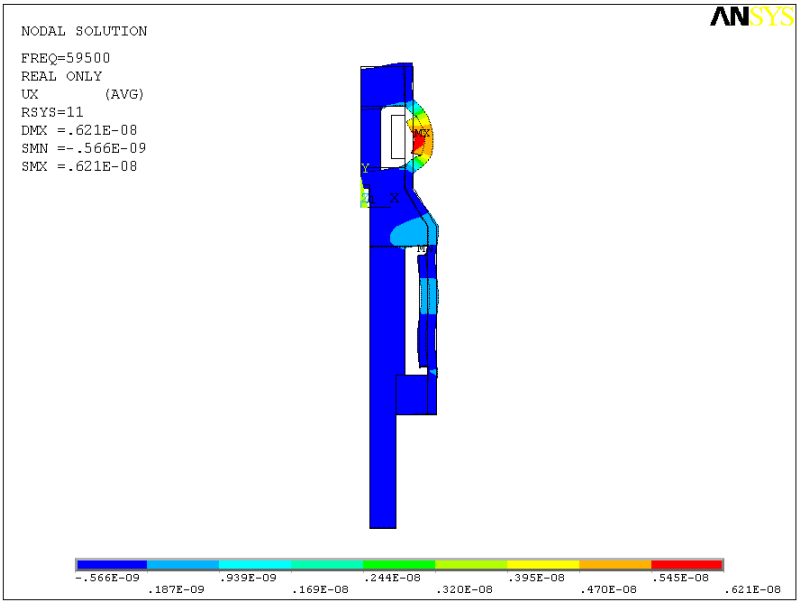

Figure 3.10: Initial and deformed shapes of the axisymmetric model of the transducer with the values of radial displacement when Tube1 is operated at its circumferential expansion mode (59.5 kHz)

In Figure 3.10, the circumferential expansion mode of Tube1 at 59.5 kHz is shown. As seen in the figure, the values of radial displacement at everywhere on Tube1 are positive, which results in a net displacement in water. In this mode, an acoustic power or acoustic signal can be transferred to the water so this is the operating mode of Tube1.

Figure 3.11: Initial and deformed shapes of the axisymmetric model of the transducer with the values of radial displacement when Tube2 is operated at its circumferential expansion mode (31 kHz)

In Figure 3.11, the circumferential expansion mode of Tube2 at 31 kHz is shown. Similarly, the values of radial displacement at everywhere on Tube2 are positive, which results in a net displacement in water. Therefore, this is the operating mode of Tube2, by which an acoustic power or acoustic signal can be transferred to the water.

In Figure 3.12, the bending mode of Tube2 at 47 kHz is shown. As seen in the figure, the values of radial displacement at top and bottom sections of Tube2 are positive while they are negative at middle section, which results in approximately zero net displacement in water. Therefore, in this mode, an acoustic power or acoustic signal cannot be transferred to the water. Instead, the tube only churns the water so this is a useless mode.

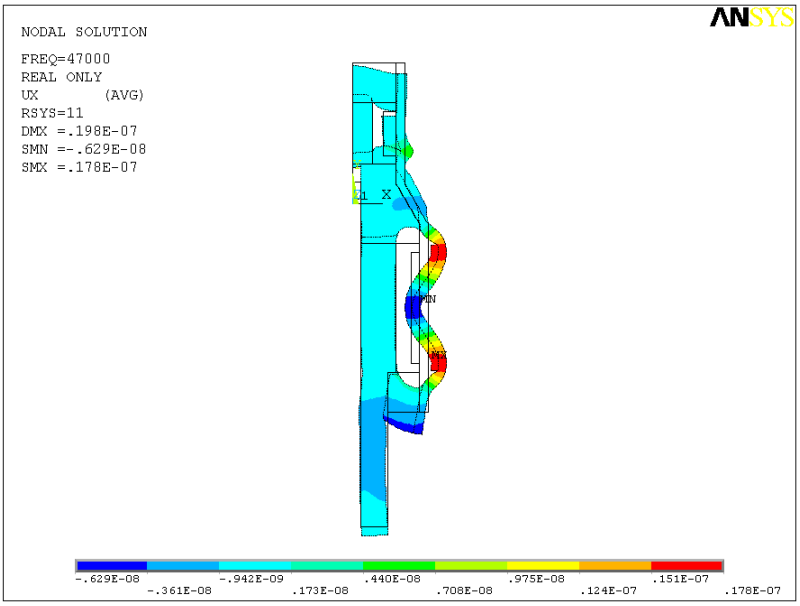

Figure 3.12: Initial and deformed shapes of the axisymmetric model of the transducer with the values of radial displacement when Tube2 is operated at its bending mode (47 kHz)

In Figure 3.13, the shear mode of Tube2 at 62 kHz is shown. In this mode, the radial displacement varies between positive and negative values on Tube2. Therefore, net displacement in the water is approximately zero. As a result, there is almost no acoustic power or acoustic signal transferred to the water and this mode is also useless.

In Figure 3.14, the longitudinal mode of Tube2 at 73 kHz is shown. As seen in the figure, the radial displacement has both positive and negative values on Tube2, which results in approximately zero net displacement in water. Therefore, this mode is also a useless mode.

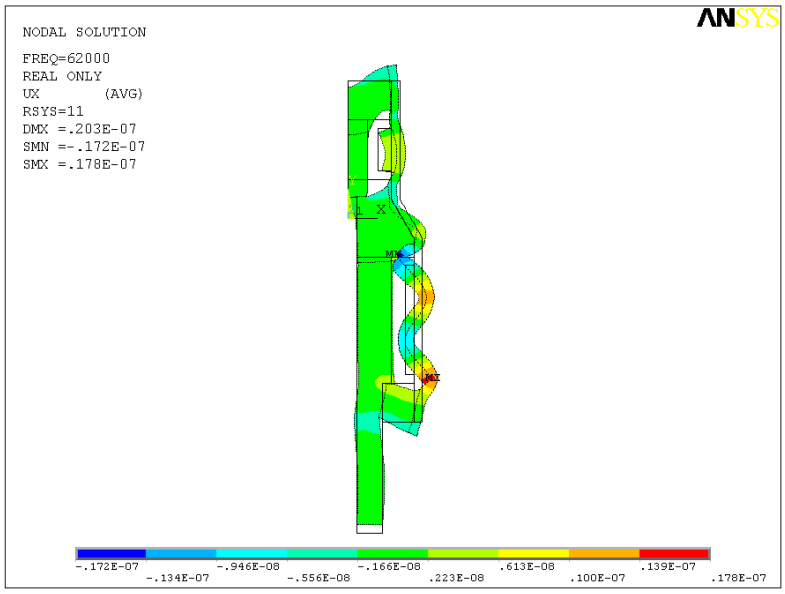

Figure 3.13: Initial and deformed shapes of the axisymmetric model of the transducer with the values of radial displacement when Tube2 is operated at its shear mode (62 kHz)

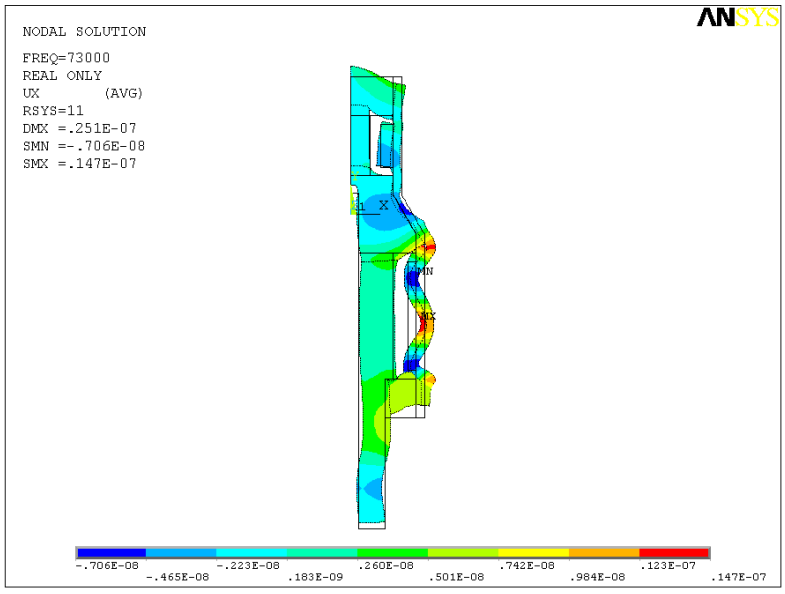

Figure 3.14: Initial and deformed shapes of the axisymmetric model of the transducer with the values of radial displacement when Tube2 is operated at its longitudinal mode (73 kHz)

The results including the resonance frequencies, bandwidths and electrical admittances of the tubes with frame in the circumferential expansion mode, found with FEM in ANSYS, are given in Table 3.5.

Table 3.5: Results of FEM in ANSYS about tubes with frame

	Resonance Frequency (kHz)	***-3 dB Bandwidth (kHz)***	***Fractional Bandwidth (%)***	***Electrical Admittance (mS)***
Tube1	60	17.59	29.0	0.23+j 0.81
Tube2	31	15.73	48.2	0.36+j 2.88

In Figure 3.15 and Figure 3.16, the conductances of the tubes with and without frame are compared.

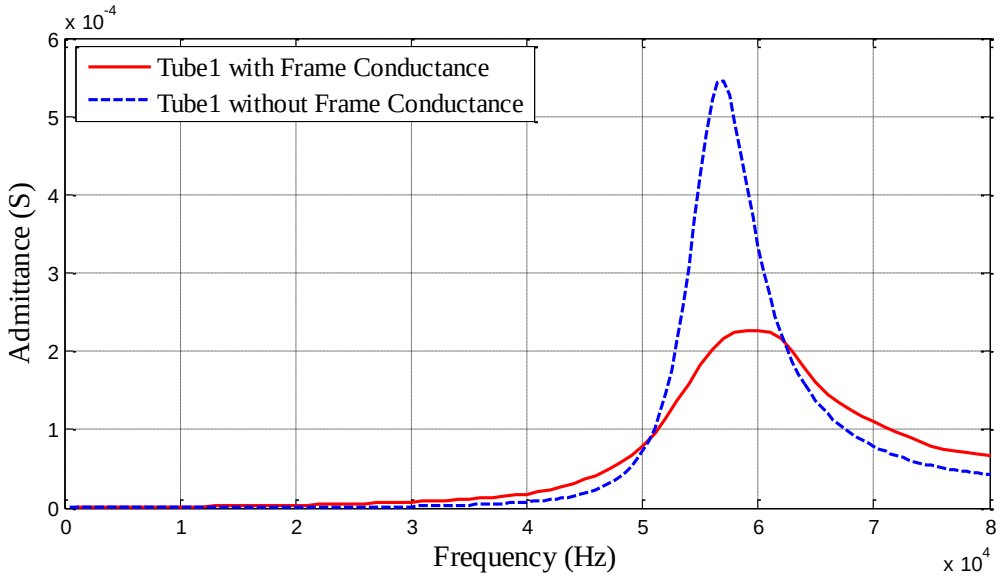

Figure 3.15: Comparison of the conductances of Tube1 with and without frame found with FEM in ANSYS

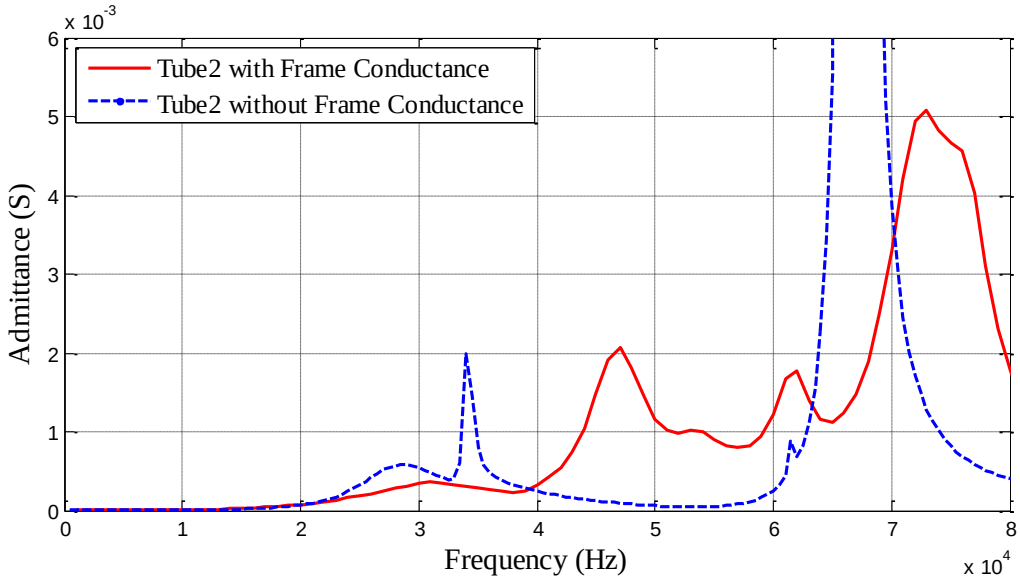

Figure 3.16: Comparison of the conductances of Tube2 with and without frame found with FEM in ANSYS

In the figures, it is seen that the center frequencies of the circumferential expansion modes go up by 2.5 kHz. Moreover, the conductance values at the center frequencies decrease by some amount and the bandwidths of these modes increase significantly. Above all, the bending mode of Tube2 centered at 34 kHz can be sent away from the operating frequency band to higher frequencies centered at 47 kHz. Therefore, the formation of undesired motions in the operating band of Tube2 can be prevented.

As a result, the numerical design of the transducer has been accomplished according to the acoustic requirements. The transducer operates at two wide frequency bands centered at about 30 and 60 kHz. Now, it must be checked in terms of mechanical and thermal performances.

3.1.2 Mechanical Performance

The second step in the numerical design of the transducer is the analysis of mechanical performance. Acoustic transducers are exposed to some loads due to their operational conditions. In this step, whether the transducer can be able to resist to these loads is checked. For this study, two types of loading are assumed to be exerted on the transducer: *static loading* and *dynamic loading*. Firstly, the transducer is exposed to hydrostatic pressure since it operates under water. Secondly, a dynamic shock may occur on the transducer while throwing it into the water. In this study, the hydrostatic pressure is taken as *30 bars* while the dynamic shock is assumed to be *500g for 1 millisecond*. Due to these loads, stresses and strains occur on the transducer, which can cause failure. These stresses and strains are determined with FEM in ANSYS and they are compared with the strength values of the materials used for the components of the transducer. For PZT Tubes, *maximum principal stress theory*, which is appropriate for brittle materials such as ceramics, is used as failure criterion whereas *Tsai-Wu failure theory* is utilized for composite components such as CRP Caps, CRP Rods and GRP Coating. In the following section, the mechanical performance of the transducer under static loading is explained.

3.1.2.1 Static Loading

The static loading on the transducer is hydrostatic pressure of 30 bars, which means a water depth of 300 m. The transducer designed is simulated with FEM in ANSYS in order to determine the stresses and strains occurred on it. The details about this simulation are given in Appendix F. The results of the simulation are evaluated individually for each component of the transducer. Firstly, the mechanical performances of PZT Tubes are checked. The principal stresses occurred on PZT ceramic tubes are shown in the figures from Figure 3.17 to Figure 3.19.

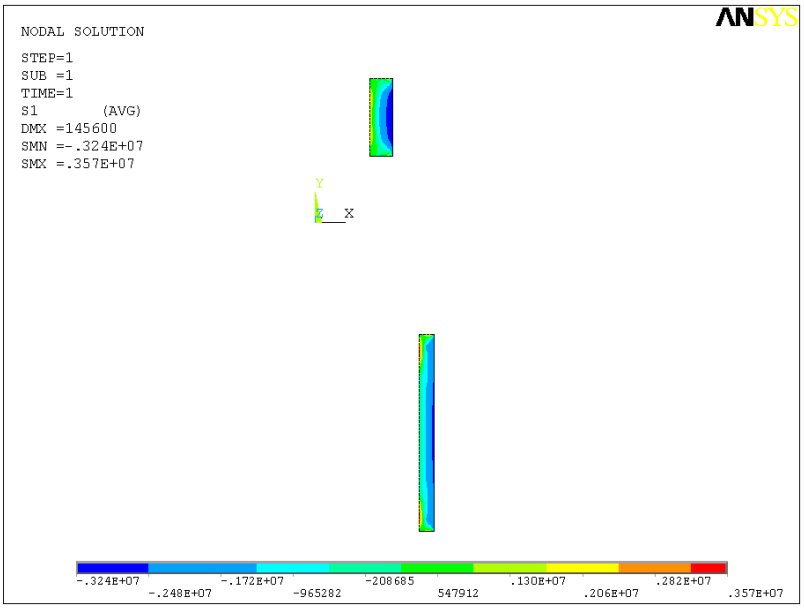

Figure 3.17: First principal stress values occurred on PZT Tubes

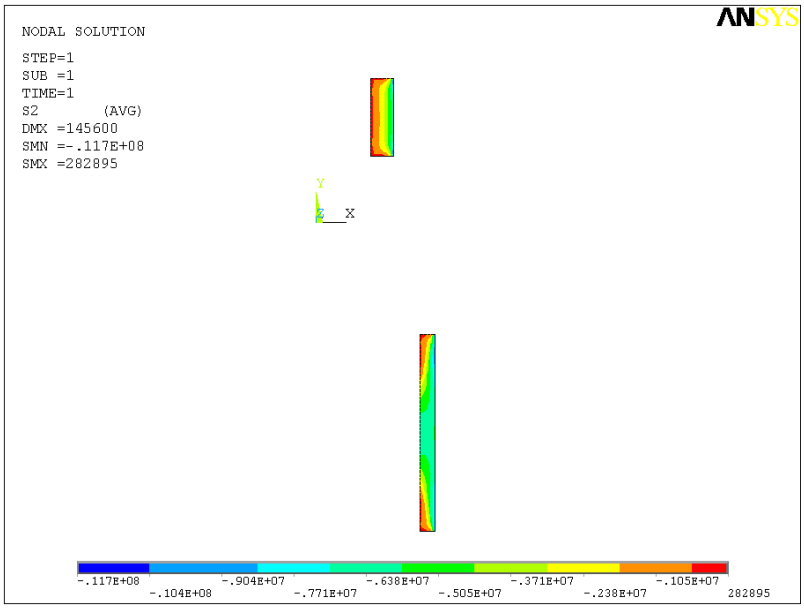

Figure 3.18: Second principal stress values occurred on PZT Tubes

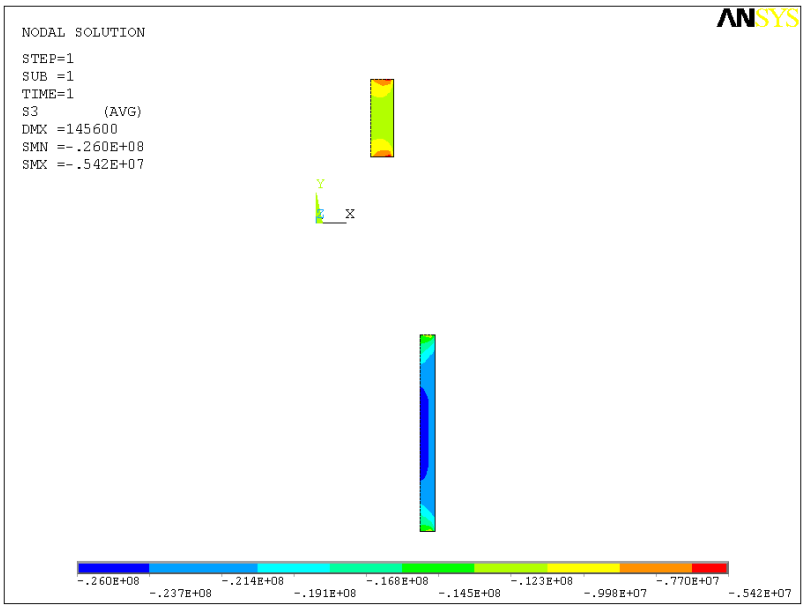

Figure 3.19: Third principal stress values occurred on PZT Tubes

Moreover, the maximum compressive and tensile principal stress values are tabulated in Table 3.6. According to the maximum principle stress theory, if one of the three principal stresses equals or exceeds the strength of the material, failure will occur [40].

Table 3.6: Maximum tensile and compressive principle stress values on PZT Tubes

	Principle Stress 1 (MPa)	***Principle Stress 2 (MPa)***	***Principle Stress 3 (MPa)***
Maximum Tensile	3.57	0.28	0
Maximum Compressive	-3.24	-11.71	**-25.96**

The strength value for PZT Tubes is the stress at which the piezoelectric properties begin to change significantly instead of yield strength or ultimate tensile strength. For PZT4 type of piezoelectric ceramic tubes, the maximum allowable static stress before a significant effect on performance is ***82.7 MPa*** along the polarization direction (radial in this study) and ***55 MPa*** along the other two directions perpendicular to the polarization (tangential and axial in this study) [6].

According to the results, the maximum principal stress occurred on the PZT Tubes is 25.96 MPa as compressive. The direction of this principle stress is tangential, which is perpendicular to the polarization direction. Therefore, it must be compared with 55 MPa and it is much lower than this strength limit. As a result, the mechanical performances of PZT Tubes under static loading are assumed to be adequate according to the maximum principal stress theory.

Secondly, the mechanical performances of CRP Caps are checked by using Tsai-Wu failure theory. CRP Caps have laminated structures so each lamina must be checked one by one and if one of them fails, the laminate will be assumed to fail in this study. Tsai-Wu failure theory indicates failure of a transversely isotropic lamina when the following inequality is satisfied [41]:

$$\begin{aligned} F_1\sigma_1 + F_2\left(\sigma_2+\sigma_3\right) + F_{11}{\sigma_1}^2 + F_{22}\left({\sigma_2}^2+{\sigma_3}^2\right) + 2\left(F_{22}-F_{23}\right){\tau_{23}}^2 \\ + F_{66}\left({\tau_{13}}^2+{\tau_{12}}^2\right) + 2F_{12}\left(\sigma_1\sigma_2+\sigma_1\sigma_3\right) + 2F_{23}\sigma_2\sigma_3 \geq 1 \end{aligned} \tag{3.1}$$

where

$$F_1 = \frac{1}{s_1^+} - \frac{1}{s_1^-} \quad , \quad F_2 = \frac{1}{s_2^+} - \frac{1}{s_2^-} \quad , \quad F_{11} = \frac{1}{s_1^+ s_1^-}$$

$$F_{22} = \frac{1}{s_2^+ s_2^-} \quad , \quad F_{66} = \frac{1}{s_{12}{}^2} \quad , \quad F_{12} = -\frac{1}{2}\sqrt{F_{11}F_{22}} \qquad (3.2)$$

$$F_{23} = -\frac{1}{2}F_{22}$$

s_1^+, s_1^- Tensile and compressive strengths in the fiber direction

s_2^+, s_2^- Tensile and compressive strengths perpendicular to the fibers

s_{12} Shear strengths (Table 3.7)

Table 3.7: Strength values of T300 carbon fibers [41]

Unit	s_1^+	s_1^-	s_2^+	s_2^-	s_{12}
MPa	1500	1500	40	246	68

The left-hand side of Equation (3.1) is designated as *failure index (F)* and it must be lower than unity for failure not to occur. On the other hand, *stress ratio (R)* is a factor by which each load and so each stress component is multiplied such that failure occurs. Therefore, it can be thought as the maximum safety factor that can be applied. When R is larger than unity, failure does not occur. The stress ratio (R) is defined as follows [41]:

$$R = \frac{-b + \sqrt{b^2 + 4a}}{2a} \qquad (3.3)$$

where

$$a = F_{11}\sigma_1^{\,2} + F_{22}\left(\sigma_2^{\,2} + \sigma_3^{\,2}\right) + 2\left(F_{22} - F_{23}\right)\tau_{23}^{\,2} + F_{66}\left(\tau_{13}^{\,2} + \tau_{12}^{\,2}\right) + 2F_{12}\left(\sigma_1\sigma_2 + \sigma_1\sigma_3\right) + 2F_{23}\sigma_2\sigma_3 \quad (3.4a)$$

$$b = F_1\sigma_1 + F_2\left(\sigma_2 + \sigma_3\right) \quad (3.4b)$$

By axisymmetric modeling with FEM, stress components in cylindrical coordinates, which are shown in the figures from Figure 3.20 to Figure 3.23, can be found.

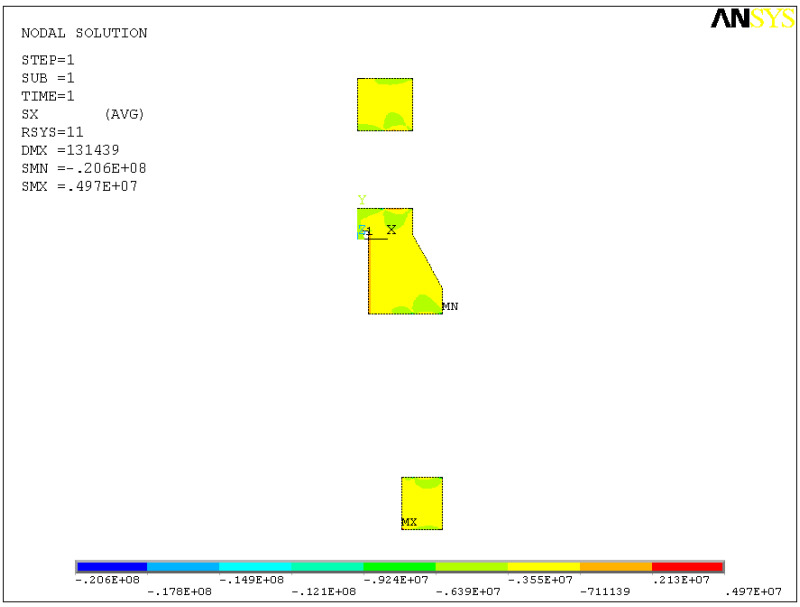

Figure 3.20: Radial normal stress (σ_r) values occurred on CRP Caps

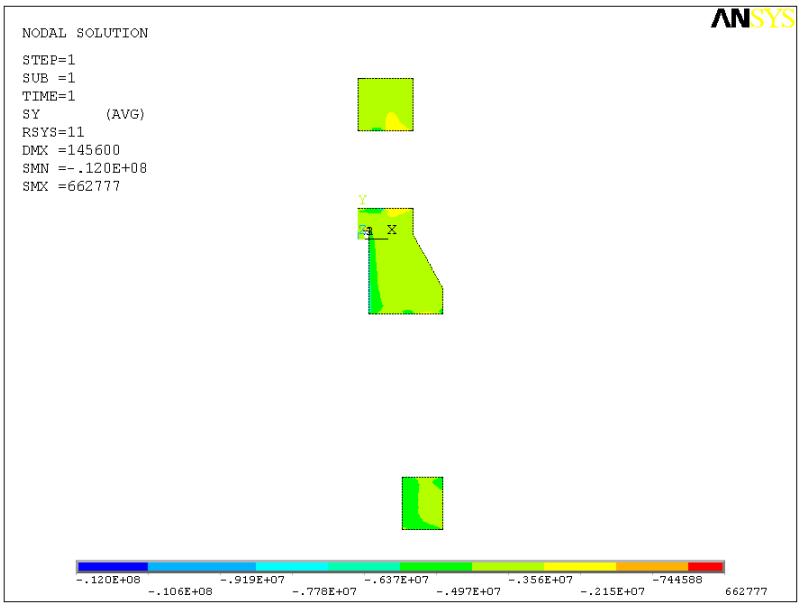

Figure 3.21: Tangential normal stress (σ_θ) values occurred on CRP Caps

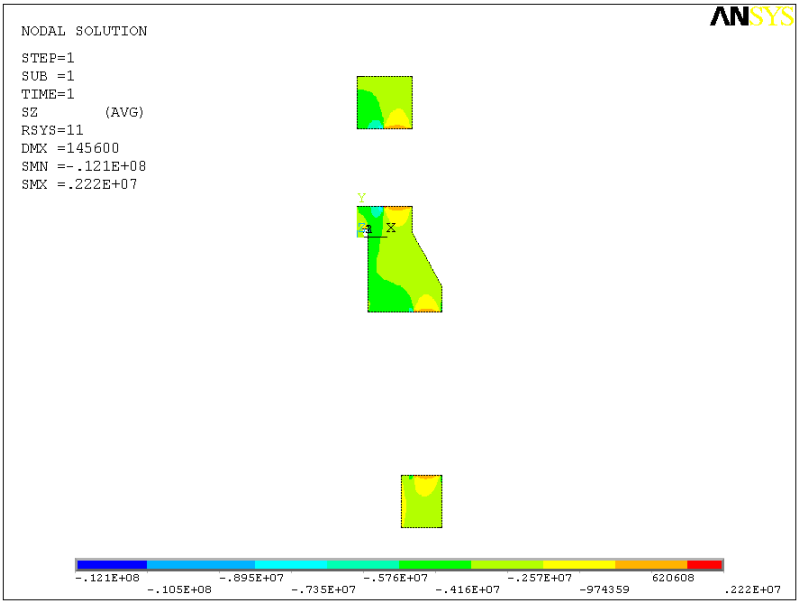

Figure 3.22: Axial normal stress (σ_z) values occurred on CRP Caps

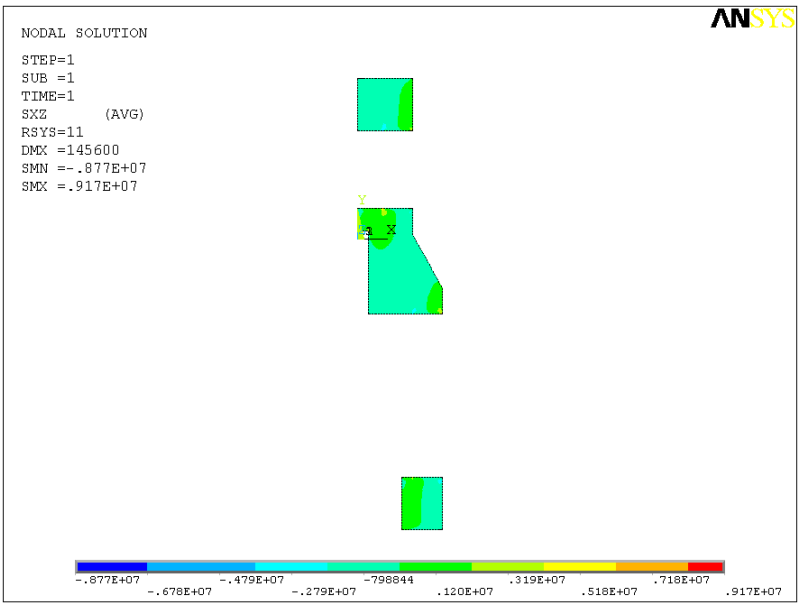

Figure 3.23: Shear stress (τ_{rz}) values occurred on CRP Caps

Due to the axisymmetry, stress components in cylindrical coordinates are symmetric with respect to the symmetry axis. In other words, all points on any circle lying on r-θ plane with the center on symmetry axis possess the same cylindrical stress components as illustrated in Figure 3.24.

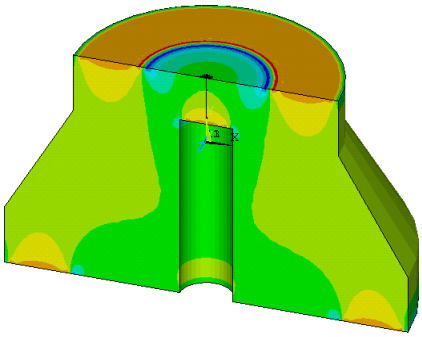

Figure 3.24: Symmetry of stress components in cylindrical coordinates with respect to the symmetry axis (e.g., axial stress (σ_z))

Furthermore, $\tau_{r\theta}$ and $\tau_{\theta z}$ are zero in axisymmetric structures since u_θ, $\frac{\partial u_r}{\partial \theta}$, $\frac{\partial u_z}{\partial \theta}$ are zero as symmetry conditions. Therefore, there are 4 nonzero stress components in this model, namely, σ_r, σ_θ, σ_z and τ_{rz}. As a result, the axisymmetric analysis gives the stress components in cylindrical coordinates at everywhere on 3D structure.

However, for the failure analysis of CRP Caps, the stress components in principal material directions of each lamina, which are illustrated in Figure 3.25, are required. Therefore, coordinate transformation from cylindrical coordinates to principal material directions must be performed:

$$\begin{Bmatrix} \sigma_1 \\ \sigma_2 \\ \sigma_3 \\ \tau_{23} \\ \tau_{13} \\ \tau_{12} \end{Bmatrix} = [T_\sigma] \begin{Bmatrix} \sigma_r \\ \sigma_\theta \\ \sigma_z \\ \tau_{\theta z} \\ \tau_{rz} \\ \tau_{r\theta} \end{Bmatrix} \tag{3.5}$$

where $[T_\sigma]$ is the transformation matrix about the axial direction (z) and it is equal to the transformation matrix given in Eq. (E.14).

In this study, the laminas are not modeled individually. Instead, the total laminate is divided into sublaminates, each of which is composed of 8 laminas ($[0/45/90/-45]_S$), and each sublaminate is represented by one element in thickness direction. Thus, the stress components that occur on each lamina in a sublaminate are not known. Instead, the analysis gives the stresses on each element and so on each sublaminate. Therefore, the stresses on any sublaminate are assumed to occur on all laminas in that sublaminate equally. In other words,

it is assumed that all of the eight laminas in any sublaminate have the same stresses in cylindrical coordinates as shown in the figures. Consequently, the stresses in cylindrical coordinates at all points on a sublaminate must be transformed to the principal material directions of all laminas in that sublaminate one by one.

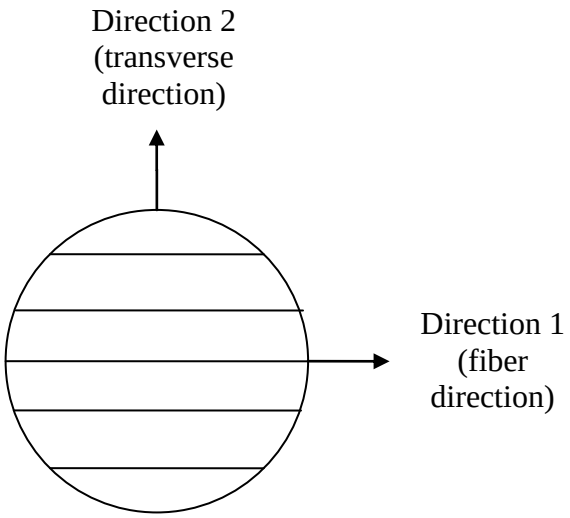

Figure 3.25: Top view of the lamina with 0° orientation angle in CRP Caps (direction 3 is orthogonal to direction 1 and direction 2)

From the stresses in principal material directions of laminas, the failure index (F) and stress ratio (R) at all points on each lamina can be calculated. Since all laminas in a sublaminate have the same stresses in cylindrical coordinates, these failure indicators are found same at points oriented with same angle with respect to principal material directions. The most critical F (maximum) and R (minimum) are found as ***0.1187*** and ***6.4942*** on each lamina in the lowest sublaminate of the bottom cap, respectively. Their locations on each lamina are the points where the radial stress with the value of ***4.97 MPa*** (MX in Figure 3.20) is coincident with the principal material direction 2, as shown in the figures from Figure 3.26 to Figure 3.29. It is evident that the locations of the

critical points rotate as the same angle as the rotation of the fibers. The stress components in cylindrical coordinates and in principal material directions for the most critical points are tabulated in Table 3.8.

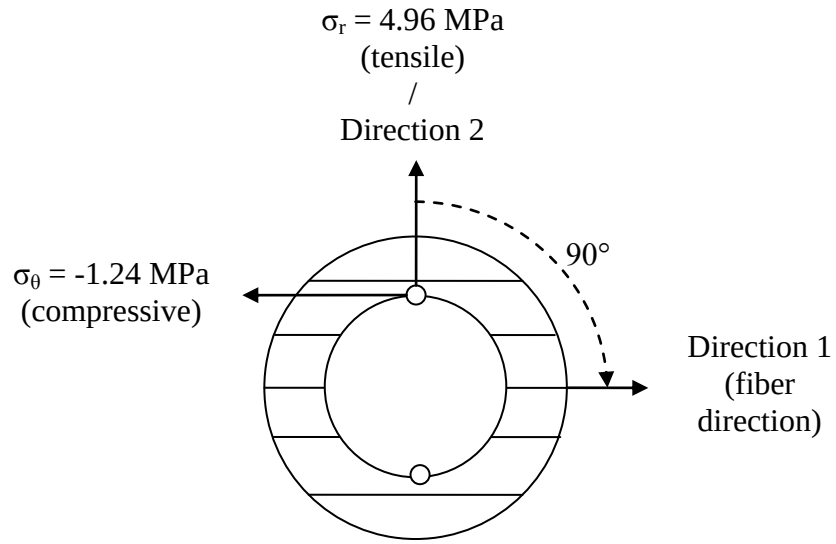

Figure 3.26: Most critical points for the laminas with 0° orientation angle in the lowest sublaminate of the bottom CRP Cap

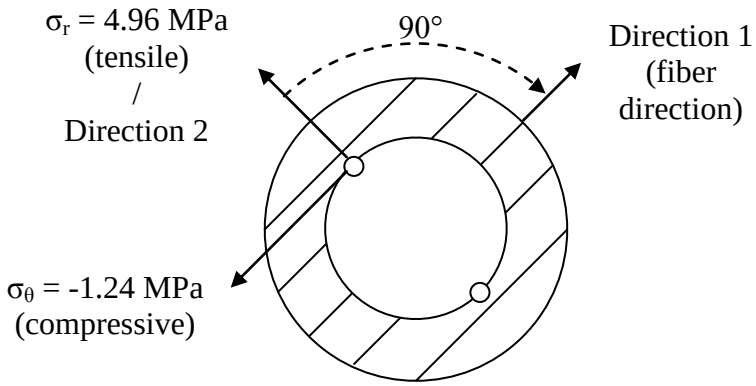

Figure 3.27: Most critical points for the laminas with 45° orientation angle in the lowest sublaminate of the bottom CRP Cap

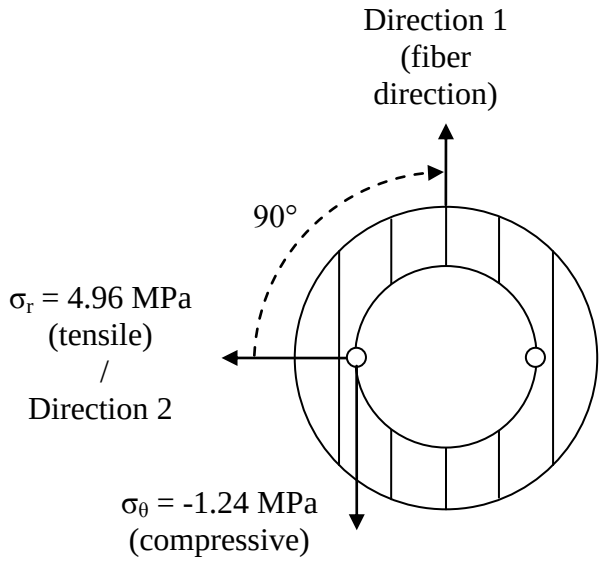

Figure 3.28: Most critical points for the laminas with 90° orientation angle in the lowest sublaminate of the bottom CRP Cap

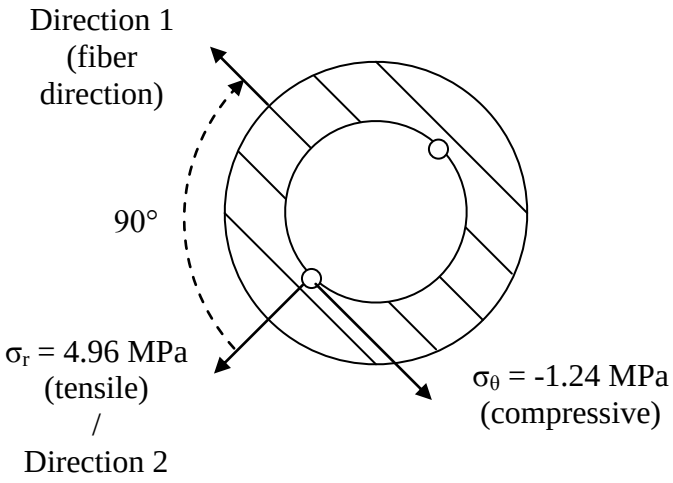

Figure 3.29: Most critical points for the laminas with -45° orientation angle in the lowest sublaminate of the bottom CRP Cap

Table 3.8: Stress components in cylindrical coordinates and in principal material directions for the most critical points of CRP Caps

CYLINDRICAL COORDINATES						
Unit	σ_r	σ_θ	σ_z	$\tau_{\theta z}$	τ_{zr}	$\tau_{r\theta}$
MPa	4.96	-1.24	0.40	0	3.65	0
PRINCIPAL MATERIAL DIRECTIONS						
Unit	σ_1	σ_2	σ_3	τ_{23}	τ_{31}	τ_{12}
MPa	-1.24	4.96	0.40	3.65	0	0

Since failure index (F) is lower than 1, no problem is expected about the mechanical performances of CRP Caps according to Tsai-Wu failure theory. However, it should be remembered that all of the eight laminas in any sublaminate are assumed to have the same stresses and the analysis is a 2D axisymmetric analysis. On the other hand, the stress ratio (R) gives the failure hydrostatic pressure as ***194.83 bars*** so a safety factor of up to ***6.4942*** can be taken for CRP Caps.

Thirdly, the mechanical performance of GRP Coating is checked similarly by using Tsai-Wu failure theory. Since GRP Coating is composed of plies formed from woven fabrics, Tsai-Wu failure theory becomes as follows [41]:

$$\begin{aligned} &F_1\sigma_1 + F_2\sigma_2 + F_3\sigma_3 + F_{11}{\sigma_1}^2 + F_{22}{\sigma_2}^2 + F_{33}{\sigma_3}^2 + F_{44}{\tau_{23}}^2 \\ &\quad + F_{55}{\tau_{13}}^2 + F_{66}{\tau_{12}}^2 + 2\left(F_{12}\sigma_1\sigma_2 + F_{13}\sigma_1\sigma_3 + F_{23}\sigma_2\sigma_3\right) \geq 1 \end{aligned} \tag{3.6}$$

where

$$F_1 = \frac{1}{s_1^+} - \frac{1}{s_1^-} \quad , \quad F_2 = \frac{1}{s_2^+} - \frac{1}{s_2^-} \quad , \quad F_3 = \frac{1}{s_3^+} - \frac{1}{s_3^-}$$

$$F_{11} = \frac{1}{s_1^+ s_1^-} \quad , \quad F_{22} = \frac{1}{s_2^+ s_2^-} \quad , \quad F_{33} = \frac{1}{s_3^+ s_3^-} \tag{3.7}$$

$$F_{44} = \frac{1}{s_{23}^{\ 2}} \quad , \quad F_{55} = \frac{1}{s_{13}^{\ 2}} \quad , \quad F_{66} = \frac{1}{s_{12}^{\ 2}}$$

$$F_{12} = -\frac{1}{2}\sqrt{F_{11}F_{22}} \quad , \quad F_{23} = -\frac{1}{2}\sqrt{F_{22}F_{33}} \quad , \quad F_{13} = -\frac{1}{2}\sqrt{F_{11}F_{33}}$$

$s_1^+,\ s_1^-$ Tensile and compressive strengths in the fiber direction

$s_2^+,\ s_2^-$ Tensile and compressive strengths perpendicular to the fibers

$s_3^+,\ s_3^-$ Tensile and compressive strengths in the out-of-plane direction

$s_{12},\ s_{23},\ s_{13}$ Shear strengths (Table 3.9)

Table 3.9: Strength values of E-glass woven fabrics [41]

Unit	s_1^+	s_1^-	s_2^+	s_2^-	s_3^+	s_3^-	s_{12}	s_{23}	s_{13}
MPa	367	549	367	549	31	118	97	72	72

Moreover, the stress ratio (R) is defined as follows for woven fabrics [41]:

$$R = \frac{-b + \sqrt{b^2 + 4a}}{2a} \tag{3.8}$$

where

$$\begin{aligned} a = {} & F_{11}\sigma_1^{\ 2} + F_{22}\sigma_2^{\ 2} + F_{33}\sigma_3^{\ 2} + F_{44}\tau_{23}^{\ 2} + F_{55}\tau_{13}^{\ 2} \\ & + F_{66}\tau_{12}^{\ 2} + 2\left(F_{12}\sigma_1\sigma_2 + F_{13}\sigma_1\sigma_3 + F_{23}\sigma_2\sigma_3\right) \end{aligned} \tag{3.9a}$$

$$b = F_1\sigma_1 + F_2\sigma_2 + F_3\sigma_3 \tag{3.9b}$$

The stresses in cylindrical coordinates on GRP Coating are shown in the figures from Figure 3.30 to Figure 3.33.

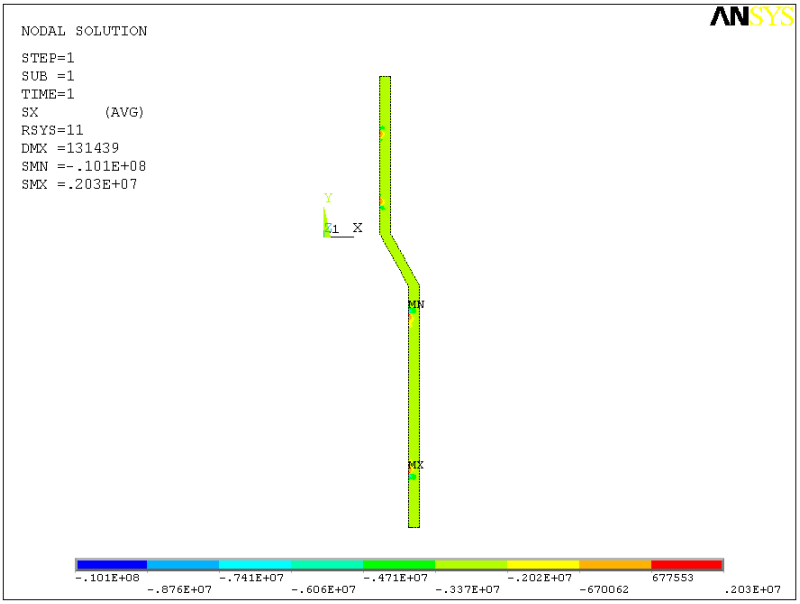

Figure 3.30: Radial normal stress (σ_r) values occurred on GRP Coating

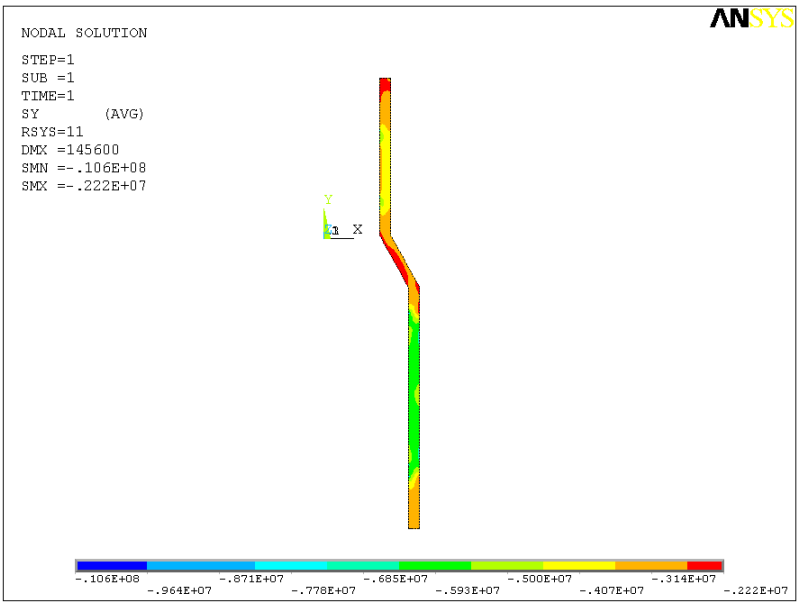

Figure 3.31: Tangential normal stress (σ_θ) values occurred on GRP Coating

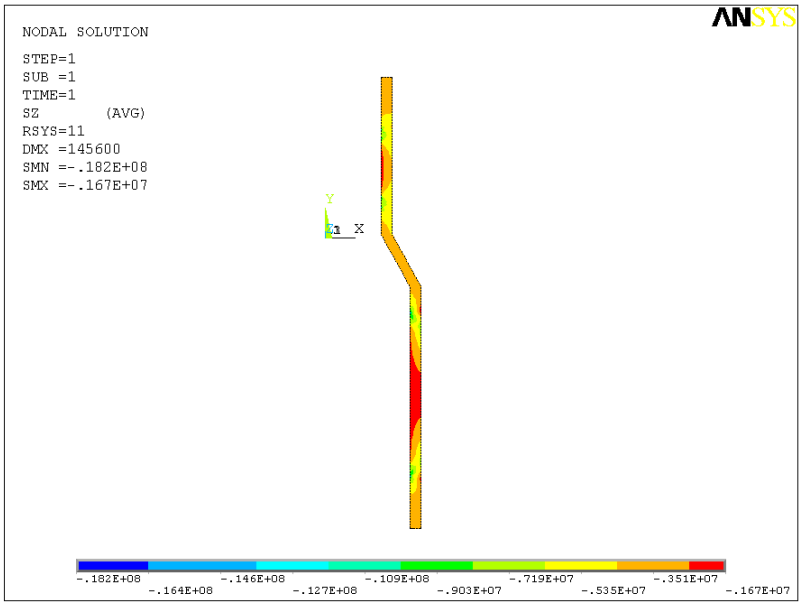

Figure 3.32: Axial normal stress (σ_z) values occurred on GRP Coating

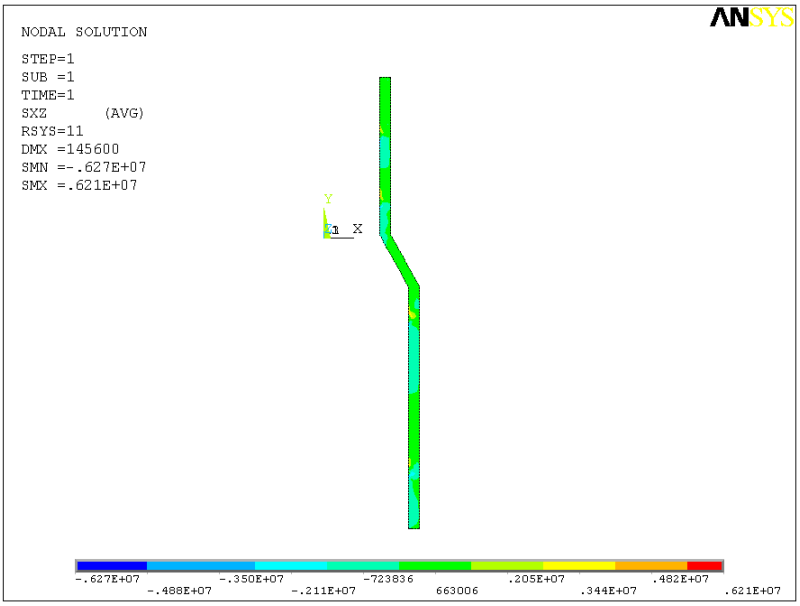

Figure 3.33: Shear stress (τ_{rz}) values occurred on GRP Coating

Since the principle material directions of the coating have different orientations from the cylindrical coordinates as shown in Figure 3.34, coordinate transformation is again required.

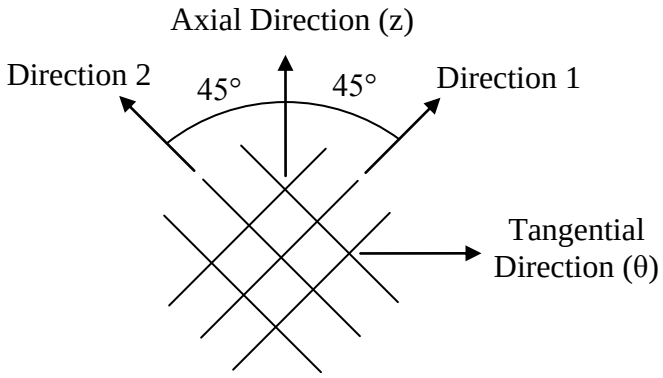

Figure 3.34: Front view of the fibers in GRP Coating, the principle material directions and cylindrical coordinates

Firstly, the cylindrical coordinates must be rotated with an angle of 135° counterclockwise about radial direction (Figure 3.35) and then the second rotation with 90° counterclockwise about new tangential direction (θ') must be performed (Figure 3.36). The transformation matrices for the rotations about radial and tangential directions are given in Eqs. (3.10) and (3.11), respectively [41].

$$\left[T_{\sigma}^{r}\right]=\begin{bmatrix} 1 & 0 & 0 & 0 & 0 & 0 \\ 0 & c^2 & s^2 & 2cs & 0 & 0 \\ 0 & s^2 & c^2 & -2cs & 0 & 0 \\ 0 & -cs & cs & c^2-s^2 & 0 & 0 \\ 0 & 0 & 0 & 0 & c & -s \\ 0 & 0 & 0 & 0 & s & c \end{bmatrix} \qquad \begin{matrix} c=\cos(\theta_r) \\ s=\sin(\theta_r) \end{matrix} \qquad (3.10)$$

$$\left[T_{\sigma}^{\theta}\right]=\begin{bmatrix} c^2 & 0 & s^2 & 0 & 2cs & 0 \\ 0 & 1 & 0 & 0 & 0 & 0 \\ s^2 & 0 & c^2 & 0 & -2cs & 0 \\ 0 & 0 & 0 & c & 0 & -s \\ -cs & 0 & cs & 0 & c^2-s^2 & 0 \\ 0 & 0 & 0 & s & 0 & c \end{bmatrix} \qquad \begin{matrix} c=\cos(\theta_\theta) \\ s=\sin(\theta_\theta) \end{matrix} \qquad (3.11)$$

The total transformation matrix is the product of these two matrices as follows:

$$\left[T_{\sigma}\right]=\left[T_{\sigma}^{\theta}\right]\left[T_{\sigma}^{r}\right] \qquad (3.12)$$

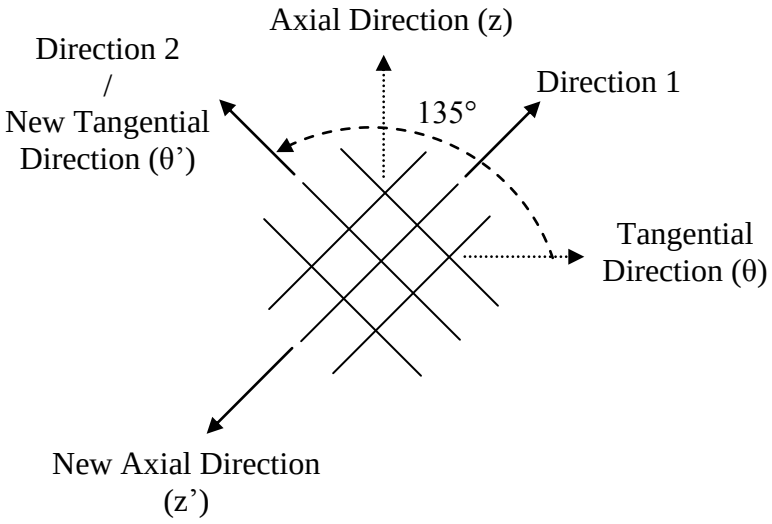

Figure 3.35: First step in coordinate transformation of GRP Coating; rotation with an angle of 135° counterclockwise about radial direction

Then, the stress components in principal material directions can be found by using Eq. (3.5). As a result, the most critical F (maximum) and R (minimum) are calculated as ***0.0371*** and ***13.0941***, respectively. Their locations are all points on a circle formed by 360° rotation of the point with the radial stress of ***2.03 MPa***

tensile (MX in Figure 3.30) about the symmetry axis. The stress components in cylindrical coordinates and in principal material directions for the most critical points are tabulated in Table 3.10.

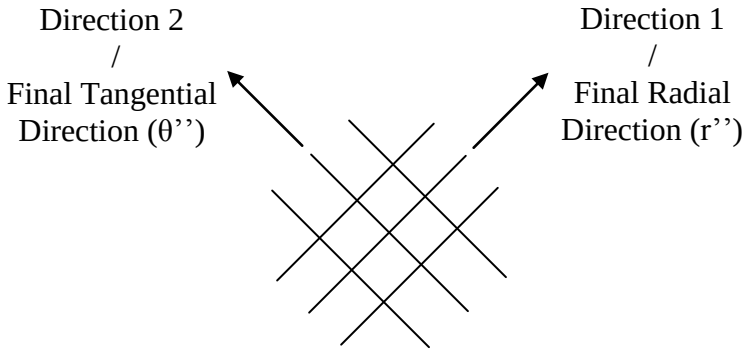

Figure 3.36: Second step in coordinate transformation of GRP Coating; rotation with an angle of 90° counterclockwise about new tangential direction

Table 3.10: Stress components in cylindrical coordinates and in principal material directions for the most critical points of GRP Coating

CYLINDRICAL COORDINATES						
Unit	σ_r	σ_θ	σ_z	$\tau_{\theta z}$	τ_{zr}	$\tau_{r\theta}$
MPa	2.03	-6.06	-9.90	0	1.09	0
PRINCIPAL MATERIAL DIRECTIONS						
Unit	σ_1	σ_2	σ_3	τ_{23}	τ_{31}	τ_{12}
MPa	-7.98	-7.98	2.03	-0.77	0.77	1.92

Since failure index (F) is lower than 1, no problem is expected about the mechanical performances of GRP Coating according to Tsai-Wu failure theory.

On the other hand, the stress ratio (R) gives the failure hydrostatic pressure as ***392.82 bars*** so a safety factor of up to ***13.0941*** can be taken for GRP Coating.

Finally, the mechanical performances of CRP Rods are checked by using Tsai-Wu failure theory. Since CRP Rods are composed of unidirectional carbon fibers, they are transversely isotropic materials. Therefore, Tsai-Wu failure theory and stress ratio (R) are the same with the given for CRP Caps in Eq. (3.1) and Eq. (3.3), respectively. Moreover, the strength values of T300 carbon fibers were given in Table 3.7. The stresses in cylindrical coordinates on CRP Rods are shown in the figures from Figure 3.37 to Figure 3.40.

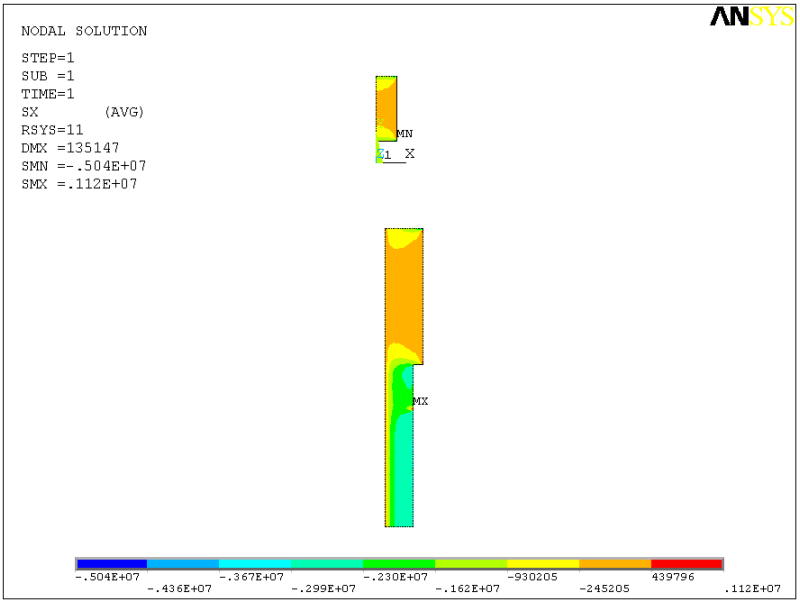

Figure 3.37: Radial normal stress (σ_r) values occurred on CRP Rods

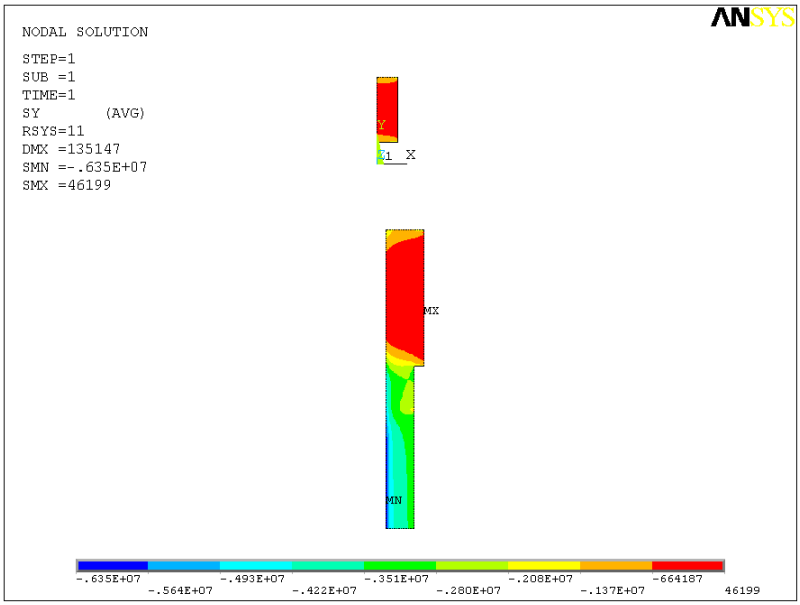

Figure 3.38: Tangential normal stress (σ_θ) values occurred on CRP Rods

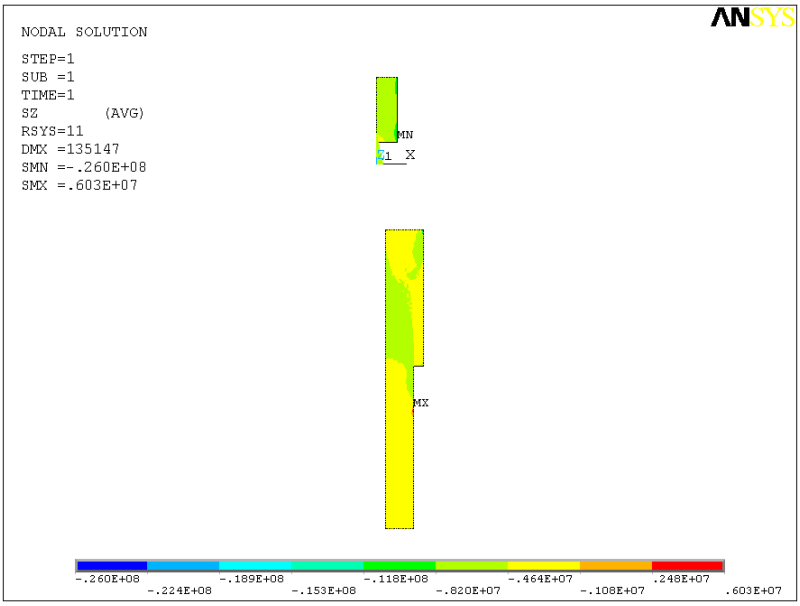

Figure 3.39: Axial normal stress (σ_z) values occurred on CRP Rods

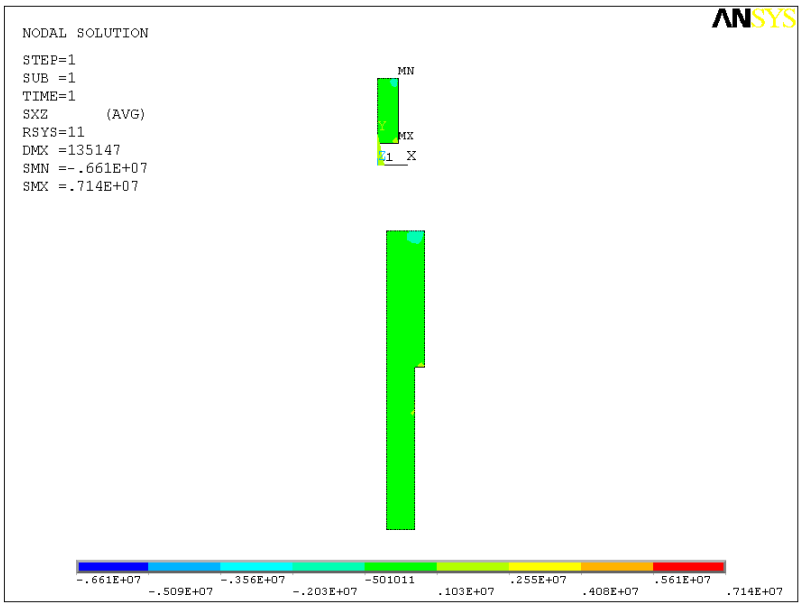

Figure 3.40: Shear stress (τ_{rz}) values occurred on CRP Rods

The principle material directions of CRP Rods and cylindrical coordinates are shown in Figure 3.41.

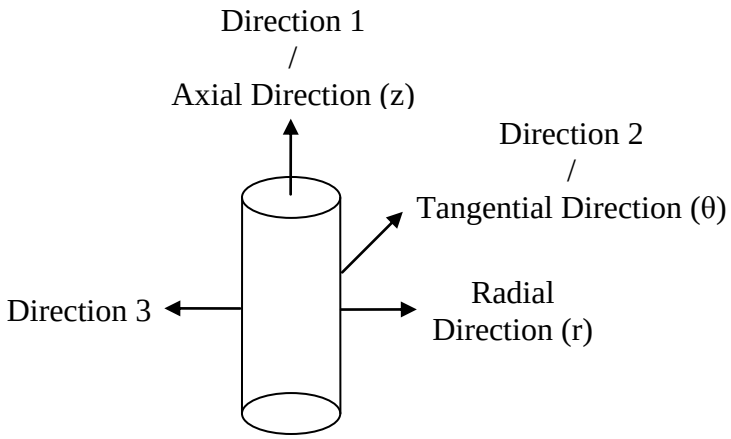

Figure 3.41: Front view of the CRP Rod, the principle material directions and cylindrical coordinates

As seen in the figure, a coordinate transformation is again required; the cylindrical coordinates must be rotated with an angle of 90° clockwise about tangential direction. Therefore, the transformation matrix given in Eq. (3.11) is inserted in Eq. (3.5) in order to find the stress components in principal material directions.

Eventually, the most critical F (maximum) and R (minimum) are calculated as ***-0.1807*** and ***20.2701***, respectively. Their locations are all points on a circle formed by 360° rotation of the point with the radial stress of ***5.04 MPa compressive*** (MN in Figure 3.37) about the symmetry axis. The stress components in cylindrical coordinates and in principal material directions for the most critical points are tabulated in Table 3.11.

Table 3.11: Stress components in cylindrical coordinates and in principal material directions for the most critical points of CRP Rods

CYLINDRICAL COORDINATES						
Unit	σ_r	σ_θ	σ_z	$\tau_{\theta z}$	τ_{zr}	$\tau_{r\theta}$
MPa	-5.04	-4.16	-26.02	0	7.14	0
PRINCIPAL MATERIAL DIRECTIONS						
Unit	σ_1	σ_2	σ_3	τ_{23}	τ_{31}	τ_{12}
MPa	-26.02	-4.16	-5.04	0	-7.14	0

Since failure index (F) is lower than 1, no problem is expected about the mechanical performances of CRP Rods according to Tsai-Wu failure theory. On

the other hand, the stress ratio (R) gives the failure hydrostatic pressure as ***608.10 bars*** so a safety factor of up to ***20.2701*** can be taken for CRP Rods.

In conclusion, the transducer designed can be able to resist to the static loading of 30 bars. In the following section, the mechanical performance of the transducer under dynamic loading is explained.

3.1.2.2 Dynamic Loading

The dynamic loading on the transducer is a shock of 500g for 1 millisecond, which is applied on the bottom of the transducer. The transducer is again simulated with FEM in ANSYS in order to determine the stresses and strains occurred on it. The details about this simulation are given in Appendix G. As explained there, the transient simulation is performed up to 2 milliseconds for transiency to finish. Similarly, the results are evaluated individually for each component of the transducer.

Firstly, the mechanical performances of PZT Tubes are checked. The maximum principle stress values take place at the beginning of the loading, i.e., at 0.06. ms. They are shown in the figures from Figure 3.42 to Figure 3.44.

Moreover, the maximum compressive and tensile principal stress values at this time are tabulated in Table 3.12. The strength value is again taken as the stress at which the piezoelectric properties begin to change significantly. For PZT4, the maximum allowable dynamic stress before a significant effect on performance is ***24 MPa*** along all directions [6].

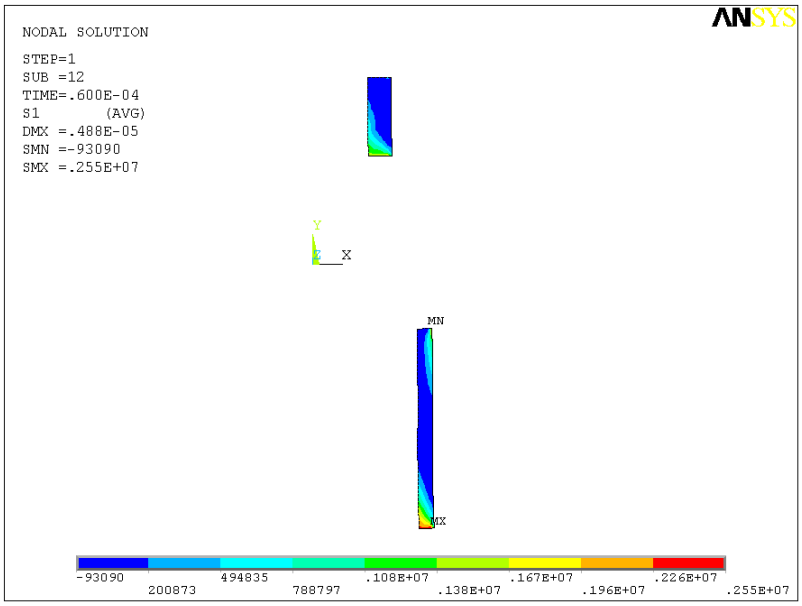

Figure 3.42: First principal stress values occurred on PZT Tubes at 0.06. ms.

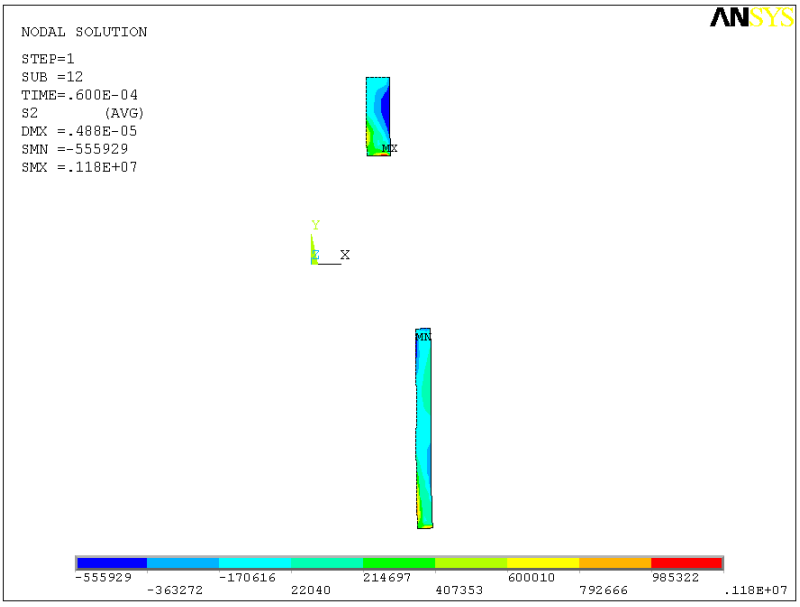

Figure 3.43: Second principal stress values occurred on PZT Tubes at 0.06. ms.

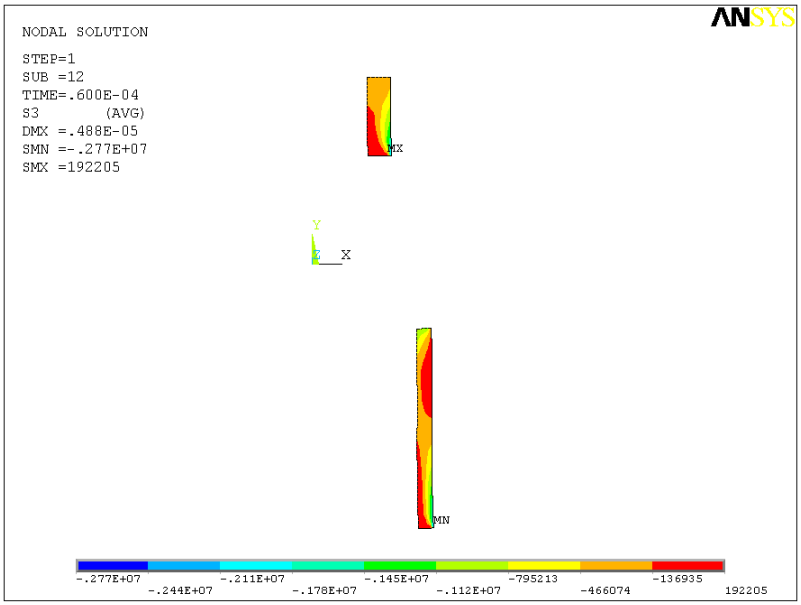

Figure 3.44: Third principal stress values occurred on PZT Tubes at 0.06. ms.

Table 3.12: Maximum tensile and compressive principle stress values on PZT Tubes at 0.06. ms.

	Principle Stress 1 (MPa)	**Principle Stress 2 (MPa)**	**Principle Stress 3 (MPa)**
Maximum Tensile	2.55	1.18	0.19
Maximum Compressive	-0.09	-0.56	**-2.77**

According to the results, the maximum principal stress occurred on the PZT Tubes is 2.77 MPa as compressive. Since this value is much lower than the strength value of 24 MPa, the mechanical performances of PZT Tubes under dynamic loading are assumed to be adequate according to the principle stress theory.

Secondly, the mechanical performances of CRP Caps under dynamic loading are evaluated in the same way with the static loading. The maximum stress components in cylindrical coordinates occur at 0.06. ms. They are shown in the figures from Figure 3.45 to Figure 3.48.

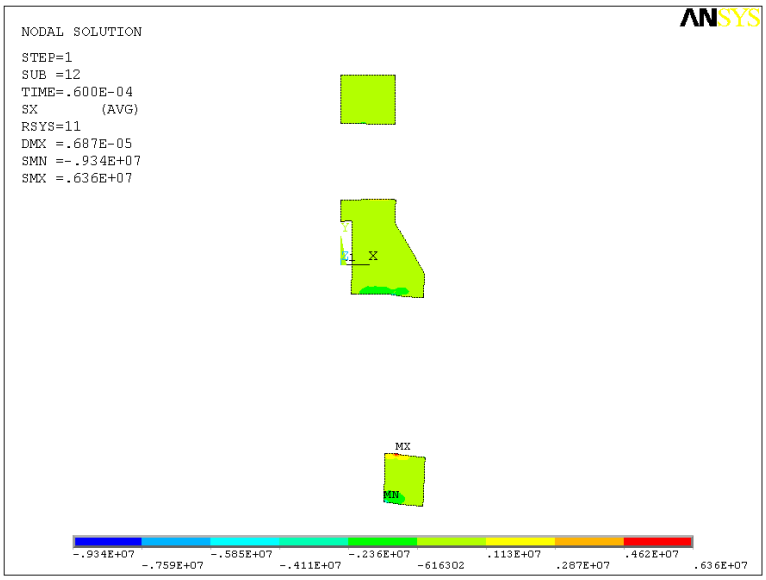

Figure 3.45: Radial normal stress (σ_r) values on CRP Caps at 0.06. ms.

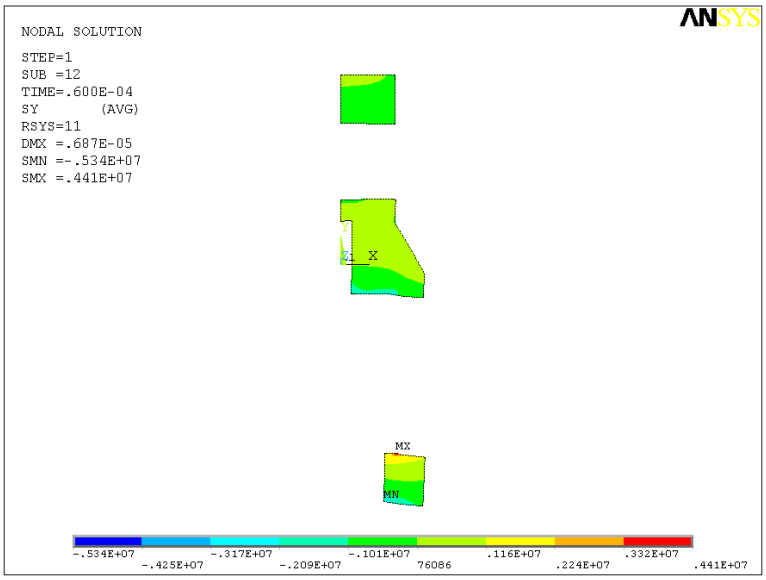

Figure 3.46: Tangential normal stress (σ_θ) values on CRP Caps at 0.06. ms.

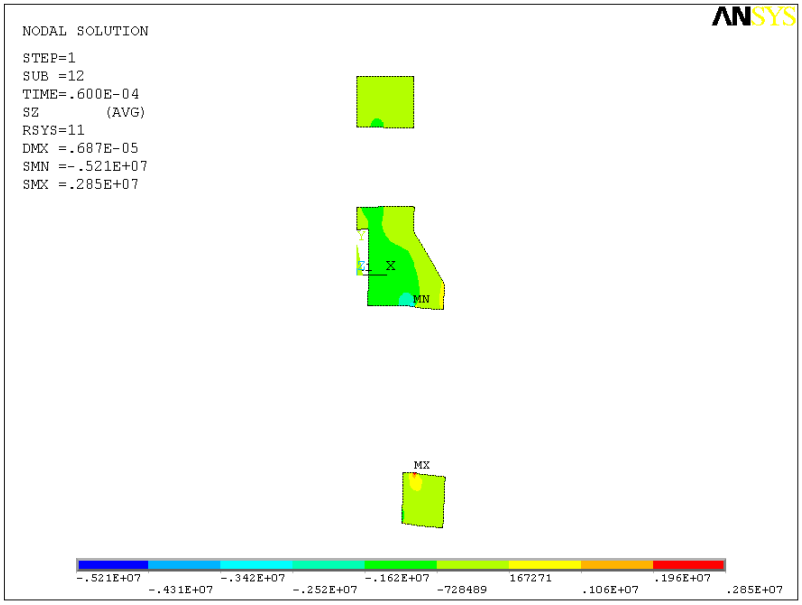

Figure 3.47: Axial normal stress (σ_z) values on CRP Caps at 0.06. ms.

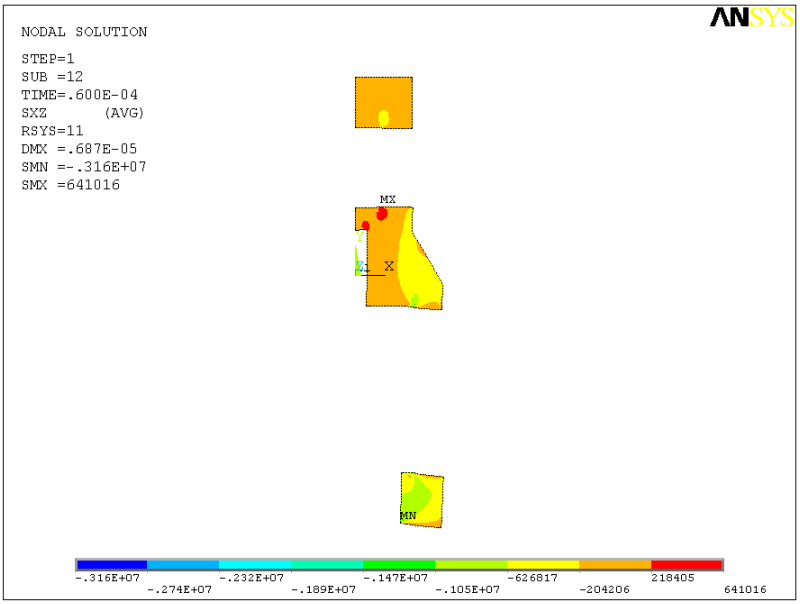

Figure 3.48: Shear stress (τ_{rz}) values on CRP Caps at 0.06. ms.

The failure index (F) and stress ratio (R) can be calculated by using Eqs. (3.1), (3.2), (3.3) and (3.4) with Table 3.7 after finding stress components in principal material directions by stress transformation with Eq. (3.5) and (E.14). The most critical F (maximum) and R (minimum) are found as ***0.1963*** and ***4.7843*** on each lamina in the uppermost sublaminate of the bottom cap, respectively. Their locations on each lamina are the points where the radial stress with the value of ***6.36 MPa*** (MX in Figure 3.45) is coincident with the principal material direction 2, in a similar way with the ones shown in figures from Figure 3.26 to Figure 3.29. The stress components in cylindrical coordinates and in principal material directions for the most critical points are tabulated in Table 3.13.

Table 3.13: Stress components in cylindrical coordinates and in principal material directions for the most critical points of CRP Caps at 0.06. ms.

CYLINDRICAL COORDINATES						
Unit	σ_r	σ_θ	σ_z	$\tau_{\theta z}$	τ_{zr}	$\tau_{r\theta}$
MPa	6.36	4.41	2.85	0	-1.31	0
PRINCIPAL MATERIAL DIRECTIONS						
Unit	σ_1	σ_2	σ_3	τ_{23}	τ_{31}	τ_{12}
MPa	4.41	6.36	2.85	-1.31	0	0

Since failure index (F) is lower than 1, no problem is expected about the mechanical performance of CRP Caps under dynamic loading according to Tsai-Wu failure theory. On the other hand, the stress ratio (R) gives the dynamic loading at failure as ***2392.15g*** so a safety factor of up to ***4.7843*** can be taken for CRP Caps.

Thirdly, the mechanical performance of GRP Coating under dynamic loading is checked. This task is again the same with the static loading. Similarly, the

maximum stress components in cylindrical coordinates occur at 0.06. ms. They are shown in the figures from Figure 3.49 to Figure 3.52.

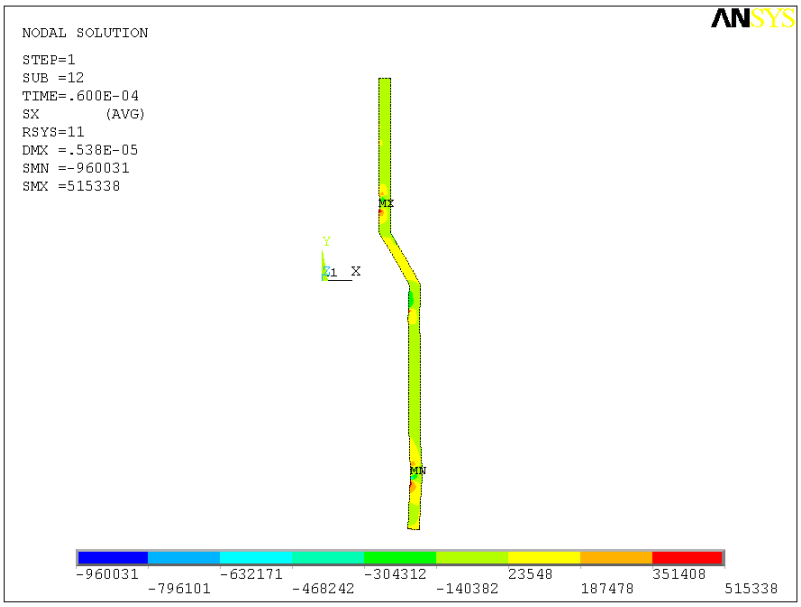

Figure 3.49: Radial normal stress (σ_r) values on GRP Coating at 0.06. ms.

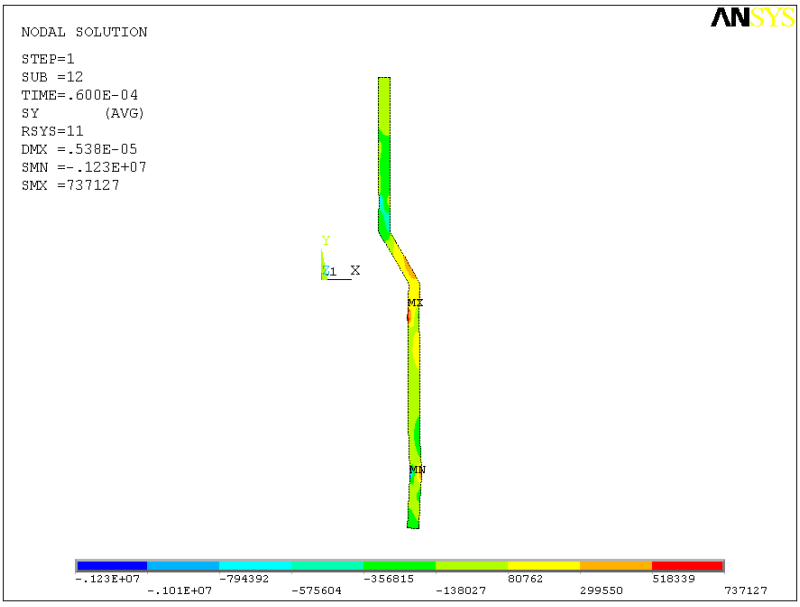

Figure 3.50: Tangential normal stress (σ_θ) values on GRP Coating at 0.06. ms.

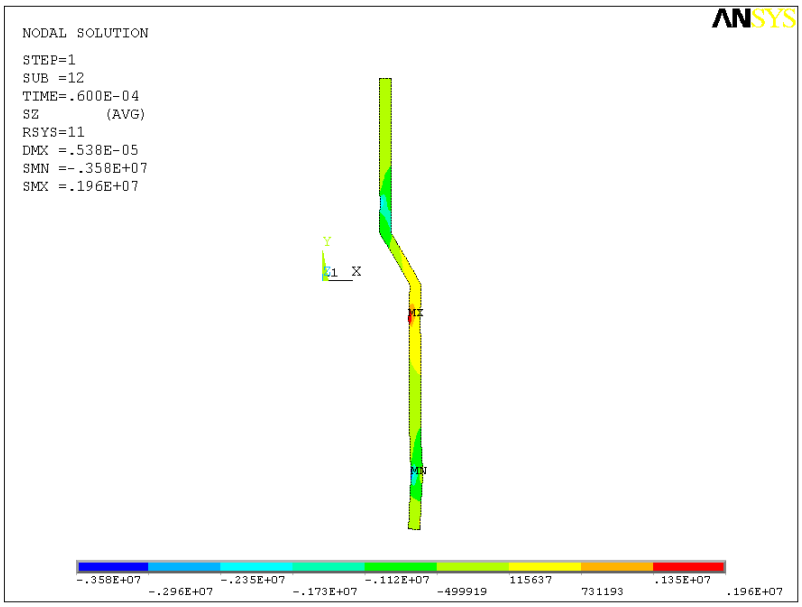

Figure 3.51: Axial normal stress (σ_z) values on GRP Coating at 0.06. ms.

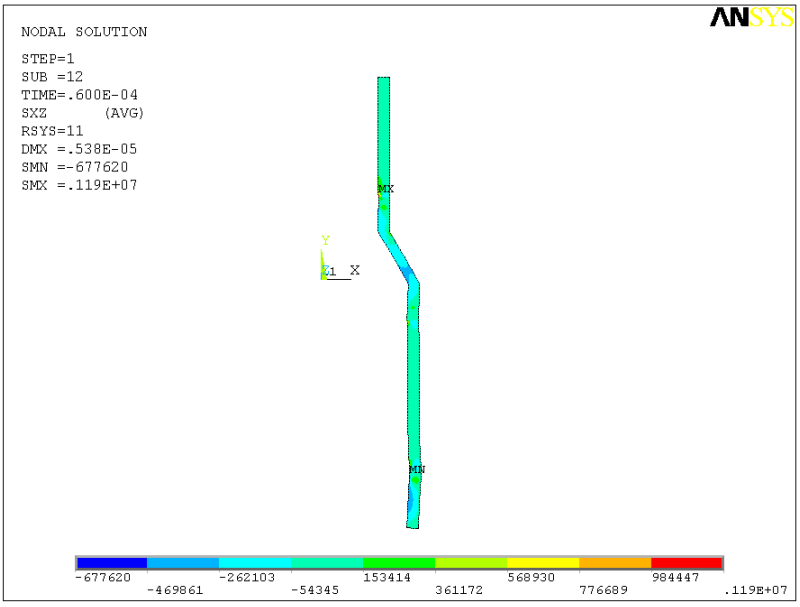

Figure 3.52: Shear stress (τ_{rz}) values on GRP Coating at 0.06. ms.

The stress components in principle material directions can be found by a similar stress transformation with the one in the static loading by means of Eqs. (3.5), (3.10), (3.11) and (3.12). Then, the failure index and stress ratio can be calculated by using (3.6), (3.7), (3.8) and (3.9) with Table 3.9.

As a result, the most critical F (maximum) and R (minimum) are found as ***0.011*** and ***51.8466***, respectively. Their locations are all points on a circle formed by 360° rotation of the point with the radial stress of ***0.52 MPa tensile*** (MX in Figure 3.49) about the symmetry axis. The stress components in cylindrical coordinates and in principal material directions for the most critical points are tabulated in Table 3.14.

Table 3.14: Stress components in cylindrical coordinates and in principal material directions for the most critical points of GRP Coating at 0.06. ms.

CYLINDRICAL COORDINATES						
Unit	σ_r	σ_θ	σ_z	$\tau_{\theta z}$	τ_{zr}	$\tau_{r\theta}$
MPa	2.03	-6.06	-9.90	0	1.09	0
PRINCIPAL MATERIAL DIRECTIONS						
Unit	σ_1	σ_2	σ_3	τ_{23}	τ_{31}	τ_{12}
MPa	-7.98	-7.98	2.03	-0.77	0.77	1.92

The failure index that is lower than 1 shows that the mechanical performance of GRP Coating under dynamic loading is sufficient according to Tsai-Wu failure theory. Moreover, the stress ratio (R) gives the dynamic loading at failure as ***25923.3g*** so a safety factor of up to ***51.8466*** can be taken for GRP Coating.

Finally, the mechanical performances of CRP Rods under dynamic loading are checked by Tsai-Wu failure theory again. The maximum stress components in

cylindrical coordinates, which occur again at 0.06. ms., are shown in the figures from Figure 3.53 to Figure 3.56.

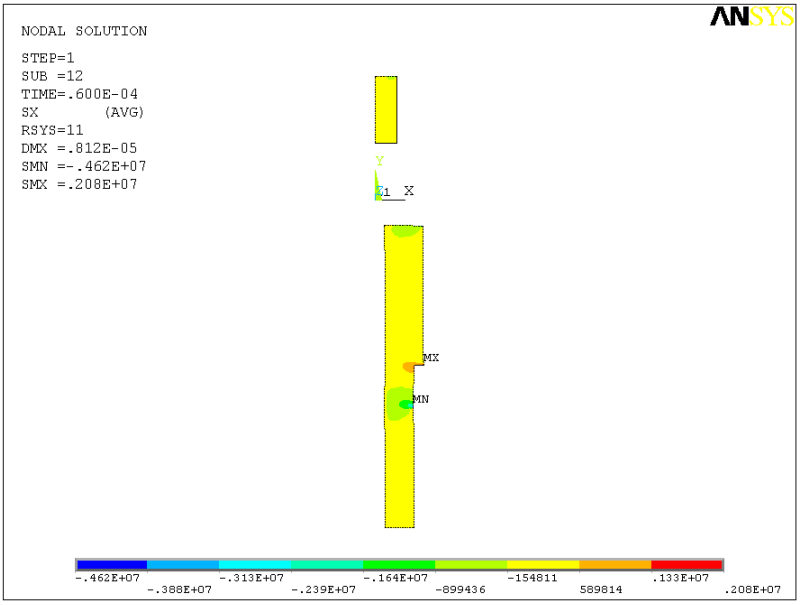

Figure 3.53: Radial normal stress (σ_r) values on CRP Rods at 0.06. ms.

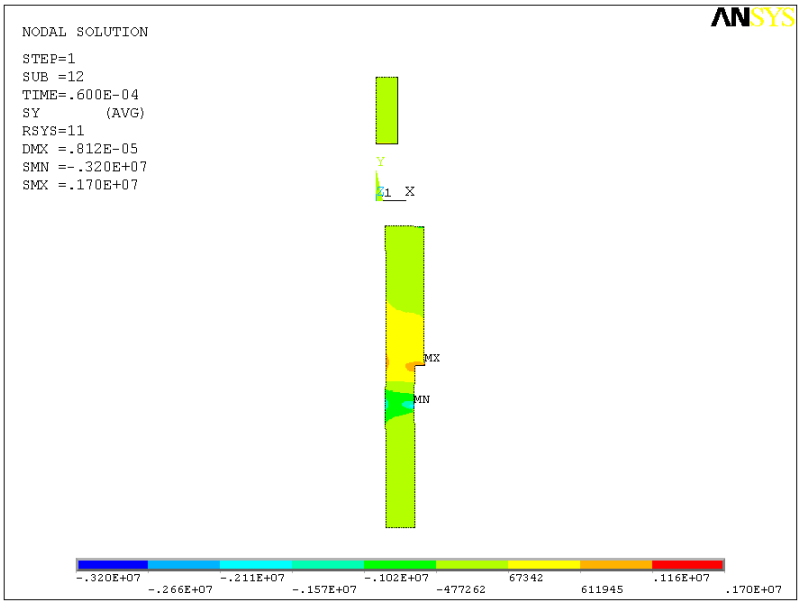

Figure 3.54: Tangential normal stress (σ_θ) values on CRP Rods at 0.06. ms.

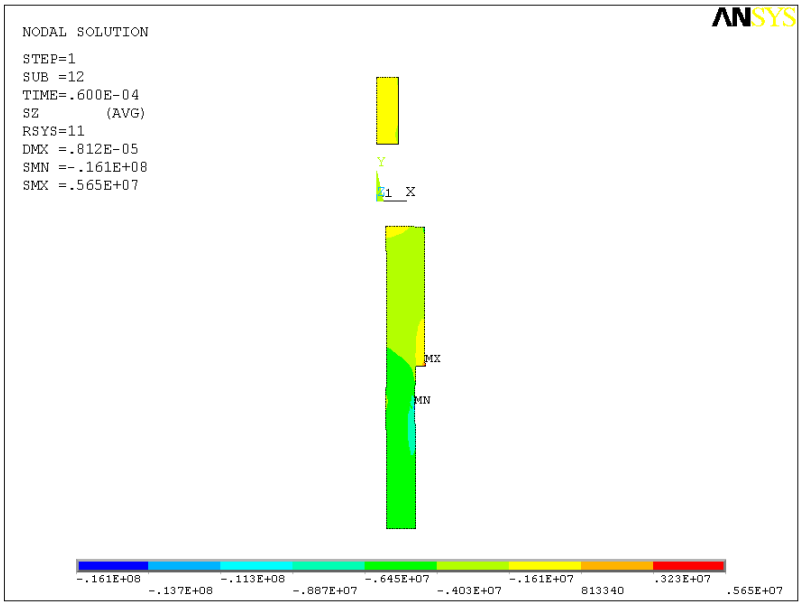

Figure 3.55: Axial normal stress (σ_z) values on CRP Rods at 0.06. ms.

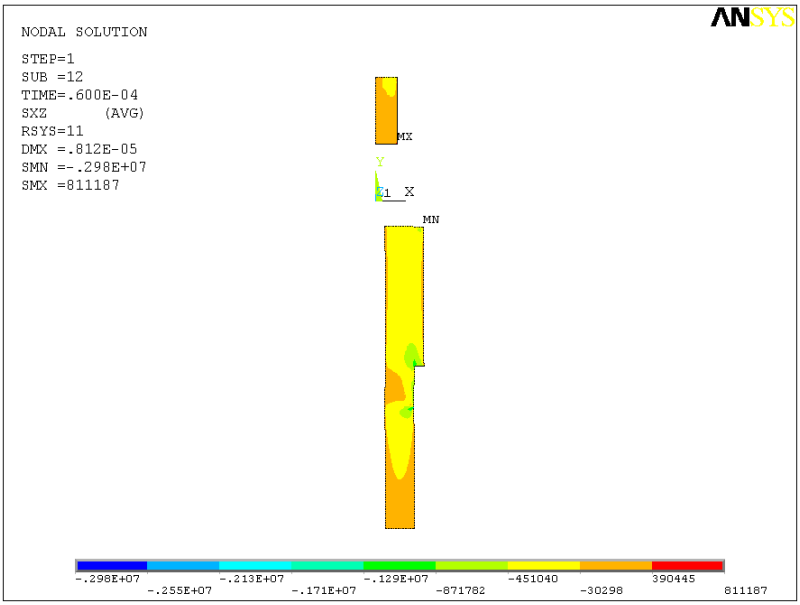

Figure 3.56: Shear stress (τ_{rz}) values on CRP Rods at 0.06. ms.

Stress transformation by using Eqs. (3.5) and (3.11) is required in order to find the stress components in principle material directions. Then, the failure index (F) and stress ratio (R) can be calculated by using Eqs. (3.1), (3.2), (3.3) and (3.4) with Table 3.7.

Consequently, the most critical F (maximum) and R (minimum) are found as ***0.081*** and ***10.6367***, respectively. Their locations are all points on a circle formed by 360° rotation of the point with the radial stress of ***2.08 MPa tensile*** (MX in Figure 3.53) about the symmetry axis. The stress components in cylindrical coordinates and in principal material directions for the most critical points are tabulated in Table 3.15.

Table 3.15: Stress components in cylindrical coordinates and in principal material directions for the most critical points of CRP Rods at 0.06. ms.

CYLINDRICAL COORDINATES						
Unit	σ_r	σ_θ	σ_z	$\tau_{\theta z}$	τ_{zr}	$\tau_{r\theta}$
MPa	2.08	1.70	5.65	0	-2.31	0
PRINCIPAL MATERIAL DIRECTIONS						
Unit	σ_1	σ_2	σ_3	τ_{23}	τ_{31}	τ_{12}
MPa	5.65	1.70	2.08	0	2.31	0

Since failure index (F) is lower than 1, no problem is expected about the mechanical performance of CRP Rods under dynamic loading according to Tsai-Wu failure theory. On the other hand, the stress ratio (R) gives the dynamic loading at failure as ***5318.35g*** so a safety factor of up to ***10.6367*** can be taken for CRP Rods.

In conclusion, the transducer designed can also be able to resist to dynamic loading of 500 g for 1 ms. Now, the thermal performance of the transducer must be checked, which are given in the following section.

3.1.3 Thermal Performance

The final step in the numerical design of the transducer is the analysis of thermal performance. In a transducer, the piezoelectric ceramics generate considerable heat, when they are driven at high powers. If the structure of the transducer does not allow adequate cooling, the transducer may not perform properly or reliably, and its lifetime may be considerably shortened [42].

The heat generation in the transducer is mainly due to the dissipated power loss, which includes mechanical and electrical losses. The mechanical losses are associated with viscous losses, damping losses and the elastic constants of the piezoelectric material, i.e., mechanical loss tangent ($\tan\delta_m$), whereas the electrical losses are related with the material's dielectric loss tangent ($\tan\delta_e$). However, the viscous and damping losses are negligible. Therefore, the mechanical losses are composed of only the mechanical loss tangent [42].

Moreover, since $\tan\delta_e$ is much larger than $\tan\delta_m$ at high electric field drive conditions, the mechanical loss tangent is also negligible. Thus, the total dissipated power loss for each tube is given below [42];

$$P_{loss} \cong P_e \tag{3.13}$$

In Eq. (3.13), the electrical losses (P_e) for each tube are calculated as follows [42]:

$$P_e = \omega E^2 K^T \varepsilon_0 V_c \tan\delta_e \tag{3.14}$$

where

ω	Resonance frequency in rad/s ($\omega = 2\pi f$)
E	Electric field
K^T	Relative permittivity
ε_0	Vacuum permittivity (8.854x10^{-12} F/m)
V_c	Volume of the PZT Tubes
$\tan\delta_e$	Dielectric loss tangent

Although a transducer can be driven at high powers, there is an upper limit for this power. This is the power when the electric field is *2000 V_{rms}/cm* because the piezoelectric properties of PZT Tubes begin to change significantly upon this field. In this study, the electric field is taken as 2000 V_{rms}/cm so the worst case can be checked.

Table 3.16: Operating parameters and total dissipated power loss for each tube

Property	***Symbol***	***Unit***	***Tube1***	***Tube2***
Resonance Frequency	f	kHz	59.5	31
Resonance Frequency	ω	rad/s	373850	194779
Electric Field	E	V_{rms}/cm	2000	2000
Relative Permittivity	K^T		1470	1470
Dielectric loss tangent	$\tan\delta_e$		0.01	0.01
Heat Generated Per Volume	p	MW/m^3	1.95	1.01
Volume	V_c	mm^3	1602	4336
Total Heat Generated	**P**	**W**	**3.12**	**4.40**

The parameters in Eq. (3.14), the total dissipated power loss and so the amount of heat generated in the tubes are shown in Table 3.16.

Some amount of this heat can be transferred to the surrounding water by convection and the remaining part increases the temperature of the transducer. In this study, the convection coefficient of the water is taken as *1350* W/m^2K. Moreover, the temperature of the water is taken as *35* $°C$ so that the cooling effect of the water is minimized in order to check the worst case.

After calculating the amount of heat generated in the tubes, the transducer is simulated with FEM in ANSYS in order to find the temperatures on it. The details about this simulation are given in Appendix H. The result of the simulation is shown in Figure 3.57.

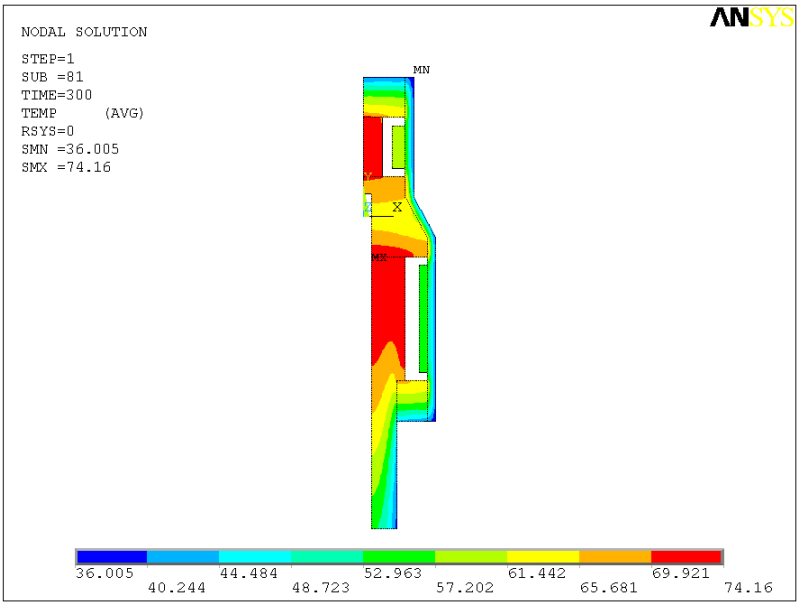

Figure 3.57: Steady state temperature distribution on the transducer

As mentioned in Appendix H, the simulation was performed for 300 seconds. The transducer reaches 99% of the maximum temperature in 164 seconds, as shown in Figure 3.58. As from this time, the process is steady state and the temperatures remain constant.

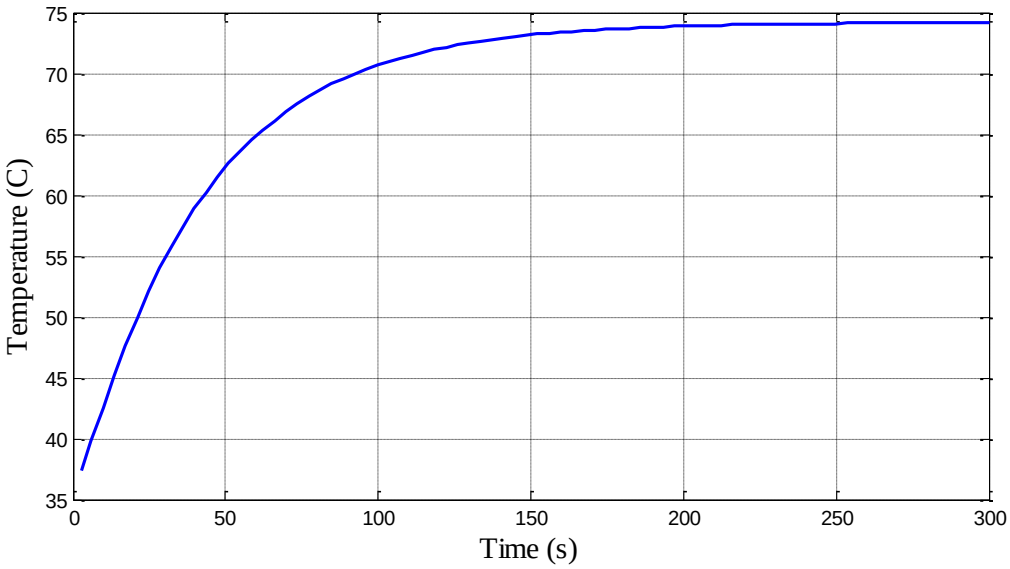

Figure 3.58: Transient temperature response of the point with the maximum temperature (MX in Figure 3.57)

The maximum and minimum temperatures on the components of the transducer are tabulated in Table 3.17.

Table 3.17: Steady state temperatures of the components of the transducer

	Unit	***PZT Tubes***	***CRP Caps***	***GRP Coating***	***CRP Rods***
Maximum Temperature	°C	59.32	74.13	68.09	74.16
Minimum Temperature	°C	53.23	38.84	36.01	38.43

For PZT Tubes, piezoelectric performance decreases as the operating temperature increases until Curie temperature, where complete and permanent depolarization occurs. Therefore, the Curie point is the absolute maximum temperature for the piezoelectric tubes. When the tubes are heated above the Curie point, all piezoelectric properties are lost. As a general rule, it is not recommended to exceed half of the Curie temperature. For PZT4, the Curie temperature is *330 °C* so the operating temperature should not exceed *165 °C* [43]. In this study, the maximum temperature occurred on PZT Tubes, i.e., 59.32, is lower than this limit. Thus, there is no thermal problem in terms of PZT Tubes.

On the other hand, for composites, matrix materials restrict the service temperature since they have lower service temperatures than the fibers. Therefore, the temperature limitations of CRP Caps, CRP Rods and GRP Coating depend on the service temperature of the epoxy resin used. Generally, it is about *125 °C* [37]. Hence, there are also no thermal problems in terms of these components.

As a result, the transducer designed can be able to resist to the operational temperatures. Here, the numerical design of the transducer finishes. In the following section, the experimental design is explained.

3.2 Experimental Design

Experimental design is the second phase of the design process. In this phase, the transducer is manufactured and some tests are applied to the transducer. By these tests, acoustic, mechanical and thermal performances of the transducer are examined. In this study, the manufacturing of the transducer and the tests were

performed in Bilkent Acoustics and Underwater Technologies Research Center (BASTA). The photograph of the transducer manufactured is shown in Figure 3.59.

Figure 3.59: Photograph of the transducer manufactured for the study

3.2.1 Acoustic Test

In this test, the electrical admittances of the tubes are measured in a water tank with an impedance analyzer that uses 1 V_{rms}. The water tank and impedance analyzer are shown in Figure 3.60 and Figure 3.61, respectively. The electrical admittances of the tubes found with this test are shown in Figure 3.62 and Figure 3.63.

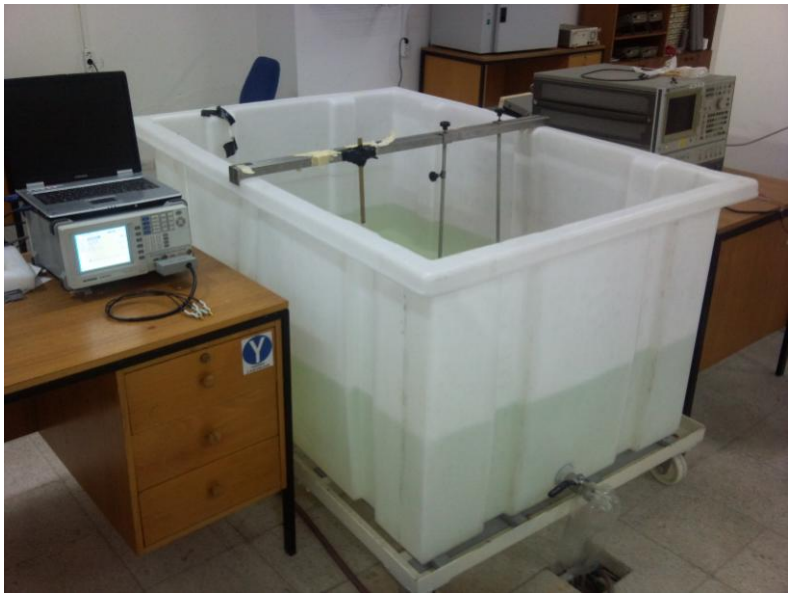

Figure 3.60: Photograph of the water tank used in the experimental design

Figure 3.61: Photograph of the impedance analyzer used in the experimental design

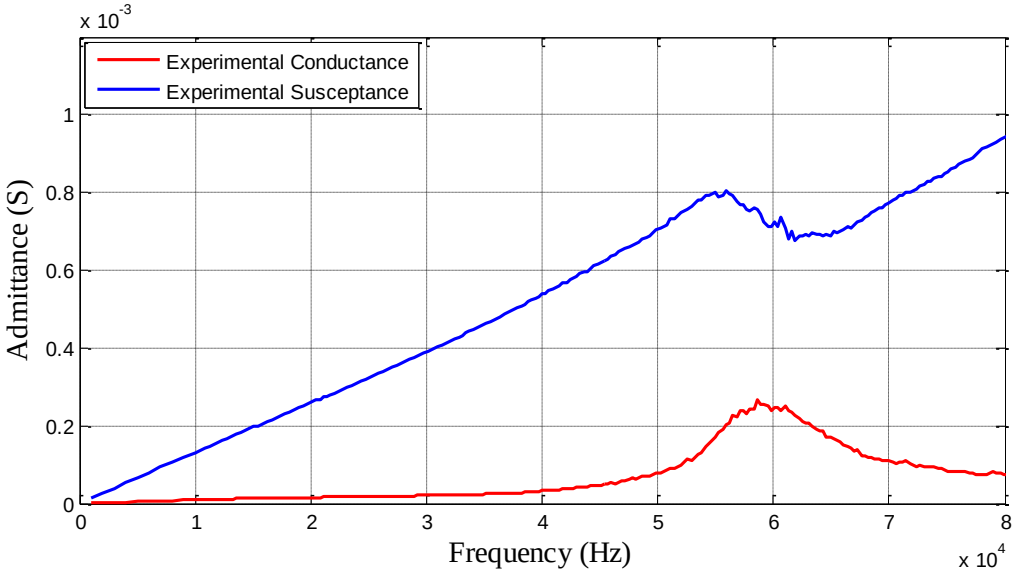

Figure 3.62: Electrical admittance of Tube1 found with acoustic test

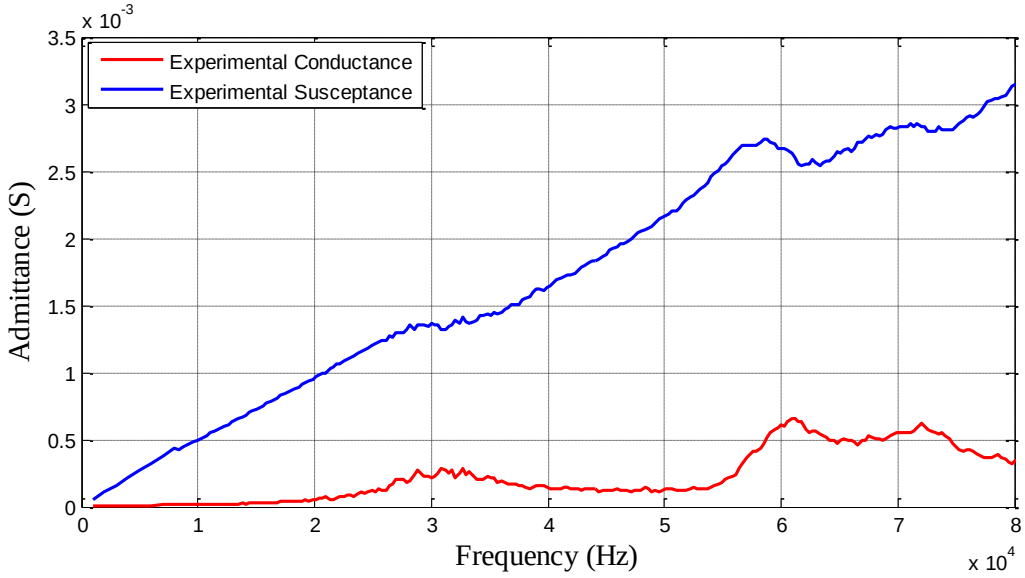

Figure 3.63: Electrical admittance of Tube2 found with acoustic test

The results including the resonance frequencies, bandwidths and electrical admittances of the tubes in the circumferential expansion mode are given in Table 3.18.

Table 3.18: Results of the acoustic test

	Resonance Frequency (kHz)	**-3 dB Bandwidth (kHz)**	**-6 dB Bandwidth (kHz)**	**Electrical Admittance (mS)**
Tube1	59.5	16.42	40.32	0.24+j 0.73
Tube2	31	22.24	27.53	0.28+j 1.36

According to the results, the transducer can be driven at two wide frequency bands centered at about 30 and 60 kHz. Therefore, the design and manufacture of the transducer can be considered successful in terms of the acoustic requirements. The comparison of the experimental results with the numerical ones is given in the *Chapter 4: Discussion and Conclusion*.

3.2.2 Mechanical Test

After the acoustic test, a mechanical test, i.e., a hydrostatic pressure test, is performed in order to evaluate the mechanical performance of the transducer. In this test, the transducer is loaded with a pressure of 30 bars in a pressure tank for 5 minutes. The pressure tank used in this study is shown in Figure 3.64. After loading, the electrical admittances of the tubes are measured again and any change is checked. In this study, no change was observed in the electrical admittances of the tubes after the pressure test so the transducer can be considered successful in terms of the mechanical requirements.

Figure 3.64: Photograph of the pressure tank used in the mechanical test

3.2.3 Thermal Test

Final test in the experimental design process is the thermal test. In this test, the transducer is driven with maximum allowable power for 5 minutes and then, the electrical admittances of the tubes are measured again. Any change is again checked for the evaluation. In this study, no change was observed in the electrical admittances of the tubes after the thermal test so thermal performance of the transducer can be considered sufficient.

CHAPTER 4

DISCUSSION & CONCLUSION

As a result, the design of a piezoelectric electroacoustic transducer that operates at two distinct frequency bands was accomplished both numerically and experimentally. In both phases of the design process, a broad acoustic bandwidth with enough mechanical and thermal performances could be obtained.

The numerical and experimental results about acoustic performance are generally similar except some differences. The electrical admittances of the tubes found numerically and experimentally are shown in Figure 4.1 and Figure 4.2. Firstly, the results about Tube1 almost coincide: the resonance frequency, bandwidth and electrical admittances have similar values. There is only a small difference between the susceptances. The slope of the susceptance depends mainly on the electrical capacitance of the piezoelectric tube, which is a function of the permittivity of the tube (ε_{33}). The permittivity is a material property of the PZT4 ceramic and its value has a tolerance. Also, it decreases with aging. Therefore, aging of the tube or the tolerance in the permittivity value may lead this difference between the susceptances.

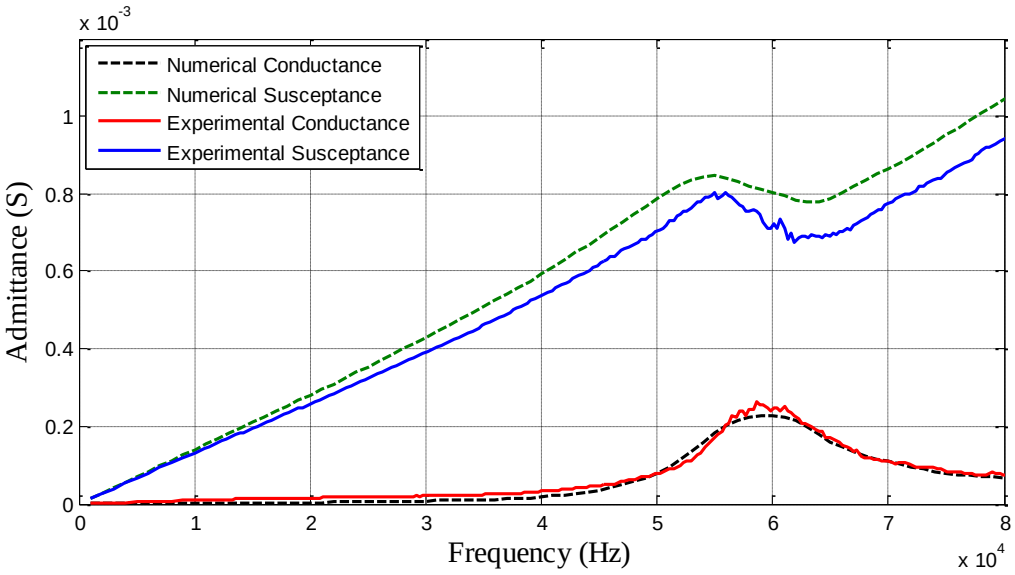

Figure 4.1: Comparison of the numerical and experimental admittances of Tube1

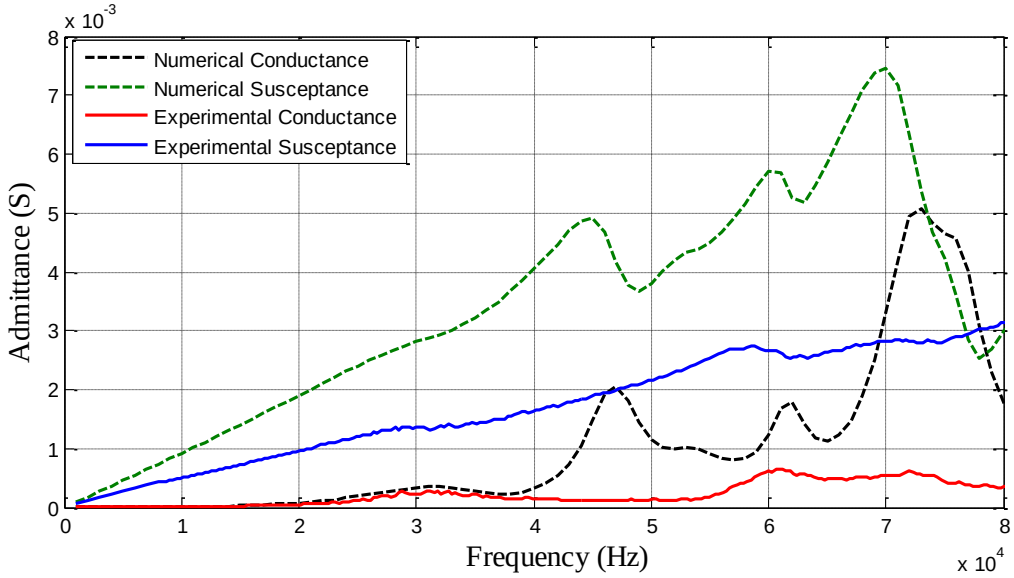

Figure 4.2: Comparison of the numerical and experimental admittances of Tube2

Secondly, the results about Tube2 coincide in the operating frequency band in terms of the conductances. However, in the other modes of Tube2, while the resonance frequencies overlap, there are some differences between the conductance values. These differences may result from the following reasons:

- Damping characteristics of the composite structures changes significantly with the frequency and the vibration mode. However, it was taken constant in this study. Therefore, it was not modeled accurately for all frequencies and modes.

- The mechanical properties of the composite structures obtained in the manufactured transducer may differ from the ones calculated and used in the numerical design phase.

- The piezoelectric properties of the PZT ceramic tubes have a tolerance about ±20%, which is given by the manufacturer of these tubes. The conductance value is proportional with the square of the piezoelectricity so it can vary between 64% and 144% of the value found numerically.

On the other hand, there is an excessive difference in the slopes of the susceptances. As mentioned before, this arises from the change in the electrical capacitance and so the permittivity of the ceramic tube. However, this difference is much more than the one that aging of the tube or tolerance in the value may lead. This difference is only possible with an excessive deviation from the material properties of PZT4 ceramic by a manufacturing defect during the production of the ceramic tube.

Finally, the experimental admittances of the tubes have wavy patterns because of the reflections from the walls of the water tank. This can be prevented by

either using a larger water tank, or performing the measurement many times by changing the position of the transducer in the tank and taking the average of these measurements.

REFERENCES

[1] Wikimedia Foundation Inc, *Transducer*: Wikipedia, the free encyclopedia. Available: http://en.wikipedia.org/wiki/Transducer, last visited on 2010, Jan. 12.

[2] McGuigan, B, *What are Transducers?* wiseGEEK. Available: http://www.wisegeek.com/what-are-transducers.htm, last visited on 2010, Jan. 12.

[3] Burdic, W. S, *Underwater Acoustic System Analysis*, 2nd ed. Englewood Cliffs, NJ: Prentice Hall, 1991.

[4] Urick, R. J, *Principles of underwater sound*, 3rd ed. New York, NY: McGraw-Hill, 1983.

[5] Randall, R. H, *An introduction to acoustics*. Mineola, NY: Dover Publications, 2005.

[6] Sherman, C. H. and Butler, J. L, *Transducers and Arrays for Underwater Sound*. New York, NY: Springer, 2007.

[7] Haines, G, *Sound Underwater*. New York, NY: David & Charles, 1974.

[8] Lurton, X, *An Introduction to Underwater Acoustics - Principles and Application*. New York, NY: Springer, 2002.

[9] Smith, S. E, *What is an Acoustic Mine?*: wiseGEEK. Available: http://www.wisegeek.com/what-is-an-acoustic-mine.htm, last visited on 2010, Jan. 14.

[10] Wass, *Anti-Torpedo Countermeasure System for Surface Ships*. [Brochure]. Available: http://www.wass.it/WASSWEB/brochure/C310.pdf, last visited on 2010, Jan. 15.

[11] Wikimedia Foundation Inc, *Ocean acoustic tomography*: Wikipedia, the free encyclopedia. Available: http://en.wikipedia.org/wiki/Acoustic_thermometry, last visited on 2010, Jan. 16.

[12] Wikimedia Foundation Inc, *SOSUS*: Wikipedia, the free encyclopedia. Available: http://en.wikipedia.org/wiki/Sosus, last visited on 2010, Jan. 17.

[13] Wikimedia Foundation Inc, *Piezoelectricity*: Wikipedia, the free encyclopedia. Available: http://en.wikipedia.org/wiki/Piezoelectricity, last visited on 2010, Jan. 19.

[14] American Piezo Ceramics, *Piezo Theory.* Available: http://www.americanpiezo.com/knowledge-center/piezo-theory.html, last visited on 19/01/10.

[15] Anissimov, M, *wiseGEEK: What is Piezoelectricity?* Available: http://www.wisegeek.com/what-is-piezoelectricity.htm.

[16] WordIQ, *Piezoelectricity - Definition.* Available: http://www.wordiq.com/definition/Piezoelectricity, last visited on 2010, Jan. 19.

[17] Gallego-Juarez, J. A, "Piezoelectric ceramics and ultrasonic transducers," *Journal of Physics E: Scientific Instruments*, vol. 22, p. 804, 1989.

[18] Chacón, D, RodrRiera-Franco Sarabia, E. de, & Gallego-Juárez, J. a, "A procedure for the efficient selection of piezoelectric ceramics constituting high-power ultrasonic transducers," *Ultrasonics*, vol. 44 Suppl 1, pp. e517-21, 2006.

[19] Silva, E. and Kikuchi, N, “Design of piezoelectric transducers using topology optimization,” *Smart Materials and Structures*, vol. 8, p. 350, 1999.

[20] Tressler, J, “Piezoelectric Transducer Designs for Sonar Applications,” *Piezoelectric and Acoustic Materials for Transducer Applications*, p. 217, 2008.

[21] Kunkel, H. a, Locke, S, & Pikeroen, B, “Finite-element analysis of vibrational modes in piezoelectric ceramic disks,” *IEEE transactions on ultrasonics, ferroelectrics, and frequency control*, vol. 37, no. 4, pp. 316-328, 1990.

[22] Yao, Q. and Bjørnø, L, “Transducers Based on Multimode Optimization,” *IEEE transactions on ultrasonics, ferroelectrics, and frequency control*, vol. 44, no. 5, pp. 1060-1066, 1997.

[23] Lin, S, Xu, L, & Wenxu, H, “A new type of high power composite ultrasonic transducer,” *Journal of Sound and Vibration*, vol. 330, no. 7, pp. 1419–1431, 2011.

[24] Lin, S. and Xu, C, “Analysis of the sandwich ultrasonic transducer with two sets of piezoelectric elements,” *Smart Mater. Struct*, vol. 17, no. 6, p. 65008, 2008.

[25] Lin, S. and Tian, H, “Study on the sandwich piezoelectric ceramic ultrasonic transducer in thickness vibration,” *Smart Materials and Structures*, vol. 17, no. 1, p. 15034.

[26] Lin, S, “An improved cymbal transducer with combined piezoelectric ceramic ring and metal ring,” *Sensors and Actuators A: Physical*, vol. 163, no. 1, pp. 266-276, 2010.

[27] Tressler, J. F, Newnham, R. E, & Hughes, W. J, “Capped ceramic underwater sound projector: The “cymbal” transducer,” *The Journal of the Acoustical Society of America*, vol. 105, no. 2, p. 591, 1999.

[28] Sun, D, Wang, S, Hata, S, & Shimokohbe, A, "Axial vibration characteristics of a cylindrical, radially polarized piezoelectric transducer with different electrode patterns," *Ultrasonics*, vol. 50, no. 3, pp. 403-410, 2010.

[29] Kim, J, Hwang, K, & Jeong, H, "Radial vibration characteristics of piezoelectric cylindrical transducers," *Journal of Sound and Vibration*, vol. 276, no. 3-5, pp. 1135-1144, 2004.

[30] Kim, J. and Lee, J, "Dynamic characteristics of piezoelectric cylindrical transducers with radial polarization," *Journal of Sound and Vibration*, vol. 300, no. 1-2, pp. 241-249, 2007.

[31] Lin, S, "Study on the radial composite piezoelectric ceramic transducer in radial vibration," *Ultrasonics*, vol. 46, no. 1, pp. 51-9, 2007.

[32] Liu, S. and Lin, S, "The analysis of the electro-mechanical model of the cylindrical radial composite piezoelectric ceramic transducer," *Sensors and Actuators A: Physical*, vol. 155, no. 1, pp. 175-180, 2009.

[33] Feng, F, Shen, J, & Deng, J, "A 2D equivalent circuit of piezoelectric ceramic ring for transducer design," *Ultrasonics*, vol. 44 Suppl 1, pp. e723-6, 2006.

[34] Lin, S, "Electro-mechanical equivalent circuit of a piezoelectric ceramic thin circular ring in radial vibration," *Sensors and Actuators A: Physical*, vol. 134, no. 2, pp. 505-512, 2007.

[35] Ramesh, R, Prasad, C. D, Kumar, T. K. V, Gavane, L. a, & Vishnubhatla, R. M. R, "Experimental and finite element modelling studies on single-layer and multi-layer 1-3 piezocomposite transducers," *Ultrasonics*, vol. 44, no. 4, pp. 341-9, 2006.

[36] Andrade, M. A. B, Alvarez, N. P, Buiochi, F, Negreira, C, & Adamowski, J. C, "Analysis of 1-3 piezocomposite and homogeneous piezoelectric rings for power ultrasonic transducers," *Journal of the Brazilian Society of Mechanical Sciences and Engineering*, vol. 31, no. 4, 2009.

[37] Mallick, P. K, *Fiber-Reinforced Composites: Materials, Manufacturing, and Design,* 3rd ed. Boca Raton, FL: CRC Press, 2007.

[38] R&G Composite Technology, *Composite Materials Handbook,* 8th ed.: [E-Book], 2008.

[39] R&G Composite Technology, *Composite Materials Handbook,* 9th ed.: [E-Book], 2009.

[40] Shigley, J. E, Mischke, C. R, & Budynas, R. G, *Mechanical engineering design,* 7th ed. New York, NY: McGraw-Hill, 2004.

[41] Kollár, L. P. and Springer, G. S, *Mechanics of composite structures*. New York, NY: Cambridge University Press, 2003.

[42] Butler, S. C, Blottman, J. B, & Montgomery, R. E, "A Thermal Analysis of High-Drive Ring Transducer Elements (NUWC-NPT Technical Report 11467)," Naval Undersea Warfare Center Division, New Port, RI, 2005.

[43] Morgan Technical Ceramics Electro Ceramics, *Piezoelectric Ceramics*. [Brochure]. Available: http://www.morganelectroceramics.com/products/sensors-transducers/, last visited on 2010, Oct. 08.

[44] *ANSYS® Multiphysics Release 11.0 Documentation*: ANSYS, Inc.

[45] Zebdi, O, Boukhili, R, & Trochu, F, "An Inverse Approach Based on Laminate Theory to Calculate the Mechanical Properties of Braided Composites," *Journal of Reinforced Plastics and Composites*, vol. 28, no. 23, pp. 2911-2930, 2008.

[46] Whitcomb, J. and Tang, X, "Effective Moduli of Woven Composites," *Journal of Composite Materials*, vol. 35, no. 23, pp. 2127-2144, 2001.

[47] Goyal, D, "Analysis of Stress Concentrations in 2 2 Braided Composites," *Journal of Composite Materials*, vol. 40, no. 6, pp. 533-546, 2005.

[48] MatWeb LLC, *Online Materials Information Resource.* Available: http://www.matweb.com/, last visited on 2010, May. 07.

APPENDIX A

MATHEMATICAL DESCRIPTION OF PIEZOELECTRICITY

In linear piezoelectricity, the equations of elasticity are coupled to the charge equation of electrostatics by means of piezoelectric constants. Hooke's Law describes the mechanical behavior of the material [13]:

$$S = sT \tag{A.1}$$

where S is strain, s is compliance matrix and T is stress.

On the other hand, the electrical behavior of the material is described as follows [13]:

$$D = \varepsilon E \tag{A.2}$$

where D is the electric charge density displacement (electric displacement), ε is permittivity and E is electric field strength.

These equations are combined into linear *coupled equations*, of which the strain-charge form is [6]:

$$S = s^E T + d^t E \tag{A.3a}$$

$$D = dT + \varepsilon^T E \tag{A.3b}$$

Equation (A.3a) represents the converse piezoelectric effect while Equation (A.3b) represents the direct piezoelectric effect. In these equations, S and T are 1 x 6 column matrices, E and D are 1 x 3 column matrices, s^E is a 6 x 6 matrix of elastic compliance, *d* is a 3 x 6 matrix of piezoelectric coefficients (d^t is the transpose of d) and ε^T is a 3 x 3 matrix of permittivity. The superscript *E* indicates a zero or constant stress whereas the superscript *T* indicates a zero or constant electric field. The matrix forms of the equations are as follows [6]:

$$\begin{bmatrix} S_1 \\ S_2 \\ S_3 \\ S_4 \\ S_5 \\ S_6 \end{bmatrix} = \begin{bmatrix} s_{11}^E & s_{12}^E & s_{13}^E & 0 & 0 & 0 \\ s_{21}^E & s_{22}^E & s_{23}^E & 0 & 0 & 0 \\ s_{31}^E & s_{32}^E & s_{33}^E & 0 & 0 & 0 \\ 0 & 0 & 0 & s_{44}^E & 0 & 0 \\ 0 & 0 & 0 & 0 & s_{55}^E & 0 \\ 0 & 0 & 0 & 0 & 0 & s_{66}^E = 2\left(s_{11}^E - s_{12}^E\right) \end{bmatrix} \begin{bmatrix} T_1 \\ T_2 \\ T_3 \\ T_4 \\ T_5 \\ T_6 \end{bmatrix} + \begin{bmatrix} 0 & 0 & d_{31} \\ 0 & 0 & d_{32} \\ 0 & 0 & d_{33} \\ 0 & d_{24} & 0 \\ d_{15} & 0 & 0 \\ 0 & 0 & 0 \end{bmatrix} \begin{bmatrix} E_1 \\ E_2 \\ E_3 \end{bmatrix}$$

$$\begin{bmatrix} D_1 \\ D_2 \\ D_3 \end{bmatrix} = \begin{bmatrix} 0 & 0 & 0 & 0 & d_{15} & 0 \\ 0 & 0 & 0 & d_{24} & 0 & 0 \\ d_{31} & d_{32} & d_{33} & 0 & 0 & 0 \end{bmatrix} \begin{bmatrix} T_1 \\ T_2 \\ T_3 \\ T_4 \\ T_5 \\ T_6 \end{bmatrix} + \begin{bmatrix} \varepsilon_{11} & 0 & 0 \\ 0 & \varepsilon_{22} & 0 \\ 0 & 0 & \varepsilon_{33} \end{bmatrix} \begin{bmatrix} E_1 \\ E_2 \\ E_3 \end{bmatrix}$$

Another equation pair in stress-charge form is as follows:

$$T = c^E S - e^t E \tag{A.4a}$$

$$D = eS - \varepsilon^S E \tag{A.4b}$$

where c^E is a 6 x 6 matrix of elastic stiffness, e is a 3 x 6 matrix of piezoelectric coefficients (e^t is the transpose of e) and ε^S is a 3 x 3 matrix of permittivity at constant strain.

The relationships between c^E and s^E, e and d, and between ε^S and ε^T matrices are given in the following equations:

$$c^E = s^{E^{-1}} \tag{A.5}$$

$$e = d c^E \tag{A.6}$$

$$\varepsilon^S = \varepsilon^T - d e^t \tag{A.7}$$

APPENDIX B

ELECTRICAL EQUIVALENT CIRCUIT MODEL METHOD (EECMM)

Electrical equivalent circuit model method (EECMM) is an effective way of modeling piezoelectric transducers. It provides an opportunity to visualize the mechanical properties of a transducer in an electrical circuit. The simplest way for this method is use of electrical elements such as *inductors, resistors and capacitors* to represent *mass, resistance (damping) and compliance (the inverse of stiffness)*, respectively. Moreover, in this method, *voltage, V, and current, I*, are used to represent *force, F, and velocity, u*, respectively. Then, the analogies between the laws of electricity and the laws of mechanics are as follows [6]:

- For an electrical resistance R_e, the voltage $V = R_e I$
  For a mechanical resistance R, the force $F = Ru$

- For a coil of inductance L, the voltage $V = L\, dI/dt = j\omega LI$
  For an ideal mass M, the force $F = M\, du/dt = j\omega Mu$

- For a capacitor C the voltage $V = (1/C) \int Idt = I/j\omega C$
  For a compliance C_m^e the force $F = (1/C_m^e) \int udt = u/j\omega C_m^e$

- For an electrical transformer of turns ratio N the output voltage is NV
  For an electro-mechanical transformer the force F = NV

- Electrical power is $W = VI = |V|^2/2R_e = |I|^2 R_e/2$
  Mechanical power is $W = Fu = |F|^2/2R = |u|^2 R/2$

Angular resonance frequency, ω_r, and quality factor, Q, analogies are:

- For inductance L, capacitor C, resonance is $\omega_r = (1/LC)^{1/2}$
  For mass M, compliance C_m^e, resonance is $\omega_r = (1/MC_m^e)^{1/2}$

- For inductance L, resistance R_e, the Q is $Q = \omega_r L/R_e$
  For mass M, mechanical resistance R, Q is $Q = \omega_r M/R$

Since "jω" term indicates the sinusoidal conditions, an electrical equivalent circuit can represent a mechanical vibrating system by replacing voltage, V, with force, F, and the current, I, with velocity, u [6]. Therefore, the vibration of a transducer is characterized by its *"electrical admittance"*, which is equivalent to *"mobility"* in mechanics by analogy.

- Electrical Admittance: $Y = I / V$ (B.1)
  Mobility (Mechanical Admittance): $Y = u / F$ (B.2)

Electrical admittance, which is inverse of *"electrical impedance (Z)"*, is a complex value and its unit is *"Siemens (S)"*

$$Y = G + jB \text{ (Conductance + j Susceptance)} \quad \text{(B.3)}$$

The admittance of a transducer can be found from its equivalent circuit, which is shown in Figure B.1. Since an electroacoustic transducer has both electrical and

mechanical parts, the equivalent circuit involves an ideal electromechanical transformer connecting both parts.

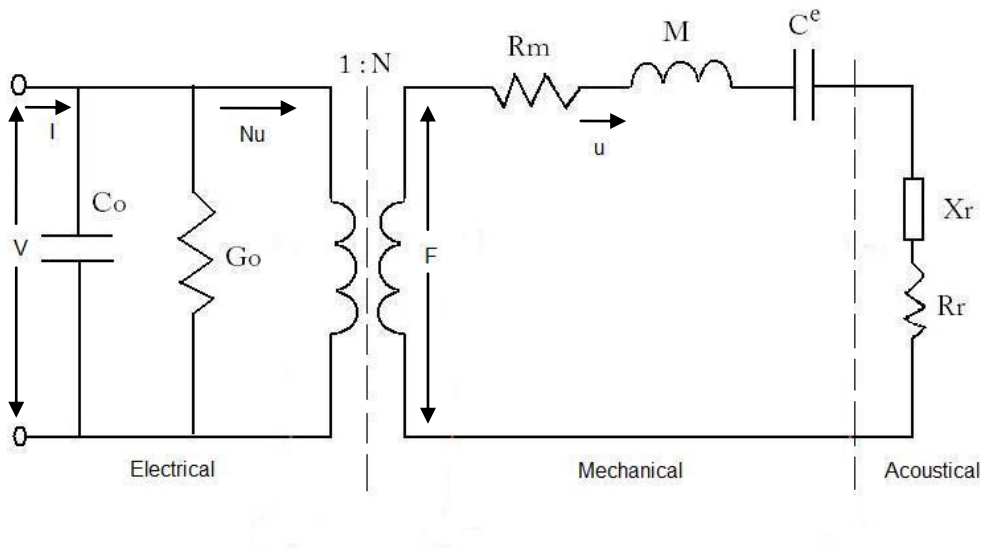

Figure B.1: Electrical Equivalent Circuit of an Electroacoustic Transducer [6]

The electromechanical turns ratio of the ideal transformer, N, is called the "*transduction coefficient"*. This turns ratio, which is proportional to the coupling coefficient, connects the electrical and mechanical parts of the circuit by the relations [6];

$$F = NV \text{ and } u = I / N \tag{B.4}$$

In the equivalent circuit, there is an acoustical part in addition to the electrical and mechanical parts. Acoustical part represents the acoustic radiation of the transducer.

The definitions of the parameters in the circuit and their formulas for a radially polarized cylindrical piezoelectric tube operating in 3-1 mode are as follows:

B.1. Electrical Part:

- **C_0:** Electrical capacitance of the tube [6]

$$C_0 = \frac{2\pi aL}{t}\varepsilon_{33}^T \tag{B.5}$$

where

a Average radius of the cylinder tube

L Length of the cylinder tube

t Thickness of the cylinder tube

ε_{33}^T Permittivity of the tube for dielectric displacement and electric field in direction 3 (radial direction) under constant stress [14]

$$\varepsilon_{33}^T = \varepsilon_{r33}^T \varepsilon_0 \tag{B.6}$$

ε_{r33}^T Relative permittivity of the tube for dielectric displacement and electric field in direction 3 under constant stress [14]

ε_0 Vacuum Permittivity $(8.854\times10^{-12}\ F/m)$

- **G_0:** Electrical loss conductance of the tube [6]

$$G_0 = \omega C_f \tan\delta \tag{B.7}$$

where

ω Frequency in rad/s

$$\omega = 2\pi f \tag{B.8}$$

f Frequency in Hz

C_f Free capacitance (Capacitance without any mechanical load under a free boundary condition where the stress is zero [6])

$$C_f = \frac{C_0}{1 - {k_{33}}^2} \tag{B.9}$$

k_{33} Electromechanical coupling factor between electric field in direction 3 and longitudinal vibrations in direction 3 [14]

$\tan\delta$ *Electrical* dissipation factor

B.2. Mechanical Part:

- **R_m:** Mechanical resistance (damping) of the tube

- **M:** Mass of the tube

$$M = 2\pi atL\rho \tag{B.10}$$

where

ρ Density of the tube

❖ **C^e:** Mechanical compliance of the tube under short circuit conditions (the reciprocal of the stiffness) [6]

$$C^e = \frac{1}{K^E} = \frac{a}{2\pi t L} S_{11}^E \tag{B.11}$$

where

K^E Elastic stiffness of the tube

S_{11}^E Elastic compliance of the tube for stress in direction 1 (tangential direction) and accompanying strain in direction 1, under constant electric field (short circuit) [14]

B.3. Acoustical Part:

❖ **X_r:** Radiation reactance (the imaginary part of the radiation impedance).

❖ **R_r:** Radiation resistance (the real part of the radiation impedance).

Z_r: Radiation impedance (the complex ratio of the acoustic force on the tube surface caused by its vibration to the velocity of the surface)

$$Z_r = R_r + jX_r \tag{B.12}$$

For a radiating sphere, the radiation impedance is as follows [6]:

$$Z_r = R_r + jX_r = A\rho_0 c_0 \left[\frac{(ka_s)^2 + j(ka_s)}{1+(ka_s)^2} \right] \tag{B.13}$$

Equation (B.13) can also be applied to a cylindrical tube by using the radius of an equivalent sphere having the same radiating area for mean radius (a_s) in the formula.

$$a_s = \sqrt{\frac{aL}{2}} \tag{B.14}$$

where

A Radiation (outer surface) area of the cylinder tube

$$A = 4\pi a_s{}^2 = 2\pi aL \tag{B.15}$$

ρ_0 Density of the water

c_0 Sound speed in water

k Wave number

$$k = \frac{\omega}{c_0} \tag{B.16}$$

Moreover,

N: Electromechanical turns ratio [6]

$$N = \frac{2\pi L d_{31}}{S_{11}^E} \tag{B.17}$$

where

d_{31} Induced polarization in direction 3 per unit stress applied in direction 1 (piezoelectric charge constant) [14]

The impedance of the right-hand side of the electromechanical transformer (mechanical and acoustical parts) is calculated from the following equation;

$$Z_{right} = R_m + j\omega M + \frac{1}{j\omega C^e} + Z_r \tag{B.18}$$

Then, Z_{right} is transformed to the electrical part of the circuit with the turns ratio of the electromechanical transformer.

$$Z_{left} = \frac{Z_{right}}{N^2} \tag{B.19}$$

After transformation, there are three parallel elements in the electrical part so the total impedance of the whole circuit is calculated from parallel circuit theory as follows:

$$\frac{1}{Z_{total}} = \frac{1}{Z_{left}} + j\omega C_0 + G_0 \tag{B.20}$$

Electrical admittance is the inverse of electrical impedance;

$$Y = \frac{1}{Z_{total}} \tag{B.21}$$

Inserting Eqs. (B.18), (B.19) and (B.20) into Eq. (B.21), the admittance of a transducer is found as follows:

$$Y = \frac{I}{V} = \left[\frac{N^2}{R_m + j\omega M + \frac{1}{j\omega C^e} + Z_r} \right] + j\omega C_0 + G_0 \qquad \text{(B.22)}$$

Moreover, R_m can be neglected since it is very small compared to R_r. Similarly, G_0 is also negligible. As a result, the input admittance of a transducer is given below;

$$Y = \frac{I}{V} = \left[\frac{N^2}{j\omega M + \frac{1}{j\omega C^e} + Z_r} \right] + j\omega C_0 \qquad \text{(B.23)}$$

The material properties of the piezoelectric tubes used in this study are given below in Table B.1.

Table B.1: Material properties of PZT4 type cylindrical piezoelectric tubes [43]

Property	***Symbol***	***Unit***	***Value***
Electrical			
Relative Permittivity	$\varepsilon_r^{T}{}_{33}$		1470
Dielectric Loss @ 2kV/cm	Tanδ		0.017
Electro-Mechanical			
Coupling Factor	k_{33}		0.71
Charge Constant or Strain Constant	d_{31}	$x10^{-12}$ C/N or m/V	-132
Mechanical			
Compliance	$S^{E}{}_{11}$	$x10^{-12}$ m^2/N	12.7
Density	ρ	kg/m^3	7600

Moreover, water density and speed of sound in water are taken as *1000 kg/m^3*, *1500 m/s*, respectively.

APPENDIX C

ACOUSTIC SIMULATIONS OF THE PZT TUBES WITH FINITE ELEMENT METHOD (FEM) IN ANSYS

Finite element method is a comprehensive and informative method used for analyzing the acoustic performance of a transducer. For this method, ANSYS 11.0 Multiphysics is used in this study. ANSYS is capable of performing coupled-field analysis so a coupled acoustic analysis, which takes the fluid-structure interaction into account, can be accomplished. Moreover, piezoelectric analysis is possible in ANSYS by using the proper element types. Therefore, a piezoelectric transducer being submerged in water can be modeled in ANSYS.

Although ANSYS assumes that the fluid is compressible, it allows only relatively small pressure changes with respect to the mean pressure. Furthermore, the fluid is assumed to be non-flowing and inviscid (viscosity causes no dissipative effects) [44].

Due to the rotational symmetry of the tubes, a 2-D axisymmetric model is used for the study. The model and finite element mesh are shown in Figure C.1. In the model, *PLANE13*, a 2-D axisymmetric coupled-field element with piezoelectricity capability, is used for PZT tube, whereas *FLUID29*, a 2-D axisymmetric harmonic acoustic fluid element, is used for surrounding water.

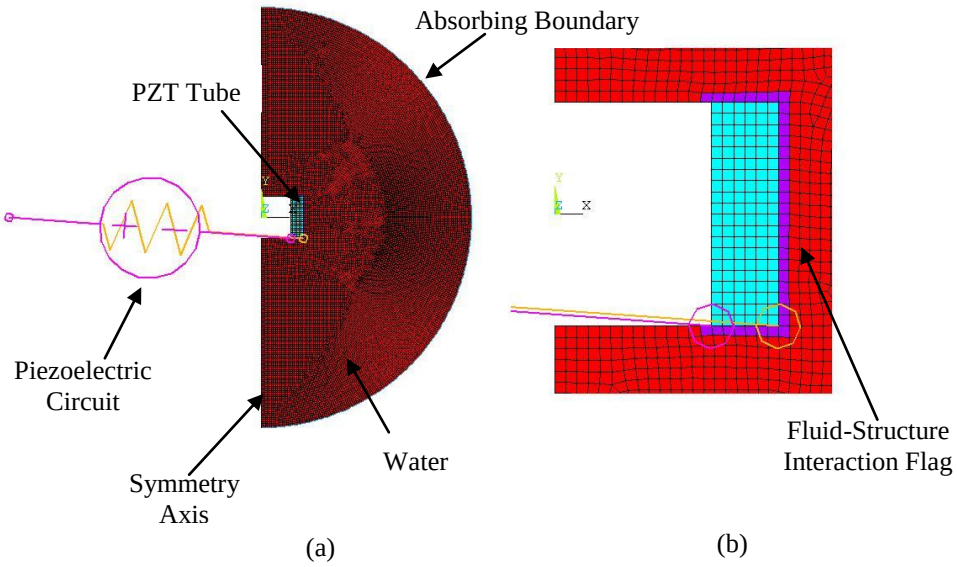

Figure C.1: (a) Axisymmetric finite element model of a PZT tube, (b) the details of the model.

On the other hand, *FLUID129*, a 2-D infinite acoustic element, is used for simulating the infinite extent of the fluid medium. This infinite acoustic element provides an absorbing condition so that an outgoing pressure wave reaching the boundary of the model is absorbed with minimum reflections back into the fluid domain. ANSYS documentation states that the placement of the absorbing element at a distance of approximately 0.2λ from the boundary of any structure that may be submerged in the fluid can produce accurate results. Here, λ represents the dominant wavelength of the pressure waves;

$$\lambda = \frac{c}{f} \tag{C.1}$$

where *"c"* is the speed of sound in the fluid and *"f"* is the dominant frequency of the pressure wave [44].

In order to obtain accurate results, the mesh size is kept at a value smaller than *1/15* of the dominant wavelength (λ). On the other hand, the fluid-structure interaction flag in the model causes the acoustic pressure to exert a force on the structure so that the structural motions provide an effective fluid load [44].

For a radially polarized tube, the electrode surfaces are the inner and outer surfaces of the tube. Therefore, the voltage degree of freedom for the nodes lying on each of these surfaces is coupled separately so that two distinct electrodes are created. Then, a potential difference (V) is applied between these electrodes with a circuit consisting of a resistor and a voltage source from *CIRCU94*, which is a circuit element for use in piezoelectric-circuit analysis. As a result, harmonic analysis with no mechanical damping is performed in the frequency range 0-80 kHz. The electrical admittance of the tube can be found from Equation (B.1);

$$Y = \frac{I}{V} \tag{B.1}$$

where I is the electric current passing through the CIRCU94 resistor element and V is the potential difference between the inner and outer electrodes.

Material properties required for a piezoelectric tube are dielectric (relative permittivity) constants, elastic coefficient matrix, piezoelectric matrix and density. In ANSYS, the piezoelectric matrix can be defined in [e] form (piezoelectric stress matrix) or in [d] form (piezoelectric strain matrix). Similarly, the elastic coefficient matrix can be defined in the form of the stiffness matrix [C] or in the form of the compliance matrix [S], whereas the relative permittivity can be at constant strain [ε_r^S] or at constant stress [ε_r^T]. On the other hand, density and speed of sound are the material properties required

for the water. The material properties of the PZT tube and water used in the model are shown in Table C.1 and Table C.2, respectively.

Table C.1: Material properties of the PZT tube used in the model [43]

PZT4 TUBE			
Property	***Symbol***	***Unit***	***Value***
Electrical			
Relative Permittivity	$\varepsilon_r^T{}_{33}$		1470
	$\varepsilon_r^T{}_{11}$		1650
Electro-Mechanical			
Charge Constants or Strain Constants	d_{33}	$x10^{-12}$ C/N or m/V	315
	d_{31}	$x10^{-12}$ C/N or m/V	-132
	d_{15}	$x10^{-12}$ C/N or m/V	511
Mechanical			
Compliances	$S^E{}_{33}$	$x10^{-12}$ m^2/N	15.6
	$S^E{}_{11}$	$x10^{-12}$ m^2/N	12.7
	$S^E{}_{12}$	$x10^{-12}$ m^2/N	-3.86
	$S^E{}_{13}$	$x10^{-12}$ m^2/N	-5.76
	$S^E{}_{55}$	$x10^{-12}$ m^2/N	39.2
	$S^E{}_{66}$	$x10^{-12}$ m^2/N	33.12
Density	ρ	kg/m^3	7600

where

$\varepsilon_r^T{}_{11}$ Relative permittivity of the tube for dielectric displacement and electric field in direction 1 (tangential direction) under constant stress [14]

d_{33} Induced polarization in direction 3 (radial direction) per unit stress applied in direction 3 [14]

d_{15} Induced polarization in direction 1 per unit shear stress applied about direction 2 (axial direction) [14]

$S^E{}_{33}$ Elastic compliance of the tube for stress in direction 3 and accompanying strain in direction 3, under constant electric field (short circuit) [14]

Table C.2: Material properties of the water used in the model [43]

PZT4 TUBE			
Property	***Symbol***	***Unit***	***Value***
Density	ρ	kg/m^3	1000
Velocity of Sound	c	m/s	1500

APPENDIX D

ACOUSTIC SIMULATIONS OF THE TRANSDUCER WITH FINITE ELEMENT METHOD (FEM) IN ANSYS

For the acoustic simulations of the transducer, ANSYS 11.0 Multiphysics is used again. Similarly, a 2-D axisymmetric model is employed since the geometry, loading and material properties have a rotational symmetry. The model and finite element mesh are shown in Figure D.1.

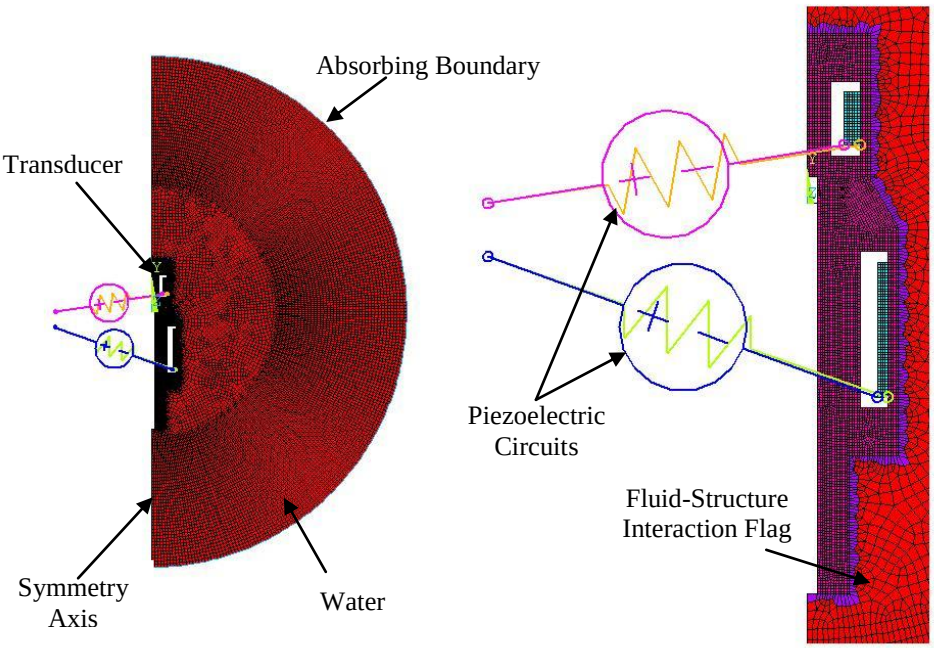

Figure D.1: (a) Axisymmetric finite element model of transducer designed, (b) the details of the model.

In the model of the transducer, *PLANE183*, a 2-D axisymmetric structural solid element, is used for the frame and coating [44]. For the other components, the same element types with the acoustic simulation of PZT tubes explained in Appendix C are employed. The element types of all the parts in the model are listed in Table D.1.

Table D.1: Element types used in the model

Component Name	***Element Type***
CRP Caps	PLANE183
CRP Rods	PLANE183
GRP Coating	PLANE183
PZT Tubes	PLANE13
Water	FLUID29
Infinite Boundary	FLUID129
Piezoelectric Circuits	CIRCU94

In the same way, the absorbing boundary is placed at a distance of approximately 0.2λ from the boundary of the transducer. The mesh size is also kept at a value smaller than 1/15 of the dominant wavelength.

In the model, there are distinct circuits for each PZT tube. However, the tubes do not operate together. In each simulation, only one of the tubes operates so a voltage difference is applied to only that tube. As a result, harmonic analysis with some mechanical damping is performed in the frequency range 0-80 kHz. The electrical admittance of the tube can be found from its own circuit.

The material properties of CRP Caps, CRP Rods and GRP Coating should be calculated since they are composite structures. They are tabulated in Table D.2,

Table D.3 and Table D.4. The details about these calculations are given in Appendix E. For PZT tubes and water, the material properties given in Table C.1 and Table C.2 are used. Damping ratios for composite structures and PZT tubes are taken as *0.04* and *0.001*, respectively.

Table D.2: Material properties of CRP Caps used in the model

CRP CAPS								
Property	***Unit***	***Value***						
Stiffness Matrix [E]	GPa		***r***	***θ***	***z***	***θz***	***zr***	***rθ***
		r	57.74	21.26	8.39	0	0	0
		θ		57.74	8.39	0	0	0
		z			18.24	0	0	0
		θz				5.14	0	0
		zr	SYMMETRY				5.14	0
		rθ						18.24
Density (ρ)	kg/m^3	1515						

Table D.3: Material properties of CRP Rods used in the model

CRP RODS								
Property	***Unit***	***Value***						
Stiffness Matrix [E]	GPa		***r***	***θ***	***z***	***θz***	***zr***	***rθ***
		r	25.08	11.06	11.06	0	0	0
		θ		25.08	11.06	0	0	0
		z			147.13	0	0	0
		θz				7.21	0	0
		zr	SYMMETRY				7.21	0
		rθ						7.01
Density (ρ)	kg/m^3	1566						

Table D.4: Material properties of GRP Coating used in the model

GRP COATING								
Property	***Unit***	***Value***						
Stiffness Matrix [E]	GPa		***r***	***θ***	***z***	***θz***	***zr***	***rθ***
		r	19.86	4.90	4.90	0	0	0
		θ		26.12	12.47	0	0	0
		z			26.12	0	0	0
		θz				14.39	0	0
		zr	SYMMETRY				7.14	0
		rθ						7.14
Density (ρ)	kg/m^3	2064						

APPENDIX E

CALCULATIONS OF MATERIAL PROPERTIES OF COMPOSITE STRUCTURES IN THE TRANSDUCER

Fiber-reinforced composite materials consist of fibers of high strength and modulus embedded in a matrix. Therefore, they can have some properties that neither of the constituents has alone. In composites, fibers are the principal load-carrying members, whereas the matrix acts as a load transfer medium between fibers and keeps fibers in the desired position. A large number of fibers in a thin layer of matrix form a *lamina (ply)*. In the lamina, continuous fibers may be arranged either in a unidirectional orientation (i.e., all fibers in one direction), in a bidirectional orientation (i.e., fibers in two directions, usually normal to each other) or in a multidirectional orientation (i.e., fibers in more than two directions). In order to obtain the thickness required in a composite structure, several laminas are stacked in a specified sequence to form a *laminate* [37].

Fiber-reinforced composites are *orthotropic materials*, which contain three orthogonal planes of material property symmetry, namely, the 1-2, 2-3, 1-3 planes shown in Figure E.1. The intersections of these symmetry planes, namely, axes 1, 2 and 3, are called the *principal material directions*. Contrary to *isotropic materials*, whose properties are the same in all directions, tensile normal stresses applied in any other direction than the principal material directions create both extensional and shear deformations in orthotropic

materials. This phenomenon is called *extension-shear coupling*. In order to characterize orthotropic materials, 9 independent elastic constants (E_{11}, E_{22}, E_{33}, G_{12}, G_{13}, G_{23}, v_{12}, v_{13}, and v_{23}) are required [37].

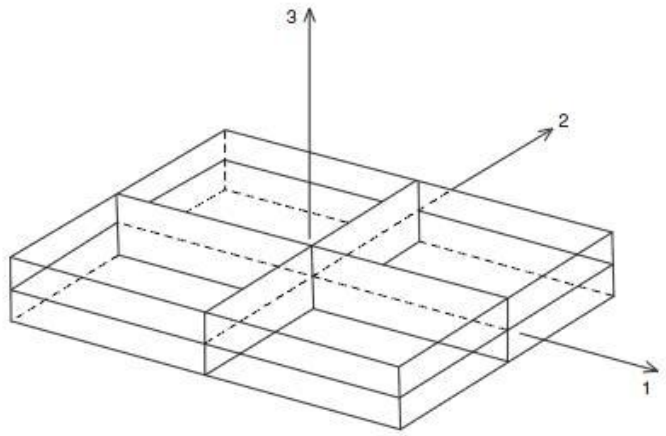

Figure E.1: Three plane of symmetry in an orthotropic material [37]

Composite materials used in this study include *carbon and glass fibers* embedded in an *epoxy matrix*. GRP Coating is composed of plies formed from bidirectional E-Glass woven fabrics. On the other hand, CRP Caps consists of a laminate including unidirectional T300 carbon fibers oriented in different directions, whereas CRP Rods include unidirectional T300 carbon fibers. The independent elastic constants of these composite components can be calculated from the elastic properties of the fibers and matrix if the volumetric ratio of fibers in the mixture and layup of the composite (fiber orientations in a sequence) are known. In the calculations, the fiber and matrix are assumed to be isotropic and their elastic properties are shown in Table E.1. Moreover, the volumetric fiber ratios and layup of the components are shown in Table E.2

Table E.1: Elastic properties of fibers and matrix used in the study [41]

T300 CARBON FIBERS			
Property	***Symbol***	***Unit***	***Value***
Elastic Modulus	E	GPa	231
Poisson's Ratio	ν		0.27
Density	ρ	kg/m^3	1770
E-GLASS FIBERS			
Elastic Modulus	E	GPa	72
Poisson's Ratio	ν		0.09
Density	ρ	kg/m^3	2600
EPOXY			
Elastic Modulus	E	GPa	4.4
Poisson's Ratio	ν		0.36
Density	ρ	kg/m^3	1260

Table E.2: Volumetric fiber ratios and layup of the components [38] [39]

CRP CAPS		
Property	***Symbol***	
Volumetric Fiber Ratio	v_f	0.50
Layup		$\{[0 / 45 / 90 / -45]_S\}_{18}$
CRP RODS		
Volumetric Fiber Ratio	v_f	0.60
Layup		unidirectional
GRP COATING		
Volumetric Fiber Ratio	v_f	0.60
Layup		$[\pm 45]^f_8$

The mechanics of fiber-reinforced composite materials are studied at two levels [37]:

- *The micromechanics level*, in which the interaction of fibers and matrix is examined on a microscopic scale.
- *The macromechanics level*, in which the response of a fiber-reinforced composite to mechanical and thermal loads is examined on a macroscopic scale. In this level, the material is assumed to be homogenous.

The calculations of the elastic constants of the composite structures begin in micromechanics level. In this level, *rule of mixtures* is used in order to calculate the elastic properties of a lamina. There are some assumptions in this approach [37]:

- Fibers are uniformly distributed throughout the matrix.
- Perfect bonding exists between the fibers and the matrix.
- The matrix is free of voids.
- The applied force is either parallel or normal to the fiber direction.
- The lamina is initially in a stress-free state (no residual stresses are present).
- Both fibers and matrix behave as linearly elastic materials.

A unidirectional continuous fiber lamina is a special class of orthotropic materials, in which the elastic properties are equal in the 2-3 direction. Therefore, $E_{22} = E_{33}$, $\nu_{12} = \nu_{13}$, $G_{12} = G_{13}$. Moreover, G_{23} can be expressed in terms of E_{22} and ν_{23}. Thus, the number of independent elastic constants for a unidirectional lamina reduces to 5, namely, E_{11}, E_{22}, ν_{12}, G_{12}, ν_{23}. These materials are called *transversely isotropic.* Also, if principal material directions

(1 and 2) coincide with the loading axes (x and y), i.e., the fiber orientation angle is *0* or *90*, ν_{23} can be related to ν_{12} and ν_{21}. As a result, the number of independent elastic constants of these materials, which are called *specially orthotropic*, is 4 (E_{11}, E_{22}, ν_{12}, G_{12}). The elastic properties of a specially orthotropic lamina are calculated as follows [37]:

❖ *Longitudinal modulus (E_{11}):*

$$E_{11} = E_f v_f + E_m v_m = E_f v_f + E_m (1 - v_f) \tag{E.1}$$

❖ *Transverse modulus (E_{22}):*

$$E_{22} = \frac{E_f E_m}{E_f v_m + E_m v_f} \tag{E.2}$$

❖ *Major in-plane Poisson's ratio (υ_{12}):*

$$\upsilon_{12} = \upsilon_f v_f + \upsilon_m v_m \tag{E.3}$$

❖ *In-plane shear modulus (G_{12}):*

$$G_{12} = \frac{G_f G_m}{G_f v_m + G_m v_f} \tag{E.4}$$

Furthermore, $\upsilon_{21} \neq \upsilon_{12}$ and $\upsilon_{31} \neq \upsilon_{13}$ but $\upsilon_{31} = \upsilon_{21}$. However, υ_{21} is not an independent elastic constant since it is defined as follows:

❖ *Minor in-plane Poisson's ratio (υ_{21}):*

$$\upsilon_{21} = \left(\frac{E_{22}}{E_{11}}\right)\upsilon_{12} \tag{E.5}$$

❖ *Out-of-plane Poisson's ratio (υ_{23}):*

$$\upsilon_{23} = \upsilon_{32} = \upsilon_{12}\frac{(1-\upsilon_{21})}{(1-\upsilon_{12})} \tag{E.6}$$

❖ *Out-of-plane shear modulus (G_{23}):*

$$G_{23} = f(E_{22}, \upsilon_{23}) = \frac{E_{22}}{2(1+\upsilon_{23})} \tag{E.7}$$

While the values for the longitudinal modulus (E_{11}) and major in-plane Poisson's ratio (ν_{12}) found with the equations above agree well with the measurements, there is disagreement for the transverse modulus (E_{22}) and in-plane shear modulus (G_{12}). The modified equations are given below [38] [39]:

❖ *Modified transverse modulus (E_{22_modified}):*

$$E_{22\_\text{modified}} = \frac{E_m^*\left(1+0.85{v_f}^2\right)}{v_f\frac{E_m^*}{E_f}+{v_m}^{1.25}} \tag{E.8}$$

where

$$E_m^* = \frac{E_m}{1-\nu_m{}^2} \tag{E.9}$$

❖ *Modified in-plane shear modulus (G_{12_modified}):*

$$G_{12\_\text{modified}} = \frac{G_m\left(1+0.6\nu_f{}^{0.5}\right)}{\nu_f \frac{G_m}{G_f} + \nu_m{}^{1.25}} \tag{E.10}$$

For a specially orthotropic lamina, the strain-stress relationship and the *compliance matrix ([S])* are as follows [41]:

$$\begin{Bmatrix} \varepsilon_1 \\ \varepsilon_2 \\ \varepsilon_3 \\ \gamma_{23} \\ \gamma_{13} \\ \gamma_{12} \end{Bmatrix} = \underbrace{\begin{bmatrix} \frac{1}{E_{11}} & -\frac{\upsilon_{21}}{E_{22}} & -\frac{\upsilon_{21}}{E_{22}} & 0 & 0 & 0 \\ -\frac{\upsilon_{12}}{E_{11}} & \frac{1}{E_{22}} & -\frac{\upsilon_{23}}{E_{22}} & 0 & 0 & 0 \\ -\frac{\upsilon_{12}}{E_{11}} & -\frac{\upsilon_{23}}{E_{22}} & \frac{1}{E_{22}} & 0 & 0 & 0 \\ 0 & 0 & 0 & \frac{2\left(1+\upsilon_{23}\right)}{E_{22}} & 0 & 0 \\ 0 & 0 & 0 & 0 & \frac{1}{G_{12}} & 0 \\ 0 & 0 & 0 & 0 & 0 & \frac{1}{G_{12}} \end{bmatrix}}_{[S]} \begin{Bmatrix} \sigma_1 \\ \sigma_2 \\ \sigma_3 \\ \tau_{23} \\ \tau_{13} \\ \tau_{12} \end{Bmatrix} \tag{E.11}$$

However, if the fiber orientation in a lamina is other than 0° or 90°, it is called *general orthotropic lamina* and the compliance matrix of the lamina must be transformed as follows [41]:

$$[\bar{S}] = [T_\varepsilon][S][T_\sigma]^{-1} \tag{E.12}$$

where

$$[T_\varepsilon] = \begin{bmatrix} c^2 & s^2 & 0 & 0 & 0 & cs \\ s^2 & c^2 & 0 & 0 & 0 & -cs \\ 0 & 0 & 1 & 0 & 0 & 0 \\ 0 & 0 & 0 & c & -s & 0 \\ 0 & 0 & 0 & s & c & 0 \\ -2cs & 2cs & 0 & 0 & 0 & c^2 - s^2 \end{bmatrix} \qquad \begin{matrix} c = \cos(\theta_3) \\ s = \sin(\theta_3) \end{matrix} \tag{E.13}$$

$$[T_\sigma] = \begin{bmatrix} c^2 & s^2 & 0 & 0 & 0 & 2cs \\ s^2 & c^2 & 0 & 0 & 0 & -2cs \\ 0 & 0 & 1 & 0 & 0 & 0 \\ 0 & 0 & 0 & c & -s & 0 \\ 0 & 0 & 0 & s & c & 0 \\ -cs & cs & 0 & 0 & 0 & c^2 - s^2 \end{bmatrix} \qquad \begin{matrix} c = \cos(\theta_3) \\ s = \sin(\theta_3) \end{matrix} \tag{E.14}$$

Note that, the transformation is about the principal material direction 3. Therefore, the transformation angle (θ_3) is the rotation of this coordinate and it is measured from the first coordinate (principle material direction 1) to the second coordinate (x direction). Moreover, it is positive in counterclockwise direction. Then, the strain-stress relationship for a general orthotropic lamina is as follows:

$$\begin{Bmatrix} \varepsilon_x \\ \varepsilon_y \\ \varepsilon_z \\ \gamma_{yz} \\ \gamma_{xz} \\ \gamma_{xy} \end{Bmatrix} = \begin{bmatrix} \overline{S}_{11} & \overline{S}_{12} & \overline{S}_{13} & 0 & 0 & 0 \\ \overline{S}_{21} & \overline{S}_{22} & \overline{S}_{23} & 0 & 0 & 0 \\ \overline{S}_{31} & \overline{S}_{32} & \overline{S}_{33} & 0 & 0 & 0 \\ 0 & 0 & 0 & \overline{S}_{44} & 0 & 0 \\ 0 & 0 & 0 & 0 & \overline{S}_{55} & 0 \\ 0 & 0 & 0 & 0 & 0 & \overline{S}_{66} \end{bmatrix} \begin{Bmatrix} \sigma_x \\ \sigma_y \\ \sigma_z \\ \tau_{yz} \\ \tau_{xz} \\ \tau_{xy} \end{Bmatrix} \tag{E.15}$$

Moreover, the stress-strain relationships and the *stiffness matrices* ($[C]$ & $[\overline{C}]$) of a specially and general orthotropic laminas are as follows [41]:

$$\{\sigma_{1,2,3}\} = [C]\{\varepsilon_{1,2,3}\} \quad , \quad \{\sigma_{x,y,z}\} = [\overline{C}]\{\varepsilon_{x,y,z}\} \tag{E.16}$$

$$[C] = [S]^{-1} \quad , \quad [\overline{C}] = [\overline{S}]^{-1} \tag{E.17}$$

On the other hand, in plane-stress condition, where σ_z, τ_{yz} *and* τ_{xz} are zero, the stress-strain relationship and the *reduced stiffness matrix ([Q])* for a specially orthotropic lamina, is as follows [41]:

$$\begin{Bmatrix} \sigma_1 \\ \sigma_2 \\ \tau_{12} \end{Bmatrix} = \underbrace{\begin{bmatrix} \frac{E_{11}}{D} & \frac{\upsilon_{12}E_{22}}{D} & 0 \\ \frac{\upsilon_{12}E_{22}}{D} & \frac{E_{22}}{D} & 0 \\ 0 & 0 & G_{12} \end{bmatrix}}_{[Q]} \begin{Bmatrix} \varepsilon_1 \\ \varepsilon_2 \\ \gamma_{12} \end{Bmatrix} \tag{E.18}$$

where

$$D = 1 - \frac{E_{22}}{E_{11}}\upsilon_{12}{}^2 = 1 - \upsilon_{12}\upsilon_{21} \tag{E.19}$$

Similarly, the reduced stiffness matrix for a general orthotropic lamina can be found by transformation as follows [41]:

$$\left[\overline{Q}\right]=\left[T_\sigma\right]\left[Q\right]\left[T_\varepsilon\right]^{-1} \tag{E.20}$$

where

$$\left[T_\sigma\right]=\begin{bmatrix} c^2 & s^2 & 2cs \\ s^2 & c^2 & -2cs \\ -cs & cs & c^2-s^2 \end{bmatrix} \qquad \begin{matrix} c=\cos(\theta) \\ s=\sin(\theta) \end{matrix} \tag{E.21}$$

$$\left[T_\varepsilon\right]=\begin{bmatrix} c^2 & s^2 & cs \\ s^2 & c^2 & -cs \\ -2cs & 2cs & c^2-s^2 \end{bmatrix} \qquad \begin{matrix} c=\cos(\theta) \\ s=\sin(\theta) \end{matrix} \tag{E.22}$$

Therefore, the stress-strain relationship for a general orthotropic lamina in plane-stress condition is as follows [41]:

$$\begin{Bmatrix} \sigma_x \\ \sigma_y \\ \tau_{xy} \end{Bmatrix}=\begin{bmatrix} \overline{Q}_{11} & \overline{Q}_{12} & 0 \\ \overline{Q}_{21} & \overline{Q}_{22} & 0 \\ 0 & 0 & \overline{Q}_{66} \end{bmatrix}\begin{Bmatrix} \varepsilon_x \\ \varepsilon_y \\ \gamma_{xy} \end{Bmatrix} \tag{E.23}$$

After calculating the stiffness or compliance of each lamina in a laminate from the elastic properties of the constituents, i.e. fiber and matrix, the elastic properties of the laminate can be found by macromechanics approach. In this approach, the *lamination theory* is used. The assumptions of this theory are as follows [37]:

- ❖ Laminate is thin and wide, i.e. width >> thickness
- ❖ Interlaminar bond between various laminas is perfect.
- ❖ Strain distribution is linear in the thickness direction.
- ❖ All laminas are macroscopically homogenous and behave in a linearly elastic manner.

For thick laminates such as CRP Caps (i.e., 9 mm thickness) in this study, the lamination theory gives inaccurate results. To overcome this, the laminate is divided into sublaminates, each of which has its own elastic constants. Then, the total laminate can be modeled with FEM by taking the thickness of each element as same as the thickness of the corresponding sublaminate [41].

On the other hand, woven fabrics are different from the laminates since they possess an undulated architecture due to the interlaced strands (i.e., bundles of continuous fibers). The fibers in woven fabrics have undulating and straight regions so they deviate from the unidirectionality. Therefore, the strength and stiffness of this type of composites are different from the ones of laminates, depending on the weaving parameters such as waviness ratio (ratio of the height to the wavelength of the strand). As the waviness ratio lowers, the woven fabric converges to the laminate. Since there is no general theory to calculate the properties of woven composites, they are generally assimilated to equivalent laminate by neglecting the undulation and strand shear effects. On the other hand, some researchers have developed analytical methods that take into account the undulation geometry, whereas the others use FEM to predict the elastic properties of woven composites [45] [46] [47]. In this study, the woven fabrics in GRP Coating are approximated by lamination theory.

In lamination theory, firstly, the *extensional stiffness matrix for the laminate [A]*, which relates the in-plane forces to the in-plane deformations, is calculated [41]:

$$A_{ij} = \sum_{k=1}^{K} \left(\overline{Q}_{ij}\right)_k \left(z_k - z_{k-1}\right) \tag{E.24}$$

where

K Total number of laminas in the laminate

$\left(\overline{Q}_{ij}\right)_k$ Elements of the stiffness matrix of the k[th] lamina

z_k Distance from the midplane to the bottom of the k[th] lamina

z_{k-1} Distance from the midplane to the top of the k[th] lamina

Note that positive z direction is from midplane to the bottom of the laminate.

Then, the *compliance matrix ([J])* and *stiffness matrix ([E])* of the laminate can be calculated. The strain-stress relationship, compliance and stiffness matrices of the laminate are as follows [41]:

$$\begin{Bmatrix} \overline{\varepsilon}_x \\ \overline{\varepsilon}_y \\ \overline{\varepsilon}_z \\ \overline{\gamma}_{yz} \\ \overline{\gamma}_{xz} \\ \overline{\gamma}_{xy} \end{Bmatrix} = \underbrace{\begin{bmatrix} J_{11} & J_{12} & J_{13} & J_{14} & J_{15} & J_{16} \\ J_{21} & J_{22} & J_{23} & J_{24} & J_{25} & J_{26} \\ J_{31} & J_{32} & J_{33} & J_{34} & J_{35} & J_{36} \\ J_{41} & J_{42} & J_{43} & J_{44} & J_{45} & J_{46} \\ J_{51} & J_{52} & J_{53} & J_{54} & J_{55} & J_{56} \\ J_{61} & J_{62} & J_{63} & J_{64} & J_{65} & J_{66} \end{bmatrix}}_{[J]} \begin{Bmatrix} \overline{\sigma}_x \\ \overline{\sigma}_y \\ \overline{\sigma}_z \\ \overline{\tau}_{yz} \\ \overline{\tau}_{xz} \\ \overline{\tau}_{xy} \end{Bmatrix} \tag{E.25}$$

$$[E] = [J]^{-1} \tag{E.26}$$

where $\bar{\sigma}$ and $\bar{\varepsilon}$ denotes the average stresses and average strains across the laminate.

❖ *Elements of [J] due to in-plane stresses* [41]:

$$\begin{Bmatrix} \bar{\varepsilon}_x \\ \bar{\varepsilon}_y \\ \bar{\gamma}_{xy} \end{Bmatrix} = \begin{bmatrix} J_{11} & J_{12} & J_{16} \\ J_{21} & J_{22} & J_{26} \\ J_{61} & J_{62} & J_{66} \end{bmatrix} \begin{Bmatrix} \bar{\sigma}_x \\ \bar{\sigma}_y \\ \bar{\tau}_{xy} \end{Bmatrix} \tag{E.27}$$

$$\{\bar{\varepsilon}_z\} = \begin{bmatrix} J_{31} & J_{32} & J_{36} \end{bmatrix} \begin{Bmatrix} \bar{\sigma}_x \\ \bar{\sigma}_y \\ \bar{\tau}_{xy} \end{Bmatrix} \tag{E.28}$$

$$\begin{Bmatrix} \bar{\gamma}_{yz} \\ \bar{\gamma}_{xz} \end{Bmatrix} = \begin{bmatrix} J_{41} & J_{42} & J_{46} \\ J_{51} & J_{52} & J_{56} \end{bmatrix} \begin{Bmatrix} \bar{\sigma}_x \\ \bar{\sigma}_y \\ \bar{\tau}_{xy} \end{Bmatrix} \tag{E.29}$$

where

$$\begin{bmatrix} J_{11} & J_{12} & J_{16} \\ J_{21} & J_{22} & J_{26} \\ J_{61} & J_{62} & J_{66} \end{bmatrix} = h_s [A]^{-1} \tag{E.30}$$

Note that h_s is the total thickness of the laminate.

$$\begin{bmatrix} J_{31} & J_{32} & J_{36} \end{bmatrix} = \sum_{k=1}^{K} \left(\begin{bmatrix} \bar{S}_{13} & \bar{S}_{23} & \bar{S}_{36} \end{bmatrix}_k (z_k - z_{k-1}) \left[\bar{Q}\right]_k \right) [A]^{-1} \tag{E.31}$$

For in-plane loading, $\bar{\tau}_{yz} = \bar{\tau}_{xz} = 0$ so $\bar{\gamma}_{yz} = \bar{\gamma}_{xz} = 0$. Therefore, the left-hand side of Eq. (E.29) is zero. In order to satisfy Eq. (E.29), the elements of the compliance matrix must be zero:

$$\begin{bmatrix} J_{41} & J_{42} & J_{46} \\ J_{51} & J_{52} & J_{56} \end{bmatrix} = \begin{bmatrix} 0 & 0 & 0 \\ 0 & 0 & 0 \end{bmatrix} \tag{E.32}$$

❖ *Elements of [J] due to out-of-plane normal stresses* [41]:

$$\begin{Bmatrix} \bar{\varepsilon}_x \\ \bar{\varepsilon}_y \\ \bar{\gamma}_{xy} \end{Bmatrix} = \begin{bmatrix} J_{13} \\ J_{23} \\ J_{63} \end{bmatrix} \bar{\sigma}_z \tag{E.33}$$

$$\bar{\varepsilon}_z = J_{33}\, \bar{\sigma}_z \tag{E.34}$$

$$\begin{Bmatrix} \bar{\gamma}_{yz} \\ \bar{\gamma}_{xz} \end{Bmatrix} = \begin{bmatrix} J_{43} \\ J_{53} \end{bmatrix} \bar{\sigma}_z \tag{E.35}$$

where

$$\begin{bmatrix} J_{13} \\ J_{23} \\ J_{63} \end{bmatrix} = -\begin{bmatrix} J_{11} & J_{12} & J_{16} \\ J_{21} & J_{22} & J_{26} \\ J_{61} & J_{62} & J_{66} \end{bmatrix} \frac{1}{h_s} \sum_{k=1}^{K} \left(\begin{Bmatrix} \bar{C}_{13} \\ \bar{C}_{23} \\ \bar{C}_{63} \end{Bmatrix}_k \frac{(z_k - z_{k-1})}{(\bar{C}_{33})_k} \right) \tag{E.36}$$

$$J_{33} = \frac{1}{h_s} \sum_{k=1}^{K} \left(\frac{z_k - z_{k-1}}{(\bar{C}_{33})_k} \right) - \begin{bmatrix} J_{31} & J_{32} & J_{36} \end{bmatrix} \frac{1}{h_s} \sum_{k=1}^{K} \left(\begin{Bmatrix} \bar{C}_{13} \\ \bar{C}_{23} \\ \bar{C}_{63} \end{Bmatrix}_k \frac{(z_k - z_{k-1})}{(\bar{C}_{33})_k} \right) \tag{E.37}$$

Similarly, $\bar{\tau}_{yz} = \bar{\tau}_{xz} = 0$ so $\bar{\gamma}_{yz} = \bar{\gamma}_{xz} = 0$. Therefore, the left-hand side of Eq. (E.35) is zero. In order to satisfy Eq. (E.35), the elements of the compliance matrix must be zero:

$$\begin{bmatrix} J_{43} \\ J_{53} \end{bmatrix} = \begin{bmatrix} 0 \\ 0 \end{bmatrix} \tag{E.38}$$

❖ *Elements of [J] due to out-of-plane shear stresses* [41]:

$$\begin{Bmatrix} \bar{\gamma}_{yz} \\ \bar{\gamma}_{xz} \end{Bmatrix} = \begin{bmatrix} J_{44} & J_{45} \\ J_{54} & J_{55} \end{bmatrix} \begin{Bmatrix} \bar{\tau}_{yz} \\ \bar{\tau}_{xz} \end{Bmatrix} \tag{E.39}$$

$$\begin{Bmatrix} \bar{\varepsilon}_{x} \\ \bar{\varepsilon}_{y} \\ \bar{\varepsilon}_{z} \\ \bar{\gamma}_{xy} \end{Bmatrix} = \begin{bmatrix} J_{14} & J_{15} \\ J_{24} & J_{25} \\ J_{34} & J_{35} \\ J_{64} & J_{65} \end{bmatrix} \begin{Bmatrix} \bar{\tau}_{yz} \\ \bar{\tau}_{xz} \end{Bmatrix} \tag{E.40}$$

where

$$\begin{bmatrix} J_{44} & J_{45} \\ J_{54} & J_{55} \end{bmatrix} = \frac{1}{h_s} \sum_{k=1}^{K} \left(\left(z_k - z_{k-1} \right) \begin{bmatrix} \bar{S}_{44} & \bar{S}_{45} \\ \bar{S}_{45} & \bar{S}_{55} \end{bmatrix}_k \right) \tag{E.41}$$

Transverse shear stresses on the laminate result in only transverse shear strains ($\bar{\gamma}_{yz}$ and $\bar{\gamma}_{xz}$). All the other strains are zero. Therefore, the left-hand side of Eq. (E.40) is zero. In order to satisfy Eq. (E.40), the elements of the compliance matrix must be zero:

$$\begin{bmatrix} J_{14} & J_{15} \\ J_{24} & J_{25} \\ J_{34} & J_{35} \\ J_{64} & J_{65} \end{bmatrix} = \begin{bmatrix} 0 & 0 \\ 0 & 0 \\ 0 & 0 \\ 0 & 0 \end{bmatrix} \tag{E.42}$$

As a result, the compliance matrix in terms of equation numbers is as follows:

$$[J] = \begin{bmatrix} \text{E.30} & \text{E.30} & \text{E.36} & 0 & 0 & \text{E.30} \\ \text{E.30} & \text{E.30} & \text{E.36} & 0 & 0 & \text{E.30} \\ \text{E.31} & \text{E.31} & \text{E.37} & 0 & 0 & \text{E.31} \\ 0 & 0 & 0 & \text{E.41} & \text{E.41} & 0 \\ 0 & 0 & 0 & \text{E.41} & \text{E.41} & 0 \\ \text{E.30} & \text{E.30} & \text{E.36} & 0 & 0 & \text{E.30} \end{bmatrix} \tag{E.43}$$

The stiffness matrix of the laminate can be calculated by Eq. (E.26). After finding the compliance and stiffness matrices, the elastic constants can be found by the following formulas [41]:

$$\begin{aligned} E_x &= \frac{1}{J_{11}} \quad , \quad E_y = \frac{1}{J_{22}} \quad , \quad E_z = \frac{1}{J_{33}} \\ G_{xy} &= \frac{1}{J_{66}} \quad , \quad G_{yz} = \frac{1}{J_{44}} \quad , \quad G_{zx} = \frac{1}{J_{55}} \\ \upsilon_{xy} &= -\frac{J_{12}}{J_{11}} \quad , \quad \upsilon_{yz} = -\frac{J_{23}}{J_{22}} \quad , \quad \upsilon_{zx} = -\frac{J_{31}}{J_{33}} \end{aligned} \tag{E.44}$$

In ANSYS, either of compliance or stiffness matrices or elastic constants can be used. Moreover, density is also required as a material property for the simulation. It can be calculated with rule of mixtures:

$$\rho_{comp} = \rho_f v_f + \rho_m v_m \tag{E.45}$$

APPENDIX F

STATIC SIMULATION OF THE TRANSDUCER WITH FINITE ELEMENT METHOD (FEM) IN ANSYS

For the static simulation of the transducer, ANSYS 11.0 Multiphysics is used. Again, the rotational symmetry of the geometry, loading and material properties allow a 2-D axisymmetric modeling. In this simulation, there is no need to model the water. The model and finite element mesh are shown in Figure F.1.

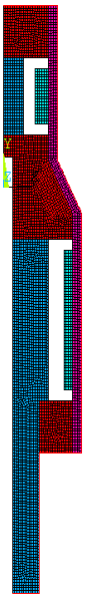

Figure F.1: Axisymmetric finite element model of transducer used in the static simulation

The element types used for CRP Caps, CRP Rods, GRP Coating and PZT Tubes were the same as given in Table D.1. The mesh size is taken as *0.5 mm* in order to obtain more accurate results.

As loading, a pressure of 30 bars is exerted on the outer surface of the transducer, which has contact with the water in real. Then, static analysis is performed.

Material properties required in this simulation are densities and elastic coefficients of the components. For PZT Tubes, Table C.1 is used, whereas Table D.2 is used for CRP Caps, CRP Rods and GRP Coating.

APPENDIX G

DYNAMIC SIMULATION OF THE TRANSDUCER WITH FINITE ELEMENT METHOD (FEM) IN ANSYS

ANSYS 11.0 Multiphysics is used again for the dynamic simulation of the transducer. Similarly, a 2-D axisymmetric modeling is performed. The model and finite element mesh are shown in Figure G.1.

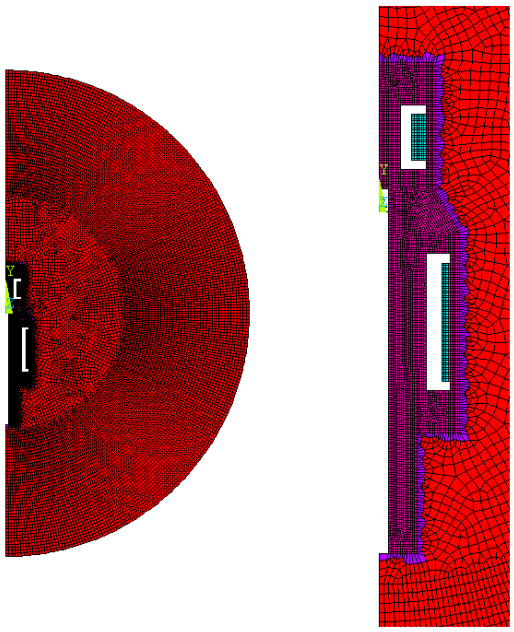

Figure G.1: (a) Axisymmetric finite element model of transducer used in the dynamic simulation, (b) the details of the model.

The element types used for CRP Caps, CRP Rods, GRP Coating, PZT Tubes and water were the same as given in Table D.1. The mesh size is taken *0.5 mm* in the structure and *2 mm* in the water. Moreover, the fluid-structure interaction flag is employed again.

As loading, an axial acceleration of 500g is exerted on the bottom surface of the transducer for 1 millisecond. After this time period, the acceleration is removed and the analysis is continued for an extra 1 millisecond so that the transiency finishes. Therefore, a transient analysis is performed for total 2 milliseconds.

In the same way with the static simulation, material properties required in this simulation are densities and elastic coefficients of the components. For PZT Tubes, Table C.1 is used, whereas Table D.2 is used for CRP Caps, CRP Rods and GRP Coating. On the other hand, the properties required for the water are density and velocity of sound, which were given in Table C.1.

APPENDIX H

THERMAL SIMULATION OF THE TRANSDUCER WITH FINITE ELEMENT METHOD (FEM) IN ANSYS

ANSYS 11.0 Multiphysics is used for the thermal simulation of the transducer. In the simulation, a 2-D axisymmetric model is employed since the geometry, loading and material properties have a rotational symmetry. In a similar way with the static simulation, there is no need to model the water. The model and finite element mesh are shown in Figure H.1.

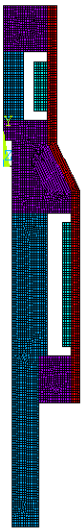

Figure H.1: Axisymmetric finite element model of transducer used in the thermal simulation

In the model, *PLANE77*, a 2-D axisymmetric thermal element, is used for all components of the transducer. The mesh size is again taken as *0.5 mm*.

In the simulation, the heat generated in the tubes is modeled as a body load called heat generation rate (HGEN). It is the heat generated per unit volume and has units of W/m^3. Moreover, convection is applied on the exterior surface of the transducer as a surface load. The initial temperature of the transducer is taken as *35 °C*. Then, a transient thermal analysis is performed for 5 minutes, which is long enough for the transducer to reach steady state.

Material properties required in this simulation are densities, specific heats (c) and thermal conductivities (k) of the components. Specific heat and thermal conductivity of PZT Tubes are shown in Table H.1.

Table H.1: Thermal properties of the PZT tubes used in the model [42]

PZT4 TUBE			
Property	***Symbol***	***Unit***	***Value***
Specific Heat Capacity	c	J/kg°C	420
Thermal Conductivity	k	W/m°C	2.1

On the other hand, the thermal properties of the composite components also depend on the fiber orientations and volumetric fiber ratio. Firstly, the specific heats of the composites are calculated as follows:

$$c = \frac{c_f \rho_f v_f + c_m \rho_m v_m}{\rho_f v_f + \rho_m v_m} \tag{H.1}$$

where c_f and c_m are the specific heats of the fiber and matrix, respectively.

Therefore, the specific heats of the composite components can be calculated from the ones of the constituents. They are tabulated in Table H.2.

Table H.2: Specific heats of the composite components and their constituents [38] [39] [48]

Material	***Unit***	***c***
T300 Carbon fiber	J/kg°C	710
E-Glass fiber		810
Epoxy		1000
Component	***Unit***	***c***
CRP Caps	J/kg°C	831
GRP Coating		856
CRP Rods		803

Secondly, the thermal conductivities of the composites have such a directional dependency that they have different values in different directions. In this simulation, they are taken as tabulated in Table H.3.

Table H.3: Thermal conductivities of the composite components [37]

Component	***Unit***	***r***	***θ***	***z***
CRP Caps	W/m°C	15.6	15.6	0.865
GRP Coating		0.35	1.9	1.9
CRP Rods		0.865	0.865	54.5